BIOFUNCTIONAL POLYMER COATINGS VIA INITIATED CHEMICAL VAPOR DEPOSITION

By

YUMIN YE

Bachelor of Engineering in Materials Science and Engineering
Zhejiang University
Hangzhou, China
2004

Master of Science in Materials Science and Engineering
Zhejiang University
Hangzhou, China
2006

Submitted to the Faculty of the
Graduate College of the
Oklahoma State University
in partial fulfillment of
the requirements for
the Degree of
DOCTOR OF PHILOSOPHY
May, 2012

BIOFUNCTIONAL POLYMER COATINGS VIA

INITIATED CHEMICAL VAPOR DEPOSITION

Dissertation Approved:

Dr. Yu Mao

Dissertation Adviser

Dr. Ning Wang

Dr. Mark R. Wilkins

Dr. Sundar Madihally

Outside Committee Member

Dr. Sheryl A. Tucker

Dean of the Graduate College

TABLE OF CONTENTS

Chapter Page

Chapter Page

LIST OF TABLES

LIST OF FIGURES

Figure Page

CHAPTER III

Figure Page

CHAPTER IV

CHAPTER V

Figure Page

CHAPTER VI

Figure Page

APPENDICES

Figure Page

CHAPTER I

INTRODUCTION

1.1 Motivation

Surface and interface play an essential role in bioengineering. Biomaterials interact with surrounding media through their interfaces both *in vivo* and *in vitro*. To promote or prevent this interaction, many traits of the surface are considered critical, such as chemical composition, surface energy, surface morphology and topography. Unfortunately, materials with desired bulk properties (e.g. mechanical robustness, porosity, optical transparency, and electric conductivity) usually lack the required surface properties. Surface modification of biomaterials thus emerged as an important research field and is attracting more and more attention.

To date, a wide variety of surface modification techniques have been developed to facilitate the application of biomaterials in various bioengineering fields. Mainly, these techniques can be categorized into two approaches.[1] Surfaces can be directly modified physically or chemically so that the atoms and molecules at the surface are substituted, removed, or rearranged. Alternatively, a thin coating over the surface can be applied so that new surface composition, morphology and functionalities are imparted. Methods involving either or both approaches have been implemented in bioengineering to achieve surfaces with a variety of desirable properties including, but not limited to biocompatibility, cell or protein adhesion and surface wettability.

Polymers with various composition and structures confer abundant surface functionalities, enabling them to be widely used in surface modification in bioengineering. For example, hydrogels, which are crosslinked high-swellable polymer networks, can be employed to modify biointerfaces to achieve biocompatibility,[2] protein repulsion,[3,4] and stimuli-responsiveness[5]. Poly(tetrafluoroethylene) is well-known for its low surface energy,

and has been used to minimize surgical adhesions.[6] Polyquaternary amines, along with many other polycationic compounds, are used in creating antimicrobial surfaces.[7,8]

Surface modification with polymers can be implemented using physical adsorption, thin film coating, and polymer grafting. The method of thin film coating provides a versatile and powerful tool in modification of biomaterial surfaces, as it immobilizes polymer films with different surface functionalities and creates bonding to the substrate substantially stronger than physical adsorption; however, it does not require complicated multi-step processes as surface grafting. As such, a variety of bioengineering fields employ this method to modify and create surface biofunctionalities. The objective of this work was to introduce a novel vapor-based polymer coating approach and demonstrate its applications in solving some real-world problems faced in different bioengineering fields.

1.2 Surface modification with polymers in bioengineering

Polymers have been employed for surface modification throughout the bioengineering fields, including biosensors, drug delivery, implants, etc. We focus on the application of polymer thin coatings in three different areas where surface modifications are considered critical, but are difficult to achieve by conventional approaches.

1.2.1 Antimicrobial surfaces

Antimicrobial surfaces are highly desirable from daily use to hospitals and healthcare facilities. Microorganisms can grow and spread in textiles, inducing unpleasant odors, damage to the textiles, and hygienic problems. Bacteria are also the major cause of hospital acquired infections, which affect 5-15% hospitalized patients in the United States and account for a staggering $35.7 billion to $45 billion direct medical cost annually.[9] Significant

efforts are therefore devoted to the development of effective, long-lasting, non-toxic, and environmentally benign antimicrobial surfaces.

Various techniques have been employed to create antimicrobial surfaces, predominantly involving two different bactericidal mechanisms: leaching based and non-leaching based. The leaching-based antimicrobial surfaces kill bacteria by releasing the antimicrobial agents into the surrounding medium and bacteria cells, and disrupting the function of target cell components, such as intracellular proteins or cell membranes. Silver, for instance, has been widely used in fabricating antimicrobial products, such as antibacterial clothes, wound dressing, and self-sterile catheters.[10,11] Silver or silver ions penetrate into the cell and bind to the thiol groups of enzymes and proteins, inducing the loss of enzyme functions and death of the bacteria.[12] Leaching-based antimicrobial surfaces, however, suffer from limitations such as the gradual loss of bactericidal efficacy over time, potential negative influence on the human body and environment, and more importantly, the development of bacteria resistance.[13,14]

Non-leaching antimicrobial surfaces, also known as permanent antimicrobial surfaces, kill microorganisms on contact without releasing biocides into the surrounding medium, which reduce the possibility of developing bacterial resistance. To achieve permanent antimicrobial surfaces, cationic polymers are immobilized onto surfaces by means of polymer coating or grafting. Klibanov et. al pioneered the work of creating permanent antimicrobial surfaces that effectively kill both Gram-positive and Gram-negative bacteria by grafting long-chain hydrophobic polycations, namely poly(vinyl-N-hexylpyridinium)[15,16] and alkylated polyethylenimine[17], onto surfaces of glass and plastics. Ever since, an enormous amount of literature has emerged covering reports on creating antimicrobial surfaces with

polymers using different approaches. Controlled polymerizations, including atom transfer radical polymerization (ATRP)[8,18] and reversible addition fragmentation chain transfer (RAFT),[19] have been employed to immobilize antimicrobial polymers using both "graft to" and "graft from" approaches. The ability to control the molecular weight, chain length, and grafting density of the immobilized polymers contributed to the understanding of the bactericidal mechanism of action and provided future guidance in creating permanent antimicrobial surfaces.

Vapor-based polymer coating and grafting approaches represent an alternative to the fabrication of antimicrobial surfaces. The solventless nature of the process avoids the exposure of the surfaces to harsh organic solvents, allowing preservation of delicate chemical and physical structures of surfaces, such as papers, dissolvable substances and many biomedical devices, e.g. catheters.[20-22] Vapor-based fabrication of antimicrobial surface has been explored by grafting poly(ethylenediamine) on stainless steel and filter paper using plasma enhanced chemical vapor deposition, resulting in 95–98% killing efficacy against both Gram-positive and Gram-negative bacteria.[23] Poly(dimethylaminomethylstyrene) (PDMAMS) was successfully deposited onto textiles using initiated chemical vapor deposition, conferring bactericidal efficacy of more than 99.99%.[24] Without crosslinking, however, PDMAMS coatings tend to gradually dissolve into neutral solution over time since the amino moiety in the DMAMS unit has a pKa of 8-9.[25]

1.2.2 Surface functionalization in biosensor fabrications

Biosensors detect analytes by the interaction of the immobilized biological components, e.g. DNA strands, enzymes, and antibodies, with the target analytes. To

maintain the activity and specificity of the biological component in the sensor over time, it is critical to provide a biologically friendly interface between the biological unit and the transducer. Polymers are an ideal candidate for the surface modification of transducers, as they offer mechanically "soft" structure, variable functionalities, and biocompatibility.[26,27]

Surface modification of biosensors pose additional challenges in comparison with other surface modification scenarios. First, the thickness of the modification layer should be kept minimal, so that the transfer of the detection signal to the transducer is not impeded. On the other hand, the thickness should be sufficient to ensure a complete coverage over the surface, as well as be resistant to delamination in aqueous media. Second, because analytes in the biosensing process are of micrometer to nanometer size, a patterned surface of transducers with ordered microstructures, e.g. vertically aligned carbon nanotube (VACNT) arrays,[28] is usually employed to enhance the detection sensitivity. Modification of such micro- or nanoscale featured surfaces require minimized damage to the surface morphology. Finally, surface modification of transducers requires precise control of surface functionality, preferentially only manipulating the intended functional groups so that the non-specific interactions to the interferants can be minimized.

Polymer coating techniques are used in biosensor fabrication mainly through two approaches: solution-based and vapor-based. Conventional polymer coating processes, such as spin coating and dip coating, lack the ability to precisely control the coating thickness. Layer-by-layer assembly is a novel polymer coating technique that finely tunes the surface composition and coating thickness by alternate and consecutive adsorption of oppositely charged species.[29,30] However, the assembled multilayer structure is usually prone to degradation over time in physiological environments.[31] More importantly, these solution-

based approaches cause damage to the microstructure of the transducers in the wetting and drying process due to capillary force.[32]

Vapor-based polymer coating techniques enable precise control of the coating thickness and excellent preservation of the surface morphology. For example, aldehyde plasma vapor deposition and plasma oxidation have been used to functionalize aligned carbon nanotubes.[33,34] The processes preserved the aligned structure and conferred surface functionalities. The plasma assisted process, however, involves high energy input, which induces the disruption of the delicate functional groups in the monomers. The resultant polymer coatings are thus highly crosslinked with a wide spectrum of non-target functional groups, lacking functional specificity.[35]

We show the modification of VACNT surfaces using a vapor deposition method with moderate energy input. The all-dry process enables complete retention of the aligned morphology and desired functional groups without introducing non-specific functionalities. By depositing two different polymer thin films, we demonstrate the surface functionalization of VACNT arrays with epoxy and hydrogel chemistries, indicating the potential of further biofunctionalization and application in biosensor fabrications. The successful conferring of the epoxy chemistry also enables the transfer of VACNT arrays onto different substrates, which is crucial in the fabrication of biosensors.

1.2.3 Responsive polymer coatings

Stimuli-responsive polymers respond to environmental changes, e.g. temperature, pH, electric and magnetic fields, by altering a variety of properties, e.g. volume, permeability, and surface hydrophilicity. Figure 1-1 illustrates the responding mechanisms of the pH- and

thermo-responsive polymer systems, respectively. The pH-responsiveness usually stems from the ionization/deionization of acidic or basic functional groups, while the thermo-responsiveness involves the switch between thermally more and less favorable conformations of the polymer chains.

By fine engineering of the composition and structure, the responsiveness of the smart polymers can be harnessed to serve for specific bioengineering purposes. For example, pH- and temperature-responsive polymer coatings are applied onto drug molecules and used in drug delivery.[36,37] When delivered to the targeted organs, the polymer coating swells or dissolves subject to the local environmental changes, triggering the release of drugs. Smart polymers have also been exploited to fabricate stimuli-responsive biological membranes with tunable molecule transportations.[38-40] Thermo-responsive coatings of poly(N-isopropyl acrylamide) can switch between hydrophilic and hydrophobic states responding to the environment, indicating potential applications in self-cleaning surfaces.[41]

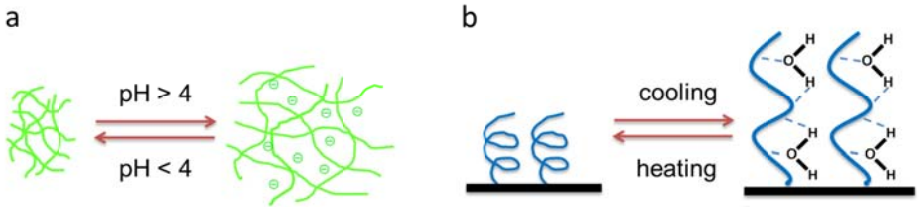

Figure 1-1 Schematic illustration of a) an anionic pH-responsive hydrogel responds to the pH change; b) thermo-responsive polymer brushes respond to the temperature change.

While solution-based polymerization methods are versatile in fabricating responsive polymer coatings, they are not suitable in certain applications, such as coating microstructured substrates with precisely controlled thicknesses and modifying materials that are sensitive to organic solvents or heating. Vapor deposition method with stoichiometric

control serves as a better alternative in these circumstances. We present the controlled vapor deposition of ultrathin responsive hydrogels on nanoporous membranes and VACNT arrays, which enables thermo-responsive transportation of biomolecules and pH-responsive surface wettability, respectively.

1.3 Initiated chemical vapor deposition of biofunctional polymer coatings

Chemical vapor deposition (CVD) utilizes the chemical reaction of gaseous reactants in a vacuum environment to produce solid state materials in the form of film or powder. Compared with the conventional solution-based surface coating techniques, the CVD method offers advantages of fully preserving the microscale and nanoscale structures of the substrates, avoiding damages caused by organic solvents, forming conformal and uniform coatings on substrates with complex geometry, and easy control of coating thickness.[42]

CVD is a well-established technique in producing inorganic thin film coatings, and this technique has been extensively used in the semiconductor industry and metallurgical-coating industry. CVD of polymeric materials is a relatively new field still under exploration. Several CVD methods have been developed to produce polymeric thin films. For example, plasma enhanced chemical vapor deposition (PECVD) utilizes plasma to induce the bombardment of monomers, generating a mixture of electrons, ions, radicals, and atoms, which subsequently undergo polymerization with a free radical mechanism.[43,44] The high energy input of the PECVD process, however, usually results in a highly branched and crosslinked structure of the polymer coating. In addition, the desired functional groups may be disrupted in the process, while non-specific functional groups can be generated.[35,42]

Initiated chemical vapor deposition (iCVD) is a novel CVD technique that has been recently developed to produce polymer thin films.[45-48] The deposition process is distinct from other CVD polymerization methods, as it introduces initiator vapor molecules (e.g. *tert*-butyl peroxide), which is decomposed around the hot filament and subsequently initiates the polymerization. The iCVD process can be perceived as a combination of chemical vapor deposition and free radical polymerization.

Figure 1-2 illustrates a typical setup of an iCVD system. During deposition, precursors and the initiator are heated and vaporized using temperature controllers (V1-V4). The vapors are metered by mass flow controllers (MFC 1-4) and fed into the reactor, which is equipped with a transparent quartz cover and arrayed Nichrome filament ~2.5 cm above the stage. The filament is usually heated to 180-250 °C, while the stage is maintained at 20-50 °C by circulating water. The pressure inside the reactor is usually kept at 0.1-0.5 Torr by a butterfly throttling valve. An interferometry system, consisting of a HeNe laser and a photometer, is used to monitor the deposition process by the *in situ* measurement of the thickness increase on a reference silicon wafer placed close to the substrates.

Inside the reactor, polymerization initiates from the decomposition of the initiator in the vicinity of the heated filament as illustrated in Figure 1-3. The polymerization propagates by the collision of consequently formed radicals with monomers in the vapor phase. Evidence shows that the iCVD polymerization is an adsorption-based process—monomers and oligomers are adsorbed onto the surface of substrates, where chain propagation proceeds.[49] Thus, surface concentration of the monomer is a key factor in iCVD polymerization, which is distinct from solution-based free radical polymerization. The composition of the product in an iCVD copolymerization process is therefore not only related

to the flow rates and copolymerization reactivity ratio of the monomers, but also to the adsorption efficiency of each monomer to the substrate. Progress has been made in understanding the kinetics and mechanism of the iCVD process,[49-51] and polymer coatings with a wide spectrum of functionalities have been fabricated and used in various applications.[25,46,52-56]

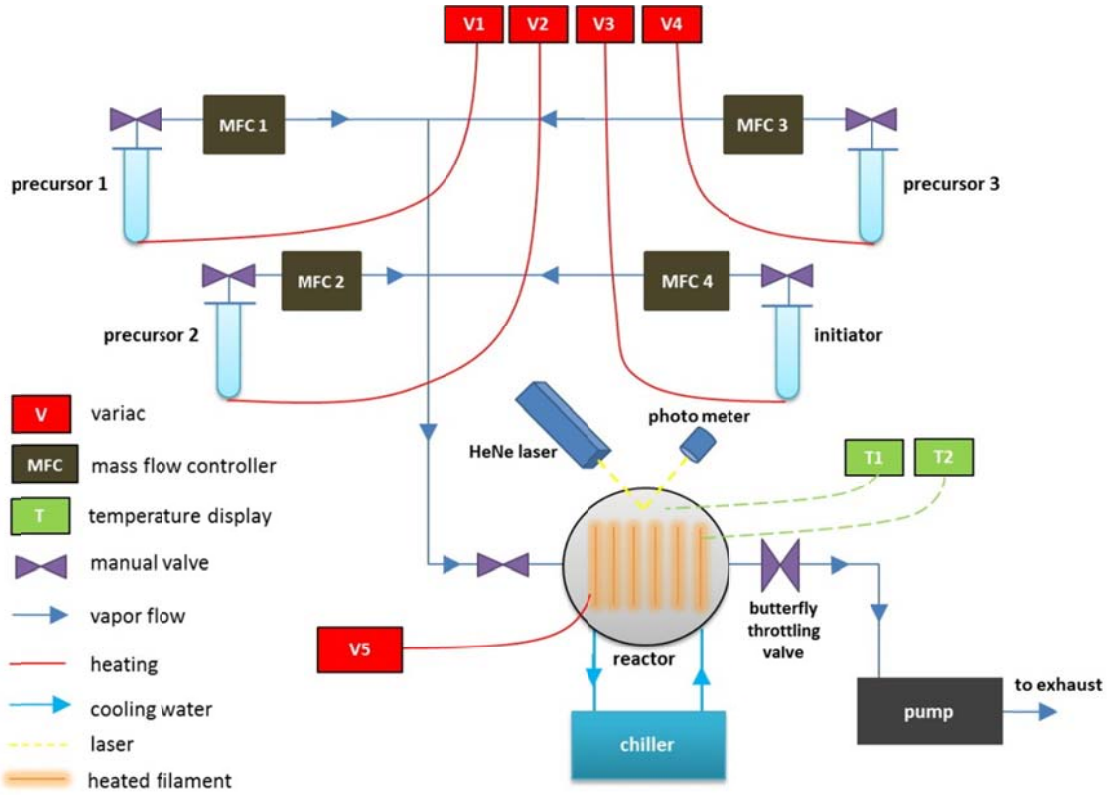

Figure 1-2 Schematics of a typical iCVD setup.

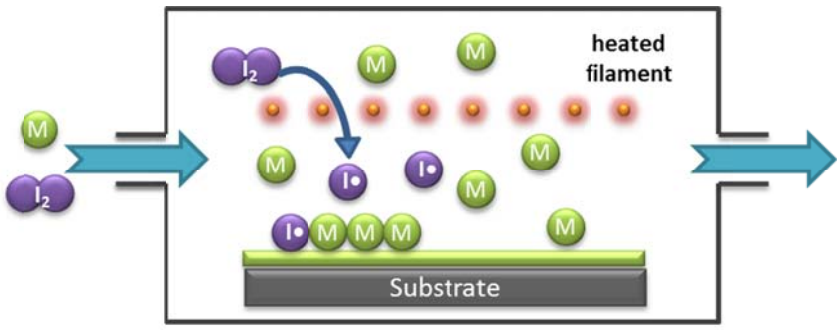

Figure 1-3 Schematic illustration of the polymerization mechanism in the iCVD process. The drawing is not in scale.

The iCVD method is advantageous over other CVD methods in producing stoichiometric polymer films, because the introduction of the initiator significantly lowers the energy input in the deposition process (3-4 W/cm^2), enabling excellent retention of the delicate functional groups and fine control of the polymer composition. In addition, the substrate is cooled by the circulating water in the process and kept away from the heated filament where initiator decomposes, which avoids exposure of the substrate material to any excessive heat. The use of the interferometry system allows precise control of the coating thickness, while the vapor phase polymerization provides conformal coatings on substrate with complex geometry. These advantages, along with other attributes of the CVD process make the iCVD technique ideal for biointerface modifications.

1.4 Scope of thesis

This thesis demonstrates the utilization of the iCVD technique to produce biofunctional polymer coatings to address some surface modification issues faced in the bioengineering field. Different polymer chemistries and coating structures are conferred onto

a variety of substrates including planar Si and glass surfaces, aligned carbon nanotubes, microfibers, catheters, and nanoporous membranes. Each chapter is aimed to address a particular problem in bioengineering, while the theme of the entire thesis is biofunctional polymer coatings using iCVD.

CHAPTER II presents a novel vapor-based hybrid grafting method to fabricate antimicrobial polymer coatings using iCVD. The grafting process employs a highly crosslinked prime layer of poly(dimethylaminomethylstyrene-*co*-ethylene glycol diacrylate) (P(DMAMS-*co*-EGDA)) and *in situ* grafting of PDMAMS polymer initiated from the reactive sites of the crosslinked network. The hybrid grafting method not only creates a strong bonding between the coating and substrate by crosslinking, but also maximizes the surface functionality by surface grafting. The resultant coatings imparted durable antimicrobial efficacy to textiles and catheters.

In CHAPTER III, we explore the surface functionalization of vertically aligned multiwall carbon nanotubes with epoxy chemistry using iCVD. The mild condition and solventless nature of the process enables complete retention of the monomer functionality, as well as the aligned structure of the nanotubes. The epoxy chemistry of the coating was further exploited to realize the transfer of nanotube arrays through an all-dry process, which results in a hybrid array structure with significantly enhanced mechanical properties and wetting stability.

CHAPTER IV extends the vapor functionalization of epoxy chemistry to vertically aligned single walled nanotubes (ASWNTs). By enhancing the access of radicals to the SWNT surface, we demonstrate the covalent functionalization of ASWNT films. Raman and terahertz time-domain spectroscopy proved the creation of covalent bonding and the tuned

electric properties of SWNTs. The vapor-based covalent functionalization of ASWNT film indicates the possibility of tailoring the electronic structure of SWNTs without disrupting its aligned morphology.

CHAPTER V demonstrates the surface functionalization of low-site-density carbon nanotube arrays with pH-responsive hydrogel coating. The hydrogel coating substantially improves the wettability of the nanotube array, facilitating the application of carbon nanotube arrays in biological environments. Superwettability is achieved with a 50 nm hydrogel coating under neutral conditions. We also discuss the quantitative correlation between the coating thickness and surface wettability.

In CHAPTER VI, the iCVD process is employed to fabricate smart nanovalves by coating a sub-50 nm thermo-responsive hydrogel on a nanoporous membrane. We emphasize the capability of the iCVD process to precisely control the coating composition and thickness, as well as the ability to coat surfaces with a complex geometry.

CHPATER VII concludes the advantages of the iCVD process in applications in bioengineering field and discusses future directions.

1.5 References

1. B. D. Ratner, *Biosens. Bioelectron.*, 1995, **10**, 797-804.
2. D. L. Elbert and J. A. Hubbell, *Annu. Rev. Mater. Sci.*, 1996, **26**, 365-394.
3. I. Eshet, V. Freger, R. Kasher, M. Herzberg, J. Lei and M. Ulbricht, *Biomacromolecules*, 2011, **12**, 2681-2685.
4. T. Ekblad, G. Bergstroem, T. Ederth, S. L. Conlan, R. Mutton, A. S. Clare, S. Wang, Y. Liu, Q. Zhao, F. D'Souza, G. T. Donnelly, P. R. Willemsen, M. E. Pettitt, M. E. Callow, J. A. Callow and B. Liedberg, *Biomacromolecules*, 2008, **9**, 2775-2783.
5. J. F. Mano, *Adv. Eng. Mater.*, 2008, **10**, 515-527.
6. J. J. Bauer, B. A. Salky, I. M. Gelernt and I. Kreel, *Ann. Surg.*, 1987, **206**, 765-769.
7. L. Timofeeva and N. Kleshcheva, *Appl. Microbiol. Biotechnol.*, 2011, **89**, 475-492.
8. H. Murata, R. R. Koepsel, K. Matyjaszewski and A. J. Russell, *Biomaterials*, 2007, **28**, 4870-4879.
9. R. D. I. Scott, *The direct medical costs of healthcare-associated infections in U.S. hospitals and the benefits of prevention*, 2009.
10. M. Rai, A. Yadav and A. Gade, *Biotechnol. Adv.*, 2009, **27**, 76-83.
11. Y. Yao, Y. Ohko, Y. Sekiguchi, A. Fujishima and Y. Kubota, *Journal of Biomedical Materials Research Part B-Applied Biomaterials*, 2008, **85B**, 453-460.
12. A. B. G. Lansdown, *J. Wound Care*, 2002, **11**, 125-130.
13. S. Silver, *FEMS Microbiol. Rev.*, 2003, **27**, 341-353.
14. S. L. Percival, P. G. Bowler and D. Russell, *J. Hosp. Infect.*, 2005, **60**, 1-7.
15. J. C. Tiller, C. J. Liao, K. Lewis and A. M. Klibanov, *Proc. Natl. Acad. Sci. U. S. A.*, 2001, **98**, 5981-5985.
16. J. C. Tiller, S. B. Lee, K. Lewis and A. M. Klibanov, *Biotechnol. Bioeng.*, 2002, **79**, 465-471.
17. J. Lin, S. Y. Qiu, K. Lewis and A. M. Klibanov, *Biotechnol. Bioeng.*, 2003, **83**, 168-172.
18. S. B. Lee, R. R. Koepsel, S. W. Morley, K. Matyjaszewski, Y. J. Sun and A. J. Russell, *Biomacromolecules*, 2004, **5**, 877-882.
19. D. Roy, J. S. Knapp, J. T. Guthrie and S. Perrier, *Biomacromolecules*, 2008, **9**, 91-99.
20. U. Edlund, M. Kallrot and A. C. Albertsson, *J. Am. Chem. Soc.*, 2005, **127**, 8865-8871.
21. A. Wirsen, H. Sun and A. C. Albertsson, *Biomacromolecules*, 2005, **6**, 2697-2702.
22. A. Wirsen, H. Sun, L. Emilsson and A. C. Albertsson, *Biomacromolecules*, 2005, **6**, 2281-2289.
23. S. N. Jampala, M. Sarmadi, E. B. Somers, A. C. L. Wong and F. S. Denes, *Langmuir*, 2008, **24**, 8583-8591.
24. T. P. Martin, S. E. Kooi, S. H. Chang, K. L. Sedransk and K. K. Gleason, *Biomaterials*, 2007, **28**, 909-915.
25. T. P. Martin and K. K. Gleason, *Chem. Vap. Deposition*, 2006, **12**, 685-691.
26. K. Z. Gumargalieva, G. E. Zaikov and Y. V. Moiseev, *Int. J. Polymer. Mater.*, 1996, **31**, 183-214.
27. F. Bischoff, *Clin. Chem.*, 1972, **18**, 869-&.
28. C. Wei, L. M. Dai, A. Roy and T. B. Tolle, *J. Am. Chem. Soc.*, 2006, **128**, 1412-1413.
29. G. Decher, *Science*, 1997, **277**, 1232-1237.

30. P. T. Hammond, *Adv. Mater.*, 2004, **16**, 1271-1293.
31. L. Richert, F. Boulmedais, P. Lavalle, J. Mutterer, E. Ferreux, G. Decher, P. Schaaf, J. C. Voegel and C. Picart, *Biomacromolecules*, 2004, **5**, 284-294.
32. C. V. Nguyen, L. Delzeit, A. M. Cassell, J. Li, J. Han and M. Meyyappan, *Nano Lett.*, 2002, **2**, 1079-1081.
33. Q. D. Chen, L. M. Dai, M. Gao, S. M. Huang and A. Mau, *J. Phys. Chem. B*, 2001, **105**, 618-622.
34. P. G. He and L. M. Dai, *Chem. Commun.*, 2004, 348-349.
35. H. O. Pierson, *Handbook of chemical vapor depostion: principles, technology and applications*, Noyes Publications, Norwich, 1999.
36. K. Zhang and X. Y. Wu, *Biomaterials*, 2004, **25**, 5281-5291.
37. A. K. Bajpai, S. K. Shukla, S. Bhanu and S. Kankane, *Prog. Polym. Sci.*, 2008, **33**, 1088-1118.
38. F. Schacher, M. Ulbricht and A. H. E. Muller, *Adv. Funct. Mater.*, 2009, **19**, 1040-1045.
39. W. Lequieu, N. I. Shtanko and F. E. Du Prez, *J. Membr. Sci.*, 2005, **256**, 64-71.
40. J. Wu and M. Sailor, *Adv. Funct. Mater.*, 2009, **19**, 733-741.
41. W. Chen, L. Qu, D. Chang, L. Dai, S. Ganguli and A. Roy, *Chem. Commun.*, 2008, 163-165.
42. K. L. Choy, *Prog. Mater Sci.*, 2003, **48**, 57-170.
43. R. Foerch, A. N. Chifen, A. Bousquet, H. L. Khor, M. Jungblut, L.-Q. Chu, Z. Zhang, I. Osey-Mensah, E.-K. Sinner and W. Knoll, *Chem. Vap. Deposition*, 2007, **13**, 280-294.
44. A. Hiratsuka and I. Karube, *Electroanalysis*, 2000, **12**, 695-702.
45. K. K. S. Lau and K. K. Gleason, *Adv. Mater.*, 2006, **18**, 1972-+.
46. Y. Mao and K. K. Gleason, *Langmuir*, 2004, **20**, 2484-2488.
47. A. Asatekin, M. C. Barr, S. H. Baxamusa, K. K. S. Lau, W. Tenhaeff, J. Xu and K. K. Gleason, *Mater. Today*, 2010, **13**, 26-33.
48. S. H. Baxamusa, S. G. Im and K. K. Gleason, *PCCP*, 2009, **11**, 5227-5240.
49. K. Chan and K. K. Gleason, *Macromolecules*, 2006, **39**, 3890-3894.
50. K. K. S. Lau and K. K. Gleason, *Macromolecules*, 2006, **39**, 3688-3694.
51. K. K. S. Lau and K. K. Gleason, *Macromolecules*, 2006, **39**, 3695-3703.
52. K. Chan and K. K. Gleason, *Langmuir*, 2005, **21**, 8930-8939.
53. M. Gupta and K. K. Gleason, *Langmuir*, 2006, **22**, 10047-10052.
54. W. S. O'Shaughnessy, S. K. Murthy, D. J. Edell and K. K. Gleason, *Biomacromolecules*, 2007, **8**, 2564-2570.
55. K. K. S. Lau and K. K. Gleason, *Macromol. Biosci.*, 2007, **7**, 429-434.
56. M. E. Alf, P. D. Godfrin, T. A. Hatton and K. K. Gleason, *Macromol. Rapid Commun.*, 2010, **31**, 2166-2172.

CHAPTER II

SOLVENTLESS HYBRID GRAFTING OF ANTIMICROBIAL POLYMERS FOR SELF-STERILIZING SURFACES

Y. M. Ye, Q. Song, Y. Mao, "Solventless hybrid grafting of antimicrobial polymers for self-sterilizing surfaces", *Journal of Materials Chemistry,* 2011, 21, 13188-13194.

Abstract

Self-sterilizing surfaces were created using a single-step solventless grafting method. The grafting process was conducted by vapor deposition of a crosslinked poly(dimethylaminomethyl styrene-*co*-ethylene glycol diacrylate) (P(DMAMS-*co*-EGDA)) prime layer, followed by *in situ* grafting of poly(dimethylaminomethyl styrene) (PDMAMS) from the reactive sites of the prime layer. The hybrid coating allows both strong binding with the substrate and enriched bactericidal functionality on the surface. Coating analysis indicated successful grafting of PDMAMS on the surface. The atomic force microscope (AFM) observation revealed dense granular structures on the coating surface at the initial stage of grafting and larger domains as the grafting proceeded. Live/dead viability assay showed disruption of bacterial membranes upon surface contact with the grafted coating. The hybrid grafted coating of P(DMAMS-*co*-EGDA)-*g*-PDMAMS had more than 99% bacterial killing against both gram-negative *Escherichia coli* and gram-positive *Bacillus subtilis*. The grafted coating exhibited durable bactericidal efficacy after continuous washing.

2.1 Introduction

Hospital-acquired infections caused by medical devices such as catheters and implants is a major healthcare issue in the United States.[1] It is estimated that hospital infections, mainly including catheter-associated urinary tract infections, central line-associated bloodstream infections and ventilator-associated pneumonia, affect 5-15% hospitalized patients in the U.S. and cause $35.7 billion to $45 billion direct medical costs annually.[2] Self-sterilizing surfaces with effective and long-lasting biocidal activity are highly desirable to prevent catheter-associated infections. Conventional antimicrobial treatments, such as impregnation and coating of antibiotics and silver, have been widely used in clinical practice.[3-6] However, the antimicrobial effect of these coatings is based on the leaching of biocidal agents, which results in the decrease of antimicrobial efficacy over time and the development of bacterial resistance.[3,7,8]

Grafting of antimicrobial polymers has advantages in creating sterile surfaces, because the resultant surfaces kill bacteria on contact without releasing biocides into the surrounding medium, which makes the surface permanently sterile and reduces the possibility of developing bacterial resistance.[9-11] Great efforts have been made to graft antimicrobial polymers onto solid surfaces using liquid-phase polymerization. Antimicrobial polymers such as polyvinylpyridinium[12,13] and polyethyleneimine[14,15]were synthesized in solution and covalently attached onto pretreated glass and plastic surfaces, resulting in surfaces with bacterial killing efficacy as high as 99%. Poly(2-(dimethylamino)ethyl methacrylate) was grafted from substrates using atom transfer radical polymerization and reversible addition-fragmentation chain transfer polymerization, followed by quaternization of the amino groups to confer antibacterial

properties.[16-18] The controlled surface polymerization enables surface design with controlled grafting density and polymer chain length; therefore, high bactericidal efficacy can be achieved by optimizing the grafting conditions. However, the "graft from" and "graft to" methods require surfaces that can accommodate surface initiation and coupling chemistry, respectively. Furthermore, the liquid-based grafting polymerization usually involves sample pretreatment and multi-step reactions in various solvents, which can be time-consuming and may affect the physical properties of substrate materials.[19,20] Grafting of antimicrobial polymers without any surface derivation has not been reported.

Vapor-based grafting of antibacterial polymers is an all-dry approach to create sterile surfaces. The solvent-free process offers advantages of eliminating possible chemical and physical damages to substrates, as well as contaminations caused by solvents.[21-23] Using UV-generated radicals, chemical vapor deposition was employed to graft plastic surfaces with poly(dimethylaminomethyl styrene) (PDMAMS) and poly(diethylamino ethyl acrylate). Though these two polymers have been reported to be antimicrobial in the non-grafted format,[16,24] no antimicrobial activity was reported in the grafted coatings, possibly due to the damage of antimicrobial functionality caused by UV.[25] In a different study, surfaces of stainless steel and filter paper were grafted with poly(ethylenediamine) using plasma enhanced chemical vapor deposition.[26] The resulted surfaces exhibited 95-98% killing efficacy against both gram- positive and gram- negative bacteria.

Previously, we have demonstrated the antibacterial properties of vapor-crosslinked poly(dimethylaminomethyl styrene-*co*-ethylene glycol diacrylate) (P(DMAMS-*co*-EGDA)) coatings with systematically varied crosslinking degrees.[27] The bactericidal effect was found to be influenced by the crosslinking degree. In this work, we explored

hybrid vapor grafting of P(DMAMS-*co*-EGDA)-*g*-PDMAMS, which involves deposition of a crosslinked P(DMAMS-*co*-EGDA) prime layer followed by *in situ* grafting of PDMAMS via successive polymerization initiated from the reactive sites of the prime layer (Figure 2-1). The resultant coating has a hybrid structure that consists of a highly crosslinked prime layer, which is bound to the solid surface, and a grafted polymer layer, which maximizes the surface bactericidal functionality. The hybrid vapor grafting is a solvent-free process that proceeds rapidly (< 1 h) and can be applied onto any substrates without surface pretreatment and derivation. The grafting process and the chemical composition of the grafted coatings were investigated. The antimicrobial activities of the grafted coating on both planar and three-dimensional substrates were studied.

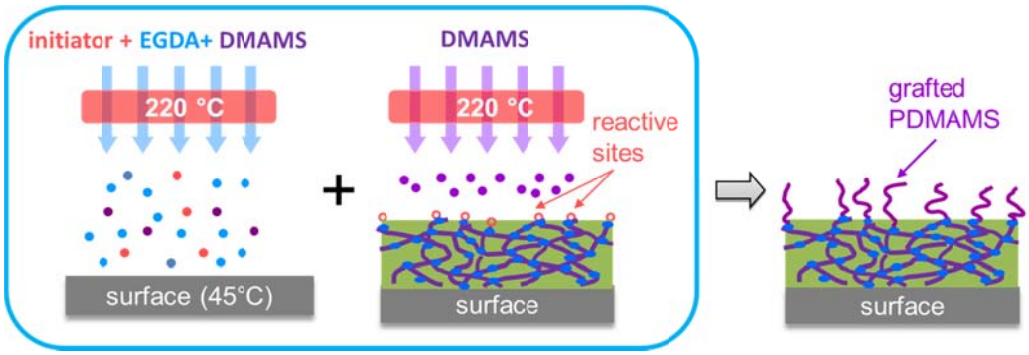

Figure 2-1 Schematic illustration of the hybrid grafting of P(DMAMS-*co*-EGDA)-*g*-PDMAMS.

2.2 Experimental

2.2.1 Materials

DMAMS (95%), EGDA (90%), and *tert*-butyl peroxide (TBP) (98%) were all purchased from Sigma-Aldrich. The DMAMS monomer, consisting of 50/50 *ortho*- and *para*-isomers, was vacuum purified prior to use to remove volatile contaminants. EGDA and TBP were directly used without further purification. Silicon wafer (MEMC Electronic Materials) was used as received. Glass slides were cleaned using ultrasonication in acetone for 15 min and dried under N_2 flow. Sterile catheter tubings (ICU Medical) with an outside diameter of 0.28 cm were cut into sections of 2.5 cm. Nylon textiles (306 A, Testfabric) with an average fiber diameter of 16-18 μm was cleaned using detergent and cut into 4×4 cm^2 pieces prior to the deposition.

2.2.2 Hybrid grafting

The hybrid graft coating was carried out using initiated chemical vapor deposition (iCVD) as previously reported.[27] Precursors of DMAMS, EGDA and TBP were vaporized at 75 °C, 60 °C and 25 °C, respectively, mixed well and metered into a custom-built reactor (Sharon Vacuum) through mass flow controllers (MKS, model 1153, 1150 and 1479A). The deposition conditions of the hybrid coating were listed in Table 2-1. For comparison, the deposition of the P(DMAMS-*co*-EGDA) prime coating was conducted using the same conditions as in stage I. And the PDMAMS homopolymer coating was synthesized without introducing EGDA. The deposition process was monitored real-time using an interferometry system with a 633 nm He-Ne laser (JDS Uniphase), through which the increase of coating thickness on a silicon wafer was observed. Catheters and

textiles were coated on both sides to ensure a complete coverage of the surface. After the vapor grafting, the coatings were continuously washed in phosphate buffer saline (PBS) solutions at 200 rpm using an incubator shaker (Isotemp, Fisher Scientific) for 60 min to remove any ungrafted PDMAMS.

2.2.3 Characterizations

Fourier transform infrared (FTIR) spectra of the coatings on silicon surfaces were collected using a Nicolet 6700 FTIR spectrometer equipped with DTGS detector under the transmission mode. The topography of the graft coatings was measured using a Veeco Multimode SPM atomic force microscope (AFM) under the tapping mode. Surface sectioning analysis was obtained using the Nanoscope software. The X-ray photoelectron spectroscopy (XPS) measurements were performed using the Mg anode of a PHI 300 W twin anode X-ray source. The resulting photoelectrons were detected by a PHI double-pass cylindrical mirror analyzer (CMA) with a pass energy of 50 eV. The escape depth of the measurement was within 10 nm from the surface.

2.2.4 Antibacterial assessment

Gram-negative *Escherichia coli* (ATCC 29425) and gram-positive *Bacillus subtilis* (ATCC 6633) were cultured for 18 h in LB liquid medium and diluted in sterile PBS solution to the desired colony forming units per ml (CFU/ml). The culturing temperatures of *E. coli* and *B. subtilis* were 37 °C and 30 °C, respectively.

Live/dead viability assay (Invitrogen) was conducted using a two-color fluorescence method. Two fluorescent dyes, a green SYTO9 stain and a red propidium iodide stain, were used. The dyes were mixed and incubated with *E. coli* at ~10^7 CFU/ml.

Subsequently, an aliquot of 15 µl of the bacteria solution was applied to pristine, prime, and graft coated glass surfaces. The test surfaces were covered with coverslips and incubated in the dark for 40 min. The bacteria cells were then observed using an Olympus BX51 epifluorescence microscope with GFP bandpass, GFP, and TRITC filters.

Pristine and graft coated catheter sections were separately immersed in 1 ml of *E. coli* solution at the concentration of 1.5-3.0×10^5 CFU/ml and shaken under 250 rpm at 37 °C for 24 h. Afterwards the catheter sections were removed from the *E. coli* solutions, washed thoroughly using a 0.85% NaCl solution, rolled and incubated in LB agar plates at 37 °C for 20 h. To quantitatively test the bactericidal efficacy of the coated catheters, the supernatant from the tested solution was diluted to 10^1, 10^2, and10^3 times in series, and 100 µl of each dilution was incubated in LB agar plates for 20 h. Each sample was placed in three plates. The bacterial colonies were counted, and the percentile reduction was calculated from the CFU/ml of the uncoated catheter sections (U) and the CFU/ ml of the coated catheter sections (C): reduction rate (%) = (U-C) /U ×100 (%). The coated nylon textiles were also tested against the gram-positive *B. subtilis* using the method reported previously.[27]

2.3 Results and discussion

2.3.1 Vapor-Based hybrid grafting

The vapor-based hybrid grafting was conducted through a one-step, two-stage process, as illustrated in Figure 2-1. Details of the process conditions are listed in Table 2-1. At the initial stage, vaporized monomers of DMAMS and EGDA were fed into the reactor

along with the initiator TBP. A high flow ratio of EGDA versus DMAMS was used to form a highly crosslinked P(DMAMS-*co*-EGDA) prime layer on the substrates with strong substrate-coating adhesion. At the second stage, the flow of the EGDA crosslinker was switched off, while the DMAMS vapor continued to flow in, resulting in the grafting polymerization of PDMAMS from the unterminated radical sites of the P(DMAMS-*co*-EGDA) prime layer. After the deposition, the ungrafted PDMAMS was removed by continuous washing in PBS solutions.

Table 2-1 The deposition conditions of the hybrid graft coating.

	flow rate (sccm)			deposition	pressure
	DMAMS	EGDA	TBP	time (min)	(torr)
Stage I	0.45	0.2	0.4	15	0.2
Stage II	0.65	0	0.4	30	0.2

The vapor-based hybrid grafting combines the crosslinking and grafting of functional polymers in one step without using any substrate pretreatment. The initiation sites for polymer grafting are directly provided by the unterminated radicals generated *in situ* from the crosslinking deposition of the prime layer, which serves as a transitional layer between the grafted polymer and the substrate. The prime layer has a highly crosslinked structure as to be discussed in the composition analysis; therefore, although the PDMAMS chains are not directly grafted onto the substrates, the prime layer ensures strong binding of the PDMAMS polymer with the substrate. In addition, the vapor-based

grafting can be applied to a wide variety of substrates with complex geometries and proceeds much faster (<1 h) than most liquid-based graft polymerizations.

To understand how the hybrid grafting proceeds, the grafting process was terminated at different grafting time, and the topography of the resultant coatings was observed using AFM. As seen in Figure 2-2a, the P(DMAMS-*co*-EGDA) prime coating showed a smooth and uniform surface, which is a typical characteristic of hydrophilic coatings synthesized using initiated chemical vapor deposition.[28,29] The root mean square roughness (RMS) of the surface was measured as 0.31 nm. Granular morphology was observed on the surfaces of the P(DMAMS-*co*-EGDA)-*g*-PDMAMS coatings. A clear trend of increasing granule size and roughness with the increase of grafting time is shown in Figure 2-2(b-d). Small granular structure appeared on the coating surface after 4 min of grafting, resulting in a RMS surface roughness of 0.7 nm. The granules were densely distributed with an average height of 1.5 nm as estimated from the sectioning profile (not shown). The closely packed granular structure suggests abundant unterminated radicals on the prime layer surface at the end of the P(DMAMS-*co*-EGDA) deposition. These reactive sites competed with each other for the grafting of DMAMS monomers, leading to a restricted growth of the grafted chains. Larger granular domains were formed as the grafting time increased to 11 min. The average height of the granules and the RMS roughness rose to 3 nm and 1.8 nm, respectively. After 30 min, significantly larger domains with height up to 15 nm were observed, resulting in a RMS surface roughness of 4.4 nm. The dense granular structures have been observed on polymer grafted surfaces using plasma activated initiation.[30-32] The vapor-based activation combined with the

"grafting from" approach provides higher grafting density and coating uniformity than the "grafting onto" method in preparation of antibacterial surfaces.[33]

The average granule height was plotted as a function of the grafting time (Figure S2-1). A linear relationship between the two variables was observed. The grafting of PDMAMS was thus estimated to have a stable growth rate. It is noted that a small amount of residual EGDA monomers may still exist in the beginning of the grafting process, which possibly creates branched and crosslinked polymer chains in the grafted granules. However, considering the volume of the reactor (ca. 2 L) and the total flow rate of the precursors (1.05 sccm), the residence time of EGDA in the reactor was roughly calculated to be 0.5 min; therefore, the effect of the EGDA residue was not significant in the grafting of PDMAMS. The hybrid grafting process is expected to significantly increase the concentration of the DMAMS component on the coating surface, as to be discussed below.

2.3.2 Coating analysis

Figure 2-3a shows the FTIR spectra of the synthesized PDMAMS homopolymer, P(DMAMS-*co*-EGDA) prime coating, and P(DMAMS-*co*-EGDA)-*g*-PDMAMS coating. The strong absorption peak at 1735 cm^{-1} was assigned to the C=O stretching in EGDA, while peaks in the region of 2700 -2850 cm^{-1} were assigned to the C-H stretching of the tertiary amine in DMAMS. Both characteristic absorption peaks were found in the spectra of the prime and grafted coatings, indicating the successful copolymerization of the DMAMS and EGDA monomers. It is noted that the intensity of the tertiary amine C-

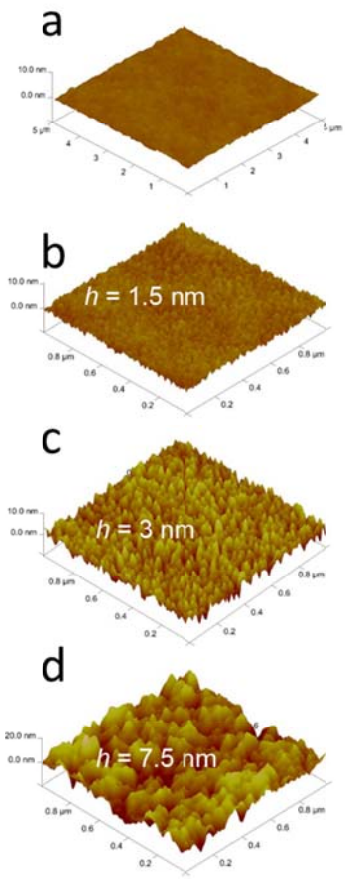

Figure 2-2: AFM images of a) prime coating and grafted coatings synthesized at different grafting time: b) 4 min, c) 11 min, and d) 30 min. *h* represents the average granule height.

H stretching is much weaker than the C=O stretching in both spectra. The intensity disparity was attributed to the high EGDA content in both coatings.

The composition difference between the grafted and the prime coatings was further analyzed by comparing their tertiary amine C-H stretching at 2814 cm^{-1} (Figure 2-3b). Both spectra were normalized to the C=O stretching peak at 1735 cm^{-1}. The grafted coating shows a slightly stronger absorption of C-H stretching than that of the prime coating. Using FTIR quantification, the molar ratios of DMAMS to EGDA in the grafted

and prime coatings were calculated to be 2.14 and 2.03, respectively. The detailed procedures of the calculation have been described previously.[27,34] The increased DMAMS content in the grafted coating confirmed the successful grafting of PDMAMS on the surface, since the P(DMAMS-*co*-EGDA) layer in the grafted coating has the same composition and thickness as that of the prime coating.

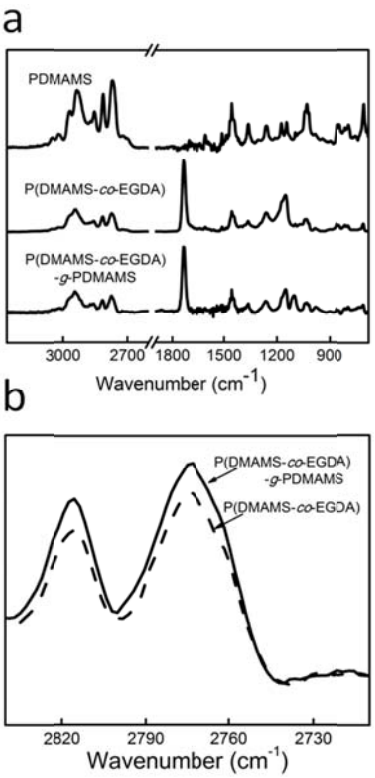

Figure 2-3: a) FTIR spectra of as-deposited PDMAMS, P(DMAMS-*co*-EGDA), and P(DMAMS-*co*-EGDA)-*g*-PDMAMS coatings; b) enlarged region of the tertiary amine C-H stretching in P(DMAMS-*co*-EGDA) and P(DMAMS-*co*-EGDA)-*g*-PDMAMS. Both spectra were normalized to the intensity of the C=O stretching.

Further evidence of the surface composition disparity between the grafted and prime coatings was provided by XPS measurement (Figure S2-2). Compared with the

spectra of the prime coating, the spectra of the grafted coating showed a reduced O1s photoelectron peak and an increased C1s photoelectron peak. Since DMAMS contains more carbon content than EGDA and no oxygen content, the enhanced C1s and reduced O1s intensity confirms that DMAMS is enriched on the surface of the grafted coating.

2.3.3 Antimicrobial properties

The live/dead viability assay was employed to first examine the interaction of the P(DMAMS-*co*-EGDA)-*g*-PDMAMS coating with the gram-negative *E. coli,* which is commonly found in catheter-associated infections.[3] *E. coli* was incubated with the pristine, prime, and graft coated glass slides and stained with two fluorescence dyes, SYTO9 and propidium iodide. The green SYTO9 penetrates the cell membrane and stains bacteria with both intact and damaged membranes, while the red propidium iodide only stains bacteria with damaged membranes.[35] As shown in Figure 2-4a and b, only green fluorescence was observed on the pristine and prime coated glass slides, indicating that the bacterial membrane was intact after incubation on these surfaces. It is not surprising that the prime coating with a DMAMS/EGDA molar ratio of 2.03 did not show any bactericidal activity towards *E. coli*, since our previous study showed that the DMAMS/EGDA molar ratio needed to be more than 5.4 in the P(DMAMS-*co*-EGDA) coating to achieve strong bactericidal effect.[27] However, most of the bacteria on the graft coated glass surface were stained with propidium iodide (Figure 2-4c), indicating the disruption of the bacterial membranes after being in contact with the graft coated surface. The strong bactericidal effect of the grafted coating with the DMAMS/EGDA molar ratio

as low as 2.14 proves that the hybrid grafting method significantly enhanced the bactericidal functionality on the surface.

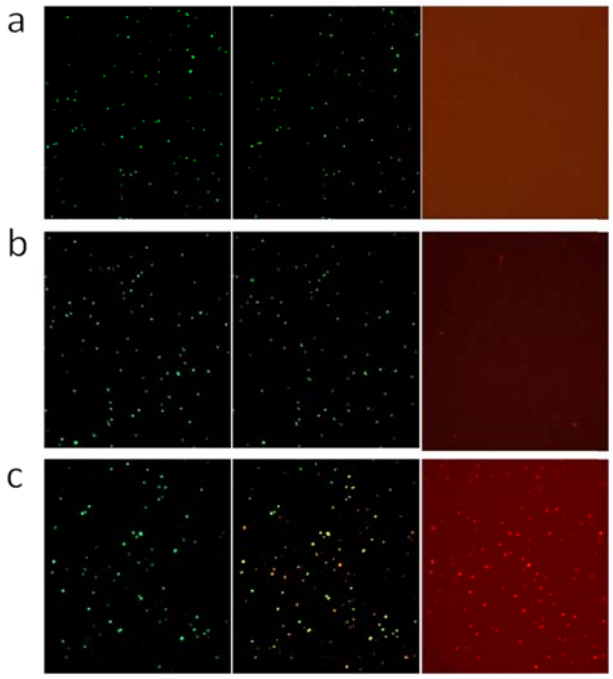

Figure 2-4: Fluorescence microscopy images of *E. coli* after 40 min incubation on a) pristine, b) P(DMAMS-*co*-EGDA), and c) P(DMAMS-*co*-EGDA)-*g*-PDMAMS coated glass slides using green band-pass (left column), green (center column), and red (right column) filters.

The bactericidal efficacy of catheter sections coated with P(DMAMS-*co*-EGDA)-*g*-PDMAMS was directly studied using *E. coli*. After incubation with the bacteria solution for 24 h, the catheter sections were transferred to LB agar plates and incubated for 20 h. No colony was observed around the graft coated catheter section, while the pristine catheter section was surrounded by dense colonies (Figure 2-5a). The results

indicated that the grafted coating successfully inhibited the growth of bacteria on the catheter surface. To quantitatively assess the bactericidal effect, the supernatant of the challenged bacterial solution was extracted, diluted, and incubated in LB agar plate to count the survived bacteria. The supernatant of the graft coated catheter resulted in nearly no growth of colony, while the pristine catheter section showed colonies of more than 1000 (Figure 2-5b). Therefore, the killing efficacy of the grafted coating against *E. coli* was estimated to be more than 99.9%.

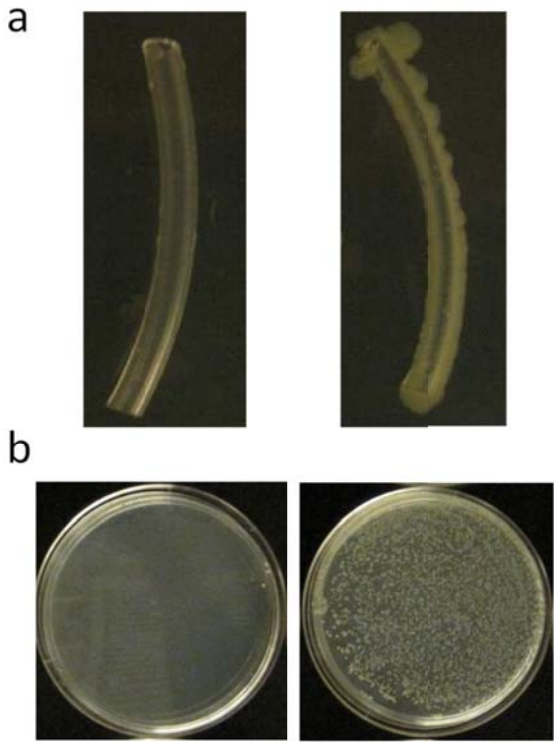

Figure 2-5 a) *E. coli* colony formation on the P(DMAMS-*co*-EGDA)-*g*-PDMAMS coated (left) and pristine (right) catheter sections; b) colonies of survived *E. coli* in solutions after incubation with P(DMAMS-*co*-EGDA)-*g*-PDMAMS coated (left) and pristine (right) catheter sections.

To study the bactericidal efficacy of the grafted coating against gram-positive bacteria, textiles coated with P(DMAMS-*co*-EGDA)-*g*-PDMAMS were challenged with *B. subtilis*. As shown in Figure 2-6, the grafted coating exhibited potent bacterial killing efficacy of more than 99%, while the prime coating showed a killing efficacy of less than 50%. The killing efficacy of the prime coating towards *B. subtilis* is comparable with that of P(DMAMS-*co*-EGDA) copolymers with similar composition.[27] Similar to the results obtained in the *E. coli* viability assay, the grafted coating demonstrated greatly improved *B. subtilis* killing efficacy than the copolymer counterpart due to the surface enrichment of the DMAMS moiety on the coating surface, which resulted in a higher charge density.[27,36]

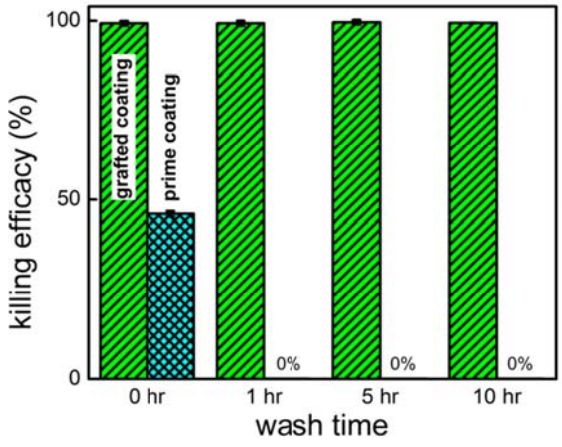

Figure 2-6 Bactericidal efficacies of the grafted and prime coatings against *B. subtilis* after different time of washing.

We further investigated the durability of the grafted coatings using two approaches. First, we compared the FTIR spectra of the P(DMAMS-*co*-EGDA)-*g*-

PDMAMS coating before and after washing at 200 rpm for 24 h (Figure S2-3). The spectrum of the post-wash coating exactly overlapped with that of the original grafted coating, indicating no loss of PDMAMS. The resemblance of the two FTIR spectra also indicated that the strong bacterial killing of the coating was not due to the leaching of PDMAMS from the surface. Second, textiles with the grafted coating were washed in PBS solutions followed by evaluation of the bactericidal efficacy. Figure 2-6 shows the bacterial killing efficacy of the grafted coatings after different washing time. The graft coated textile retained more than 99% killing efficacy with no loss of the bactericidal effect observed after intensive washing for up to 10 h. In comparison, the prime coating showed 0% bacterial killing after only 1 h washing, the cause of which is still unclear. Nevertheless, the durability tests suggested that the grafted coating is durable with the bactericidal functionality excellently preserved after washing under harsh conditions.

2.4 Conclusions

Hybrid grafted coatings of P(DMAMS-*co*-EGDA)-*g*-PDMAMS were synthesized using a vapor deposition process. The grafting was achieved by depositing a highly crosslinked P(DMAMS-*co*-EGDA) prime layer followed by *in situ* grafting of PDMAMS from the reactive sites of the prime layer. AFM, FTIR, and XPS analysis confirmed successful grafting of PDMAMS to the surface. The grafted coating disrupted bacterial membranes upon surface contact. High killing efficacy of greater than 99% against both gram-positive and gram-negative bacteria was observed. The grafted coatings exhibited durable bactericidal efficacy against continuous washing. The vapor-based hybrid

grafting is an all-dry, single-step process that requires no surface pretreatment and can be applied onto a wide variety of substrates, including thermo-sensitive materials, surfaces with nanoscale features, and surfaces with complex geometry. The hybrid grafting concept can be extended to the grafting of other functional polymers to maximize the surface functionality while maintaining the coating stability.

2.5 Acknowledgements

We thank Oklahoma Center for the Advancement of Science and Technology for the financial support (# ONAP 09-12 and AR 09.02-024) for this research. We also thank the Oklahoma State University Microscopy Laboratory for AFM experiments, Dr. Astri Wayadande for the use of the fluorescence microscope and Dr. Nicholas Materer for the help on XPS experiments.

2.6 References

1. B. W. Trautner and R. O. Darouiche, *Arch. Intern. Med.*, 2004, **164**, 842-850.
2. Z. F. Ren, Z. P. Huang, J. W. Xu, J. H. Wang, P. Bush, M. P. Siegal and P. N. Provencio, *Science*, 1998, **282**, 1105-1107.
3. S. Noimark, C. W. Dunnill, M. Wilson and I. P. Parkin, *Chem. Soc. Rev.*, 2009, **38**, 3435-3448.
4. N. Penel and Y. Yazdanpanah, *Support. Care Cancer*, 2009, **17**, 285-293.
5. M. Rai, A. Yadav and A. Gade, *Biotechnol. Adv.*, 2009, **27**, 76-83.
6. Y. Yao, Y. Ohko, Y. Sekiguchi, A. Fujishima and Y. Kubota, *J. Biomed. Mater. Res., Part B*, 2008, **85B**, 453-460.
7. S. Silver, *FEMS Microbiol. Rev.*, 2003, **27**, 341-353.
8. S. L. Percival, P. G. Bowler and D. Russell, *J. Hosp. Infect.*, 2005, **60**, 1-7.
9. S. Borman, *Chem. Eng. News*, 2002, **80**, 36-38.
10. K. Lewis and A. M. Klibanov, *Trends Biotechnol.*, 2005, **23**, 343-348.
11. N. M. Milovic, J. Wang, K. Lewis and A. M. Klibanov, *Biotechnol. Bioeng.*, 2005, **90**, 715-722.
12. J. C. Tiller, C. J. Liao, K. Lewis and A. M. Klibanov, *Proc. Natl. Acad. Sci. U. S. A.*, 2001, **98**, 5981-5985.
13. J. Lin, J. C. Tiller, S. B. Lee, K. Lewis and A. M. Klibanov, *Biotechnol. Lett.*, 2002, **24**, 801-805.
14. J. Lin, S. Y. Qiu, K. Lewis and A. M. Klibanov, *Biotechnol. Bioeng.*, 2003, **83**, 168-172.
15. N. Pasquier, H. Keul, E. Heine and M. Moeller, *Biomacromolecules*, 2007, **8**, 2874-2882.
16. S. B. Lee, R. R. Koepsel, S. W. Morley, K. Matyjaszewski, Y. J. Sun and A. J. Russell, *Biomacromolecules*, 2004, **5**, 877-882.
17. H. Murata, R. R. Koepsel, K. Matyjaszewski and A. J. Russell, *Biomaterials*, 2007, **28**, 4870-4879.
18. D. Roy, J. S. Knapp, J. T. Guthrie and S. Perrier, *Biomacromolecules*, 2008, **9**, 91-99.
19. A. Bhattacharya and B. N. Misra, *Prog. Polym. Sci.*, 2004, **29**, 767-814.
20. L. Li, Z. B. Yang, H. J. Gao, H. Zhang, J. Ren, X. M. Sun, T. Chen, H. C. Kia and H. S. Peng, *Adv. Mater.*, 2011, **23**, 3730-3735.
21. U. Edlund, M. Kallrot and A. C. Albertsson, *J. Am. Chem. Soc.*, 2005, **127**, 8865-8871.
22. A. Wirsen, H. Sun and A. C. Albertsson, *Biomacromolecules*, 2005, **6**, 2697-2702.
23. A. Wirsen, H. Sun, L. Emilsson and A. C. Albertsson, *Biomacromolecules*, 2005, **6**, 2281-2289.
24. T. P. Martin, S. E. Kooi, S. H. Chang, K. L. Sedransk and K. K. Gleason, *Biomaterials*, 2007, **28**, 909-915.
25. T. P. Martin, K. L. Sedransk, K. Chan, S. H. Baxamusa and K. K. Gleason, *Macromolecules*, 2007, **40**, 4586-4591.
26. S. N. Jampala, M. Sarmadi, E. B. Somers, A. C. L. Wong and F. S. Denes, *Langmuir*, 2008, **24**, 8583-8591.
27. Y. M. Ye, Q. Song and Y. Mao, *J. Mater. Chem.*, 2011, **21**, 257-262.
28. W. S. O'Shaughnessy, S. K. Murthy, D. J. Edell and K. K. Gleason, *Biomacromolecules*, 2007, **8**, 2564-2570.
29. N. Mari-Buye, S. O'Shaughnessy, C. Colominas, C. E. Semino, K. K. Gleason and S. Borros, *Adv. Funct. Mater.*, 2009, **19**, 1276-1286.
30. B. Lego, M. Francois, W. G. Skene and S. Giasson, *Langmuir*, 2009, **25**, 5313-5321.
31. B. Lego, W. G. Skene and S. Giasson, *Macromolecules*, 2010, **43**, 4384-4393.
32. G. T. Lewis and Y. Cohen, *Langmuir*, 2008, **24**, 13102-13112.

33. J. Y. Huang, R. R. Koepsel, H. Murata, W. Wu, S. B. Lee, T. Kowalewski, A. J. Russell and K. Matyjaszewski, *Langmuir*, 2008, **24**, 6785-6795.
34. K. Chan and K. K. Gleason, *Langmuir*, 2005, **21**, 8930-8939.
35. A. E. Madkour, J. A. Dabkowski, K. Nusslein and G. N. Tew, *Langmuir*, 2009, **25**, 1060-1067.
36. R. Kugler, O. Bouloussa and F. Rondelez, *Microbiology-Sgm*, 2005, **151**, 1341-1348.

2.7 Supporting Information

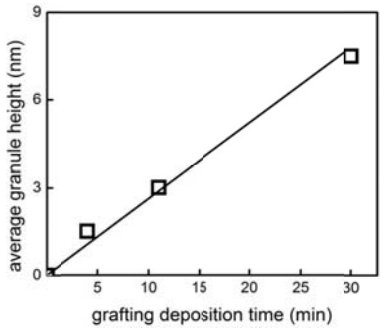

Figure S2-1 The increase of the average granule height as a function of the grafting time.

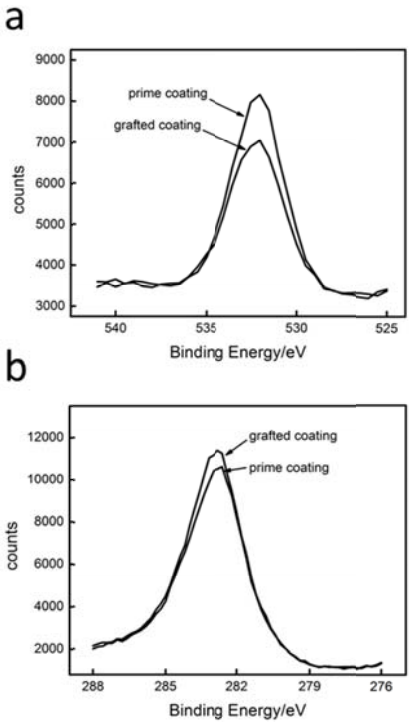

Figure S2-2 O1s and C1s XPS spectra of the prime and grafted coatings.

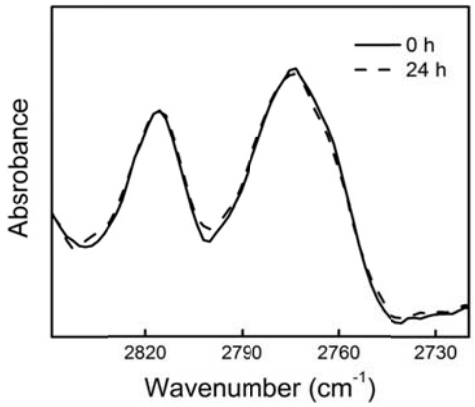

Figure S2-3 FTIR spectra of the P(DMAMS-*co*-EGDA)-*g*-PDMAMS coatings before and after washing for 24 h.

CHAPTER III

FUNCTIONALIZATION AND TRANSFER OF ALIGNED CARBON NANOTUBES WITH VAPOR-DEPOSITED POLYMER NANOCOATINGS

Y. M. Ye, Y. Mao, F. Wang, H. B. Lu, L. T. Qu, L. M. Dai, "Solvent-free functionalization and transfer of aligned carbon nanotubes with vapor-deposited polymer nanocoatings", *Journal of Materials Chemistry*, 2011, 21, 837-842.

Abstract

We studied solvent-free, one-step functionalization of aligned multi-walled carbon nanotube (MWNTs) using initiated chemical vapor deposition. Aligned MWNTs with a variety of aspect ratios were uniformly functionalized with an epoxy polymer. The vapor deposition process allowed excellent retention of the nanotube alignment and control of the porosity of the resultant MWNT nanostructure. In addition, we transferred the functionalized MWNTs using a flip-over procedure and directly measured the mechanical properties of the transferred MWNTs using nanoindentation. The transferring process created a synergistic effect by crosslinking the polymer coatings sheathed around the aligned nanotubes and forming strong adhesion between the nanotubes and the target substrate. As a result, the elastic modulus of the transferred MWNT nanostructure was improved 650% and the nanoindentation hardness improved 92% compared with the MWNT nanostructure before transferring. The transferred MWNT nanostructure also demonstrated significantly enhanced stability towards wetting and drying. The combination of surface functionality, nanotube alignment, controlled porosity, and enhanced mechanical robustness in the MWNT nanostructures may greatly impact the fabrication of carbon nanotube devices.

3.1 Introduction

Thin films of carbon nanotubes (CNTs) have important applications in devices such as chemical and bio-sensors,[1,2] nanoporous membranes,[3-6] dry adhesives,[7,8] and thermal management systems.[9,10] Aligned CNTs, with the vertically oriented structure, offer unique advantages in collective manipulation and easy integration of nanotubes into such devices. To enable applications in sensors and membranes, it is critical that the aligned CNTs have defined surface functionalities with controlled porosity and mechanical robustness in the nanostructure.

Functionalization of non-aligned CNTs has been investigated extensively using both covalent and non-covalent approaches as reviewed.[11] However, functionalization of aligned CNTs remains a challenge due to the difficulty of preserving the desirable alignment. Traditional solution-based functionalization protocols involve use of solvents and dispersion of nanotubes, which usually result in the disruption of the aligned structure.[12] To improve the mechanical stability, gap-filling materials such as spin-on glass and polymers were used to consolidate the aligned CNTs and functionalize the nanotube tips.[3,13] Other methods such as polymer impregnation[2] and *in situ* polymerization[14,15] have been successfully used to incorporate functionalities to CNTs. However, the resulting nanostructures usually have little porosity between neighboring nanotubes.

Vapor-based methods such as microwave discharge and plasma vapor deposition serve as an alternative strategy to functionalize CNTs.[16,17] These solventless methods do not result in collapse[12] or contraction[18] of neighboring nanotubes, as what are

encountered in functionalizing aligned CNTs using solution-based protocols. Aligned MWNTs have been functionalized with the preservation of nanotube alignment using aldehyde plasma vapor deposition[19] and plasma oxidation.[3] However, the high energy input in those plasma processes usually results in partial destruction of delicate functional groups, thus limiting the control of surface functionalities. Recently an initiated chemical vapor deposition (iCVD) method has been used for the surface engineering of high-aspect-ratio pores[20] and microfabricated trenches.[21] During the iCVD process, initiator molecules are thermally decomposed in the vapor phase at a relatively low temperature of 150-180°C, followed by radical polymerization of monomer vapor molecules to produce conformal polymer coatings directly on solid structures. The low energy input in the process limits the bond scission only to initiator molecules and preserves the functionalities in precursor monomers, resulting in successful synthesis of a wide range of functional polymer coatings. [22-25]

To realize the full potential of aligned CNTs, the nanotube assemblies also need to be transferred to target substrates with enhanced substrate adhesion because of the limited choices of substrates for CNT growth and the poor adhesion between the substrate and CNTs.[26,27] The improvement of interfacial adhesion and mechanical robustness has particular importance in enabling applications of aligned CNTs in dry adhesives and thermal interface materials.[28,29] Different approaches have been reported to transfer aligned CNTs to target substrates. Metal pastes were successfully used to establish strong contacts between the CNTs and the target substrates;[27,30] but the processes required flexible substrates or relatively high temperature (270-800°C) for the annealing of metal materials. Aligned CNTs were transferred to gold-coated substrates using the reaction of

oxidized CNTs with self-assembled monolayers.[31] The chemical reaction resulted in two-fold improvement in the interfacial strength at the transferred CNT/gold interface. Single-walled CNTs were transferred to metal substrates using treatment of warm water or etching of hydrofluoric acid.[32,33] Subsequent polymer coating and melting at the interface was needed to ‘‘glue’’ the CNTs to the target substrates. Most of the studies report the morphology change and electrical characterization of transferred CNTs. Direct measurement on the mechanical properties of the transferred CNTs, however, have not been reported.

This paper reports one-step functionalization of aligned multi-walled carbon nanotubes (MWNTs) using an iCVD method. Poly(glycidyl methacrylate) (PGMA), a polymer with epoxy functionality, was used to demonstrate this functionalization concept. The functionalization process not only preserves the alignment of MWNTs, but also enables facile transfer of the functionalized MWNTs with controlled porosity and improved substrate adhesion. Morphology and mechanical characterization of the transferred MWNTs will be presented in this work. The improved mechanical properties and stability will be discussed.

3.2 Experimental

3.2.1 Growth of MWNTs

Vertically aligned carbon nanotubes were prepared on silicon using thermal chemical vapor deposition by pyrolysis of iron phthalocyanine (FePc) under Ar/H_2.[34] Briefly, a predetermined amount of FePc (0.1 – 0.3 g) was placed in the first zone while a

clean silicon plate was placed in the second zone of a dual quartz tube furnace equipped with independent temperature controllers. A flow of Ar/H_2 (1:1 to 1:2 v/v, 20-40 cm^3/min) mixture was introduced into the quartz tube. The second zone was heated to 800-1100ºC and subsequently the temperature of the first zone was increased to 500-600ºC for 2-15 minutes. Thereafter, the first zone was also heated to 800-1100ºC, and both zones were maintained at that temperature for 10-20 minutes. The resulting carbon nanotubes appeared as a black layer on the substrate.

3.2.2 iCVD process

The vapor deposition functionalization was performed in a custom-built iCVD reactor (Sharon Vacuum) with a quartz plate at the top for visual inspection. The reactor was 25 cm in diameter equipped with a water-cooled stage, on which samples were placed on. A Nichrome filament (Ni80/Cr20, Goodfellow) was mounted in a parallel array at 2.5 cm above the stage. During the deposition, the glycidyl methacrylate (GMA) monomer (98%, Aldrich) was vaporized at 50 ˚C in a glass jar, and *tert*-butyl peroxide (TBP, 97%, Aldrich) was vaporized at room temperature. The GMA monomer and the TBP initiator were mixed well and fed into the reactor. The flow rates of the monomer and initiator were regulated by a needle valve and a mass flow controller (MKS, Type 1479A) to be 1.2 sccm and 0.6 sccm, respectively. The Nichrome filament was resistively heated to 150-180˚C, while the substrate temperature was maintained at 30-33 ˚C, as measured by thermocouples (Omega, Type K) directly attached to the substrate. The pressure in the reactor was maintained at 150 mTorr using a throttling butterfly valve (MKS, Type 253B). A silicon wafer was used as a reference surface and placed close to the MWNT samples. The deposition process was monitored by measuring the reference

thickness using interferometry with a 633 nm He-Ne laser. The cycle thickness in interferometry was calibrated using the data obtained from variable-angle spectroscopic ellipsometry. The polymer deposition rate on the reference surface was approximately 50 nm/min.

3.2.3 Transfer of MWNTs

In the MWNT transfer experiments, silicon substrates were used as the target substrates. Both the MWNT films and the target substrates were modified by the iCVD process described above. The functionalized MWNTs and the silicon substrate were then placed in contact using a general-purpose, self-closing tweezer and annealed at 150 ˚C in a vacuum oven for 2 hours. The wetting experiments of the MWNTs films were conducted by immersing each sample in de-ionized water for 2 min and drying in air. The morphology of the MWNT films was observed using a FEI Quanta 600F scanning electron microscope (SEM). The FTIR spectra were collected by a Nicolet 6700 FTIR spectrometer under transmission mode using a DTGS detector over the range of 400-4000 cm^{-1} at 4 cm^{-1} resolution.

3.2.4 Nanoindentation

Nanoindentation measurements were conducted using a Nano Indenter XP system (MTS Systems Corporation). A diamond spherical tip with a radius of 10 μm was used in all the measurements. The nanoindentation tests were conducted in air at 23°C under a relative humidity of about 50%. The resolutions for load and displacement are 50 nN and 0.01 nm, respectively. The maximum load applied was 1mN at a loading rate of 0.0125mN/s, and the measured indenter tip drift rate was within ±0.02nm/s. In all the

nanoindentation tests, the indentation depths were below 300 nm. Films with thicknesses of >2 μm were used to minimize any substrate effects. Four nanoindentation tests were conducted at different locations for each sample, and the load-displacement curves were recorded.

3.3 Results and discussions

3.3.1 Functionalization of aligned MWNTs

Functionalization of aligned MWNTs was performed in an iCVD reactor (Figure 3-1). During deposition, the peroxide initiator was decomposed at the vicinity of the heated filaments, which generated reactive radicals and initiated the polymerization of the functional monomer on each nanotube. Figure 3-2(a-d) shows the morphology of aligned MWNTs before and after the iCVD PGMA functionalization. The aligned MWNTs have an average length of 2.5 μm. Each individual nanotube was observed to be uniformly functionalized by the polymer coating with the aligned nanotube morphology preserved. Some nanotubes bundled together because of the high site-density of nanotubes. Based on the SEM measurements, the average diameter of modified MWNTs was estimated to increase from 70 nm to 120 nm after the iCVD functionalization process. In addition to the functionalization of small-aspect-ratio MWNTs, the iCVD method was extended to functionalization of aligned nanotubes with high aspect ratios. As indicated in Figure 3-2e and 2f, the iCVD PGMA coatings were uniformly deposited on the nanotube sidewalls down to the bottom of the 60-μm MWNT forests. The above observations indicate that during the iCVD functionalization, the monomer vapors and radicals are able to diffuse

into the densely packed nanotube forests and produce polymers directly on the nanotube sidewalls.

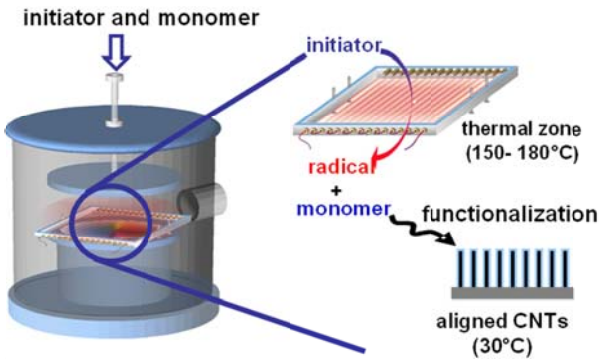

Figure 3-1: Schematic illustration of the iCVD functionalization process of aligned CNTs.

The iCVD method allows functionalization of nanotubes in a controllable manner. As demonstrated in Figure 3-3b and e, with a thin PGMA coating deposited into the MWNT forest, the resulting MWNT film preserved the porosity of the original nanostructure. As the coating thickness increased, the aligned MWNTs became embedded in the polymer matrix and formed a composite film (Figure 3-3c and f). The resultant composite film shows a larger extent of nanotube bundling and significantly smaller porosity compared with the MWNT nanostructure in Figure 3-3a and b. A comparison of the functionalized MWNTs with the pristine MWNTs suggests that the PGMA coating wraps around each nanotube at the beginning of iCVD functionalization, and adjacent nanotubes bundle together as the process proceeds, which eventually can fill

all the interstitial space between nanotubes. By adjusting the deposition time and rate, the porosity of the MWNT-polymer nanostructure can be precisely controlled.

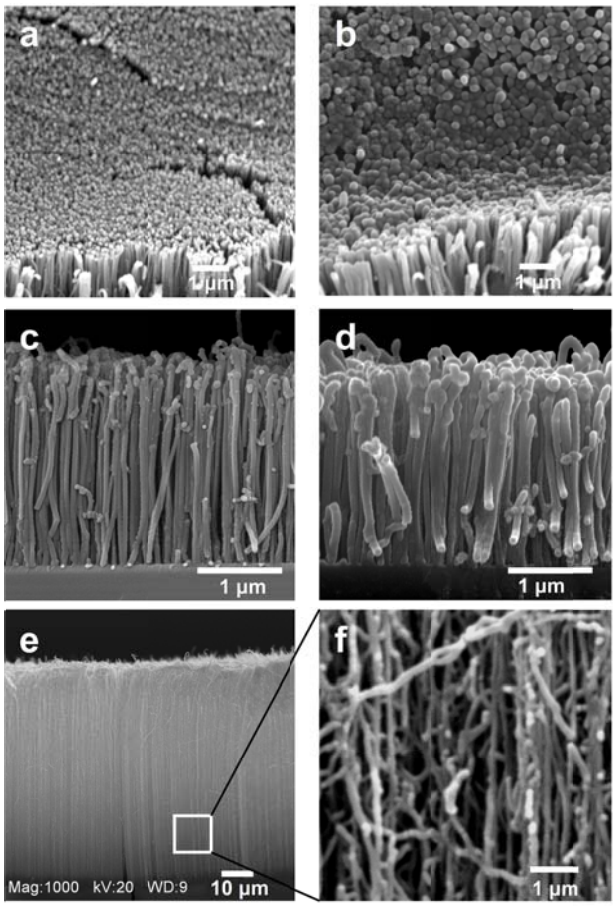

Figure 3-2: SEM images of a) tilted view of pristine aligned MWNTs (nanotube length ca. 2.5 µm); b) tilted view of the functionalized MWNTs; c) cross section of the pristine MWNTs; d) cross section of the functionalized MWNTs; e) functionalized MWNTs with about 60 µm in the nanotube length; f) the enlarged image of the portion at the bottom of the aligned MWNTs.

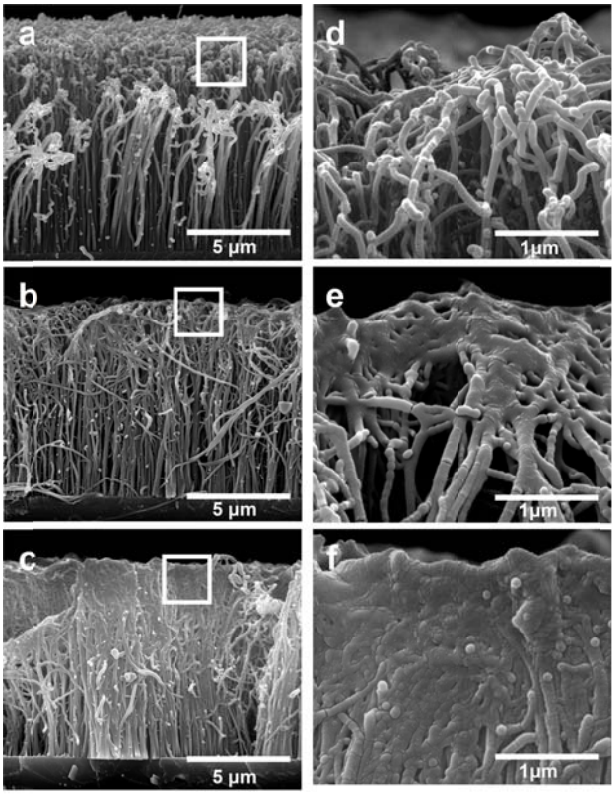

Figure 3-3: Cross section view of a) pristine aligned MWNTs (nanotube length ca. 7 µm); b) iCVD functionalized MWNTs with the porosity preserved; c) iCVD functionalized MWNTs with a much smaller porosity; d), e), and f) enlarged images of the portion indicated by the squares in a), b), and c), respectively.

The iCVD process successfully retained the epoxy functionality in the PGMA film. Figure 3-4 shows the FTIR spectrum of the iCVD PGMA film compared with that of PGMA synthesized using liquid-phase polymerization. The epoxy characteristic absorption peaks at 909, 848, and 760 cm^{-1}, can be clearly identified in the fingerprint region as in the conventionally synthesized PGMA. The iCVD PGMA film can be self-crosslinked at temperatures above the glass transition temperature. As shown in Figure 3-4c, the intensity of the epoxy absorption peaks decreases upon heating at 150˚C, indicating the ring-opening of the epoxy groups and the formation of crosslinks.

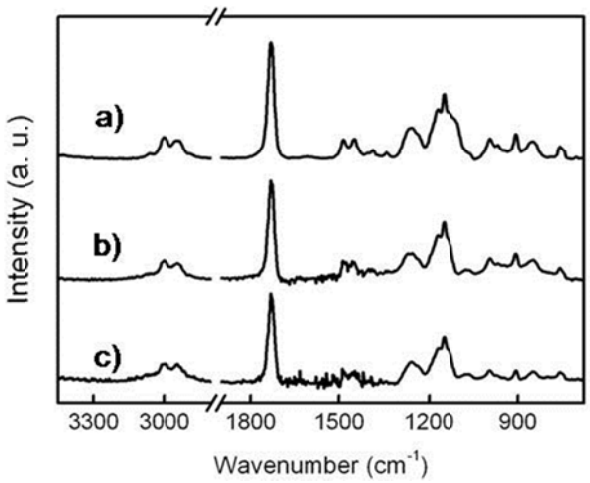

Figure 3-4: FTIR spectra of a) conventionally polymerized PGMA, b) iCVD PGMA as-deposited, and c) iCVD PGMA after annealing at 150°C. The intensity of the peak at 909 cm^{-1} was reduced after annealing.

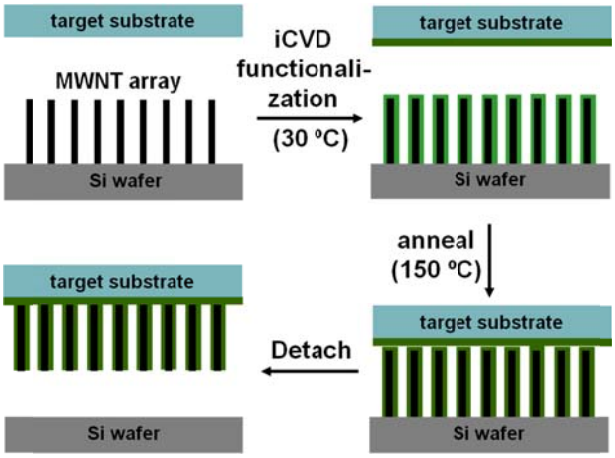

Figure 3-5: Schematics of the MWNT transfer process.

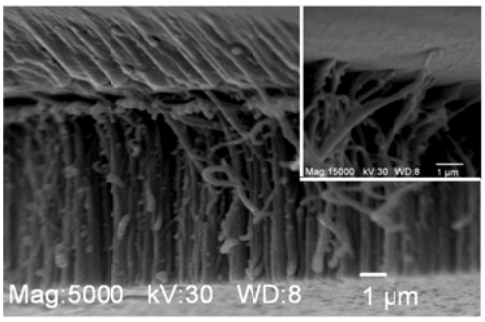

Figure 3-6: Cross section of the transferred MWNTs; inset: closed-up view of the MWNT/substrate interface.

3.3.2 Transfer of aligned MWNTs

The epoxy chemistry incorporated on the aligned MWNTs provides a simple method to transfer the aligned nanotubes to other substrates. The transfer process is illustrated in Figure 3-5. Both the aligned MWNTs and the target substrate were modified with the iCVD PGMA at a thickness of about 50 nm. The modified MWNTs were placed in contact with the target substrate and annealed under vacuum at 150˚C. The crosslinking extent of epoxy groups, X, is calculated to be around 18% from the change of the epoxy absorption peak at 909 cm^{-1} (Figure 3-4) before annealing (A_{909}) and after annealing (A'_{909}): $X = 1 - A'_{909}/ A_{909}$.[24] Because of the self-crosslinking reactions between epoxy groups in PGMA, strong bonding was observed between the aligned MWNTs and the target substrate at the point of contact, which enabled detachment of the aligned MWNTs from the original silicon substrate. Figure 3-6 shows the SEM image of the transferred MWNTs with the nanotube alignment well retained. The inverted nanotubes have the aligned portion exposed at the top, while the entangled portion connected to the substrate - a conFiguration that may be favorable for devices such as sensors and dry adhesives. A

close observation indicates that the entangled part of the MWNTs is firmly connected with the target substrate surface (Figure 3-6, inset).

This transfer process utilizes similar flip-over procedures as the metal welding[27] or polymer wetting[2] transfer method, but with several potential advantages. First, the transfer process does not involve wetting of nanotubes, thus resulting in no contraction of nanotubes as reported in the wetting of aligned CNTs.[18] The method provides control on the porosity of the transferred MWNT nanostructure instead of filling all the spaces between neighboring nanotubes. More importantly, the entire transfer process require neither metal coating nor high temperatures as what used in metal welding, which allows aligned nanotubes to be transferred to a wider variety of substrates. The epoxy reaction with other chemical groups suggests that the PGMA functionalized MWNTs can be transferred to target substrates at temperatures as low as 60°C.[35] Additionally, the un-reacted epoxy groups after the transfer process allows further chemical/biological modification of the transferred MWNTs.

3.3.3 Mechanical properties and wetting stability

Mechanical properties of the functionalized and transferred MWNTs were measured using nanoindentation following standard protocol.[36] Low-aspect-ratio aligned MWNTs (Figure 3-2c) were used to minimize the buckling of nanotubes during nanoindentation.[37] Modulus and hardness of the pristine aligned MWNTs could not be measured due to the collapse of nanotubes. To understand the contribution of the PGMA polymer to the mechanical performance of MWNT-PGMA films, the PGMA film was annealed during the MWNT-PGMA transferring process, and the mechanical properties of both un-

annealed and annealed PGMA films were measured using nanoindentation. The initial portion of the nanoindentation unloading curves of annealed and un-annealed PGMA films showed a negative slope due to the time-dependent nature of polymers. Therefore, the elastic modulus of PGMA films could not be obtained using the standard nanoindentation protocol. Instead, linear viscoelastic analysis[38] was used to extract the relaxation modulus of the PGMA films (supplementary information).

The transferring process significantly improves the mechanical properties of the MWNT-PGMA film, with the elastic modulus increased from 3.4 GPa to 25.8 GPa compared with the film before transfer, and the nanoindentation hardness increase from 0.25 GPa to 0.49 GPa (Figure 3-7). It is noted that the mechanical property enhancement of the MWNT-PGMA film after transferring is significantly higher than that of the PGMA film. For example, the modulus of the PGMA-MWNT film increased more than 650% after annealing and transferring, while the PGMA modulus improved 66% after the same annealing process. Therefore, the modulus enhancement of the MWNT-PGMA film after transferring is only partially due to the stronger support from the crosslinked PGMA. Other features of the MWNT nanostructure, such as the retention of nanotube orientation and the enhanced adhesion at the aligned MWNT/substrate interface, also play an important role in improving the mechanical properties of transferred MWNTs.

The aligned MWNTs can be viewed as reinforcement to the PGMA film. Before transferring, the MWNT-PGMA film showed an increase of 145% in hardness compared with the pristine PGMA film. After the transfer process, the hardness of the annealed MWNT-PGMA films was 252% higher than that of the annealed PGMA film. Since the stiffness of MWNT composite films can be negatively affected by the waviness of

nanotubes,[39] the observed significant enhancement in the stiffness of the MWNT-PGMA film suggests the alignment of nanotubes in the loading direction after the transfer process.

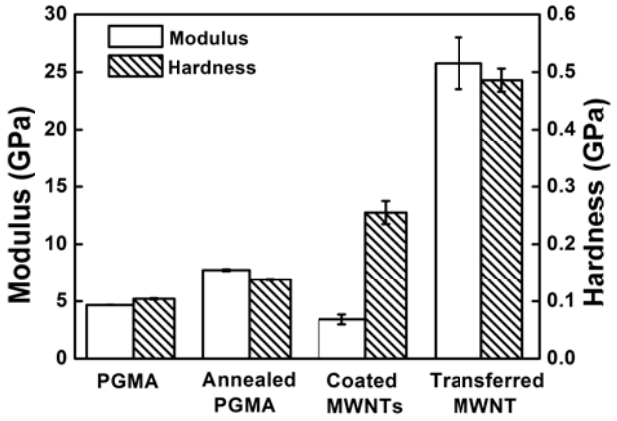

Figure 3-7: Modulus and hardness of the PGMA film, annealed PGMA film, PGMA functionalized MWNTs, and the transferred MWNT-PGMA film measured by nanoindentation. Modulus and hardness of the pristine aligned MWNTs could not be measured due to the collapse of nanotubes.

The wetting stability of the functionalized and transferred MWNTs was investigated and compared with that of the pristine MWNTs. Figure 3-8 shows the SEM images of the aligned MWNTs after water immersion and evaporative drying. The pristine nanotubes collapsed and bundled together due to the capillary force during wetting and drying (Figure 3-8a). The PGMA coating helps alleviate the problem of nanotube collapse by providing mechanical support to the nanotubes. However, the mechanical support is not strong enough to counteract the capillary force, resulting in the formation of nanotube clusters (Figure 3-8b). The transferred MWNTs demonstrated outstanding stability during the wetting and drying processes.. The nanotube alignment was well retained, with no

collapse or clusters observed (Figure 3-8c). Similar to the mechanical property enhancement, the improvement in wetting stability is attributed to the transferring of aligned MWNTs, which crosslinked the PGMA coating sheathed around nanotubes and formed strong epoxy bonding at the MWNT/substrate interface. As a result, the aligned MWNTs possess sufficient mechanical robustness as well as enhanced adhesion to the substrate to overcome the capillary forces during wetting and drying.

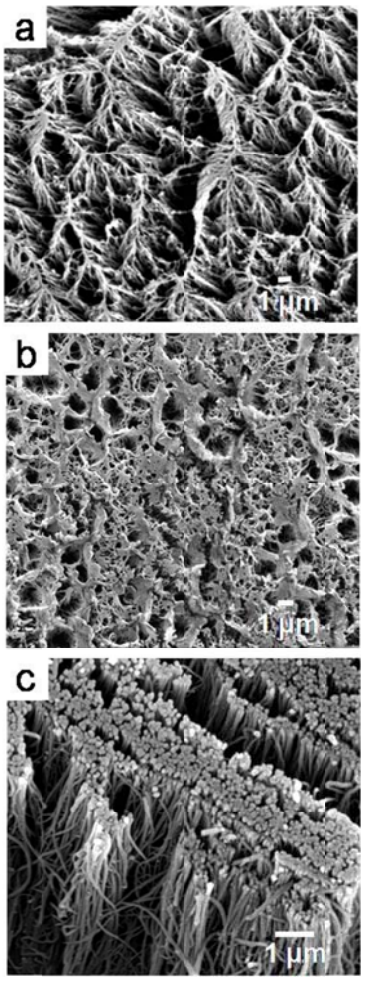

Figure 3-8: SEM images of a) original MWNTs, b) functionalized MWNTs, and c) transferred MWNTs after wetting tests.

3.4 Conclusions

Aligned MWNTs were successfully functionalized by conformal coatings of PGMA using a one-step iCVD process. MWNT forests with a variety of aspect ratios can be functionalized with the aligned structure completely preserved. The iCVD process allows in-situ control of coating thickness and the porosity of the resultant MWNT nanostructure. The MWNT nanostructure was successfully transferred to target substrates through a low-temperature flip-over method. The transferring process retained the nanotube alignment and created a synergistic effect by crosslinking the PGMA coatings sheathed around the nanotubes and forming strong adhesion at the nanotube/substrate interface. The transferred MWNTs demonstrated significantly improved mechanical properties with an elastic modulus of 25.8 GPa and a nanoindentation hardness of 0.49 GPa, while the pristine MWNTs collapsed during nanoindentation. In addition, the transferred MWNTs demonstrated significantly enhanced stability towards wetting. The combination of surface functionality, nanotube alignment, controlled porosity, and enhanced mechanical robustness in the MWNT nanostructures may greatly impact the fabrication of carbon nanotube devices.

3.5 Acknowledgements

Support for this research was provided by the Oklahoma Center for the Advancement of Science and Technology under AR08.2-033. Wang and Lu acknowledge the support of NSF under CMMI-0555902 and CMMI-0826241. We also thank the Oklahoma State University Microscopy Laboratory for SEM observations.

3.6 References

1. Y. Lin, Lu, F., Tu, Y., Ren, Z., *Nano Lett.*, 2004, **4**, 191-195.
2. C. Wei, L. M. Dai, A. Roy and T. B. Tolle, *J. Am. Chem. Soc.*, 2006, **128**, 1412-1413.
3. B. J. Hinds, N. Chopra, T. Rantell, R. Andrews, V. Gavalas and L. G. Bachas, *Science*, 2004, **303**, 62-65.
4. J. K. Holt, H. G. Park, Y. M. Wang, M. Stadermann, A. B. Artyukhin, C. P. Grigoropoulos, A. Noy and O. Bakajin, *Science*, 2006, **312**, 1034-1037.
5. X. S. Li, G. Y. Zhu, J. S. Dordick and P. M. Ajayan, *Small*, 2007, **3**, 595-599.
6. P. Nednoor, V. G. Gavalas, N. Chopra, B. J. Hinds and L. G. Bachas, *J. Mater. Chem.*, 2007, **17**, 1755-1757.
7. L. Ge, S. Sethi, L. Ci, P. M. Ajayan and A. Dhinojwala, *Proc. Natl. Acad. Sci. U. S. A.*, 2007, **104**, 10792-10795.
8. L. Qu and L. Dai, *Adv. Mater.*, 2007, **19**, 3844-3849.
9. M. J. Biercuk, M. C. Llaguno, M. Radosavljevic, J. K. Hyun, A. T. Johnson and J. E. Fischer, *Appl. Phys. Lett.*, 2002, **80**, 2767-2769.
10. H. Huang, C. H. Liu, Y. Wu and S. S. Fan, *Adv. Mater.*, 2005, **17**, 1652-1656.
11. D. Tasis, N. Tagmatarchis, A. Bianco and M. Prato, *Chem. Rev.*, 2006, **106**, 1105-1136.
12. C. V. Nguyen, L. Delzeit, A. M. Cassell, J. Li, J. Han and M. Meyyappan, *Nano Lett.*, 2002, **2**, 1079-1081.
13. P. Nednoor, N. Chopra, V. Gavalas, L. G. Bachas and B. J. Hinds, *Chem. Mater.*, 2005, **17**, 3595-3599.
14. W. Chen, L. Qu, D. Chang, L. Dai, S. Ganguli and A. Roy, *Chem. Commun.*, 2008, **2**, 163-165.
15. Z. H. Yang, Z. Cao, H. Sun and Y. Li, *Adv. Mater.*, 2008, **20**, 2201-2205.
16. B. N. Khare, P. Wilhite, R. C. Quinn, B. Chen, R. H. Schingler, B. Tran, H. Imanaka, C. R. So, C. W. Bauschlicher and M. Meyyappan, *J. Phys. Chem. B*, 2004, **108**, 8166-8172.
17. D. L. Shi, J. Lian, P. He, L. M. Wang, W. J. van Ooij, M. Schulz, Y. J. Liu and D. B. Mast, *Appl. Phys. Lett.*, 2002, **81**, 5216-5218.
18. E. J. Garcia, A. J. Hart, B. L. Wardle and A. H. Slocum, *Adv. Mater.*, 2007, **19**, 2151-2156.
19. Q. D. Chen, L. M. Dai, M. Gao, S. M. Huang and A. Mau, *J. Phys. Chem. B*, 2001, **105**, 618-622.
20. M. Gupta, V. Kapur, N. M. Pinkerton and K. K. Gleason, *Chem. Mater.*, 2008, **20**, 1646-1651.
21. W. E. Tenhaeff, L. D. McIntosh and K. K. Gleason, *Adv. Funct. Mater.*, 2010, **20**, 1144-1151.
22. K. Chan and K. K. Gleason, *Langmuir*, 2005, **21**, 8930-8939.
23. K. K. S. Lau and K. K. Gleason, *Macromolecules*, 2006, **39**, 3688-3694.
24. Y. Mao and K. K. Gleason, *Macromolecules*, 2006, **39**, 3895-3900.
25. Y. Mao and K. K. Gleason, *Langmuir*, 2006, **22**, 1795-1799.
26. C. C. Chiu, T. Y. Tsai and N. H. Tai, *Nanotechnology*, 2006, **17**, 2840-2844.
27. M. J. Kim, N. Nicholas, C. Kittrell, E. Haroz, H. W. Shan, T. J. Wainerdi, S. Lee, H. K. Schmidt, R. E. Smalley and R. H. Hauge, *J. Am. Chem. Soc.*, 2006, **128**, 9312-9313.
28. H. B. Fan, K. Zhang and M. M. F. Yuen, *J. Appl. Phys.*, 2009, **106**, 034307.
29. S. K. Pal, Y. Son, T. Borca-Tasciuc, D. A. Borca-Tasciuc, S. Kar, R. Vajtai and P. A. Ajayan, *J. Mater. Res.*, 2008, **23**, 2099-2105.
30. L. B. Zhu, Y. Y. Sun, D. W. Hess and C. P. Wong, *Nano Lett.*, 2006, **6**, 243-247.
31. W. Lin, Y. H. Xiu, H. J. Jiang, R. W. Zhang, O. Hildreth, K. S. Moon and C. P. Wong, *J. Am. Chem. Soc.*, 2008, **130**, 9636-9637.
32. Y. Murakami and S. Maruyama, *Chem. Phys. Lett.*, 2006, **422**, 575-580.

33. G. Y. Zhang, D. Mann, L. Zhang, A. Javey, Y. M. Li, E. Yenilmez, Q. Wang, J. P. McVittie, Y. Nishi, J. Gibbons and H. J. Dai, *Proc. Natl. Acad. Sci. U. S. A.*, 2005, **102**, 16141-16145.
34. S. D. Huang, L.; Mau, W.H., 1999, **103**, 4223-4227.
35. S. G. Im, K. W. Bong, C. H. Lee, P. S. Doyle and K. K. Gleason, *Lab on a Chip*, 2009, **9**, 411-416.
36. *Theory of Instrumented Indentation Testing*, Customer Care Kit, MTS Systems Corporation, Oak Ridge, TN, 2000.
37. C. P. Deck, J. Flowers, G. S. B. McKee and K. Vecchio, *J. Appl. Phys.*, 2007, **101**, 023512.
38. H. Lu, B. Wang, J. Ma, G. Huang and H. Viswanathan, *Mech. Time-Depend. Mater.*, 2003, **7**, 189-207.
39. N. R. Raravikar, A. S. Vijayaraghavan, P. Keblinski, L. S. Schadler and P. M. Ajayan, *Small*, 2005, **1**, 317-320.

3.7 Supporting information

Nanoindentation measurement

The elastic modulus (E) and the Hardness (H) are the basic properties measured by nanoindenter system. The hardness (H) is determined using the equation[1]:

$$H = P / A$$

where P is the applied load and A is the projected contact area at that load. The elastic modulus (E) is determined from the reduced modulus E_r using the expression[1]:

$$\frac{1}{\mathrm{E_r}} = \frac{(1-v^2)}{E} + \frac{(1-v_i^2)}{E_i}$$

where v is the Poisson's ratio for the test material and E_i and v_i are the elastic modulus and Poisson's ratio of the indenter. The reduced modulus E_r is given by[1]:

$$E_r = \frac{(\sqrt{\pi} \cdot S)}{2\beta\sqrt{A}}$$

where β is a constant related to the indenter geometry and S is the slope of the initial portion of the unloading curve. For the transferred MWNT-PGMA nanostructure, the recorded elastic modulus was 25.7±1.7 Gpa and the hardness was 0.46±0.05 Gpa.

Reference:

1. *Theory of Instrumented Indentation Testing*. Customer Care Kit, MTS Systems Corporation: Oak Ridge, TN, 2000.

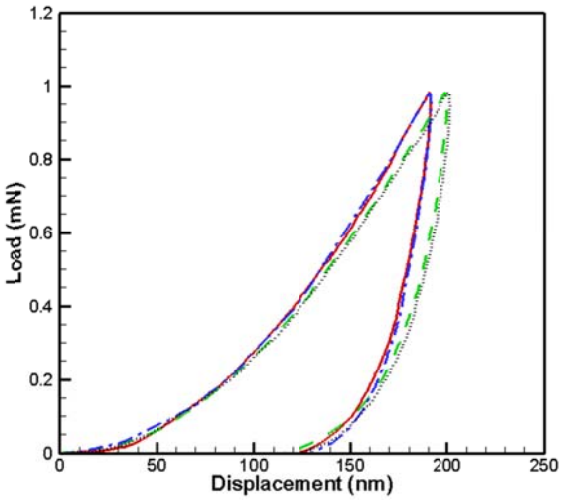

Figure S3-1 Indentation load-displacement curves.

CHAPTER IV

COVALENT FUNCTIONALIZATION OF ALIGNED SINGLE WALLED CARBON NANOTUBES BY VAPOR-DEPOSITED POLYMER COATINGS

Y. Mao, Y. M. Ye, W. L. Zhang, K. Kalkan, D. E. Resasco, "Covalent Functionalization of Aligned Single Walled Carbon Nanotubes by Vapor-Deposited Polymer Coatings", *Journal of Physical Chemistry C*. (In preparation)

Abstract

We report covalent functionalization of vertically aligned single walled carbon nanotubes (SWNTs) using a novel vapor-based method. By introducing initiator and monomer in the vapor phase, free radical polymerization occurred on the surface of SWNTs, resulting in thin polymer coatings sheathed around nanotubes with controlled thickness. The mild and solventless nature of the deposition process well-preserved the aligned morphology and retained the delicate functional groups from the monomer. Further study proved covalent grafting of polymer coatings to the SWNTs during the functionalization process, manifested by the evidences of: 1) the increase of the intensity ratio of D- to G-band in the SWNT Raman spectra after functionalization; 2) the decreased frequency-dependent electric conductivity of the SWNT film measured by terahertz time-domain spectroscopy (THz-TDS). Through the THz-TDS measurement and modeling, we also demonstrated the decrease of the metallic behavior of the SWNT film after polymer grafting, indicating the possibility of tailoring the chemical and electronic properties of aligned SWNT films using a solvent-free approach.

4.1 Introduction

Single walled carbon nanotubes (SWNTs) have demonstrated great promise in nanofabrication due to their unique anisotropic electrical and optical properties.[1-3] The aligned single walled carbon nanotube (ASWNT) ensembles offer the advantage of collective manipulation and integration in device fabrications.[4-7] To further the application of SWNTs, covalent functionalization is desired to tailor the specific electronic[8-10] and chemical[11,12] properties and to improve the nanotube biocompatibility. Though random SWNTs have been successfully functionalized using solution- and vapor-based schemes, studies in covalent functionalization of ASWNT films have been limited due to the difficulties of nanotube wetting and alignment disruption.

Radical chemistry has been widely investigated using solution-based methods in covalent functionalization of SWNTs. Radicals generated from reaction of diazonium salts[13,14] or thermal decomposition of peroxides[15-17] were reported to covalently bond to SWNTs and change their electronic state. Polymer radicals were also grafted to the nanotubes through the *in-situ* "grafting to"[18,19] and "grafting-from"[20-22] methods. However, these functionalization processes usually require the use of solvents (e.g. organic solvents or strong acids) for nanotube dispersion and treatment, long reaction time (2-120 h), and/or multiple processing steps, which are incompatible with the functionalization of aligned SWNTs.

Solventless methods have also been reported to functionalize SWNTs with the assist of plasma or high temperature. Covalent bondings between carbon atoms and H,[23,24] F,[25-27] and N[28,29] have been created by flowing vapors of H_2, CF_4, and NH_3 in a plasmatic environment, respectively. Further study showed tuned electronic and optical

properties of SWNTs after functionalization.[9,30-32] These vapor-based methods require much simpler treatments than solution-based methods in SWNT functionalization, and exert less disruption to the original SWNT morphology. However, plasma- and heat-based processes impose high energy on the side walls and end caps of SWNTs, resulting in difficulties in undesired defect sites and even tube fragmentation.[33] Moreover, although plasma-assisted methods are fully capable of covalently functionalizing SWNTs with small molecules, polymeric functionalization is rarely studied, as the plasma process lacks the control of stoichiometric chemistry.[34]

In this study, we report covalent functionalization of vertically aligned SWNTs via a single-step, vapor-based, polymer grafting method. The vapor-phase grafting method overcomes the problems of both solution-based and plasma-assisted functionalization methods listed above by combining the radical polymerization chemistry with the vapor deposition process to graft polymers directly to SWNTs. The bypass of any solvent treatment enables a complete preservation of the aligned morphology. We investigate how the vapor grafting process affects the structural and electronic properties of ASWNTs using Raman spectroscopy and terahertz time-domain spectroscopy (THz-TDS). THz-TDS is a non-contact, non-destructive technique that can directly interact with bulk electronic systems and characterize the cumulative electronic properties of ASWNTs; which therefore represents a more practical approach towards realistic applications. We study the electric conductivity of the ASWNT film before and after functionalization, and fit the experimental results using an effective medium approximation.

4.2 Experimental Section

4.2.1 Synthesis of ASWNTs

The ASWNTs were synthesized by plasma chemical vapor deposition.[7,35] Catalyst thin film was deposited on a pre-cut p-type Si wafer (from Montco Silicon Technologies, Inc.) by dropping and self-spreading of isopropanol solution containing Co and Mo followed by slow drying in a pseudo-saturate environment. The wafer with catalyst was then baked in a convection oven at 100^{o}C for 10 min and calcined at 500^{o}C for 15 min. After pretreatment, the wafer was placed in a quartz reactor oriented parallel to the direction of flowing gases. Prior to forming SWNT by the CO disproportionation reaction, the catalyst was heated in H_2 flow from room temperature to 500 °C, and then in He flow up to 750 ^{o}C. Subsequently, the flow of pure CO was fed in to initiate the growth at atmospheric pressure. The flow rate was kept at 1,000 sccm for each gas. The synthesized ASWNTs were purified by heating to 600 °C in Helium with an O_2 flow rate of 10 sccm.

4.2.2 Vapor-based Functionalization

The vapor-based functionalization was carried out in a custom-built iCVD reactor (Sharon Vacuum) as previously reported.[36] Briefly, glycidyl methacrylate (GMA) monomer (98%, Aldrich) and *tert*-butyl peroxide (TBP, 97%, Aldrich) were vaporized at 50 ˚C and room temperature in glass jars, and fed into the reactor by the regulation of a manual needle valve and a mass flow controller (MKS, Type 1479A) at the flow rate of 1.2 sccm and 0.6 sccm, respectively. The reactor was equipped with a parellelly arrayed filament (Ni80/Cr20, Goodfellow) and circulating water to quench the stage. The filament was placed 1.5 cm above the stage to enhance the access of radicals to the

SWNTs. During deposition, the Nichrome filament was resistively heated to 150˚C, while the substrate temperature was maintained at 30-33 ˚C, as measured by directly attached thermocouples (Omega, Type K). The pressure in the reactor was maintained at 250 mTorr using a throttling butterfly valve (MKS, Type 253B). The deposition process was monitored by an interferometry system with a 633 nm He-Ne laser.

4.2.3 Characterizations

The morphology of the ASWNT films was observed using a FEI Quanta 600F scanning electron microscope (SEM). The FTIR spectrum of the polymer coating was collected by a Nicolet 6700 FTIR spectrometer under the transmission mode using a DTGS detector over the range of 400-4000 cm^{-1} at 4 cm^{-1} resolution. Since the IR absorption of the ASWNT film exceeds the detection limit, FTIR spectrum of polymer coatings on a reference Si wafer, which was placed close to the ASWNT sample during deposition, was collected instead. Raman scattering spectra were acquired using a Renishaw RM 1000 micro-Raman spectrometer at its SynchroScan Mode equipped with a 514 nm Ar+ ion laser. Back-scattered radiation was collected employing a 50X objective lens of 0.85 numerical aperture and analyzed with a 1800 lines/mm grating and a Peltier-cooled (-70 C) RenCam CCD array detector (576×384 pixels). A slit width of 60 μm was employed. For rejection of the Rayleigh scattered light, a holographic notch filter was employed. The signal was integrated for 10 s under 7.5 mW incident laser power.

The electric conductivity of pristine and functionalized ASWNT films were experimentally characterized by broadband terahertz time-domain spectroscopy (THz-TDS) transmission measurements.[37] The experimental setup of the THz-TDS is

illustrated in Figure S4-1. By using four paraboloidal mirrors, the photoconductive switch-based THz-TDS system was arranged into an 8-F confocal geometry, which enables terahertz beam coupling between the transmitter and receiver and compresses the beam to a frequency-independent waist with a diameter of 3.5 mm. The samples were placed midway between the transmitter and receiver modules at the waist of the terahertz beam. The THz-TDS system has a usable bandwidth of 0.1-4.5 THz (3 mm-67μm) and a signal to noise ratio (S/N) of >15,000:1.[38]

4.3 Results and Discussions

4.3.1 Vapor-based Functionalization

Figure 4-1 illustrates the vapor-based functionalization of ASWNTs. During the deposition process, the initiator molecules of *tert*-butyl peroxide in the reactor chamber were thermally decomposed in the vapor phase at 150°C to generate radicals such as *tert*-butoxy. The initiation was followed by an addition reaction of monomer vapor molecules to produce polymer radicals, which directly react with the sidewalls of the nanotubes. Using acrylic monomers with glycidyl groups, we show how the ASWNTs are functionalized with epoxy chemistry. The low energy input (3-4 W/cm^2) in the process limits the bond scission only to the initiator molecules, thus preserving the functionalities in the monomers.[39-41] FTIR spectrum of the synthesized poly(glycidyl methacrylate) (PGMA) coating (Figure S2) revealed excellent retention of the carbonyl (1732 cm^{-1}) and epoxy (909, 848, and 760 cm^{-1}) groups, which is in good agreement with previously reported PGMA coatings on multiwall carbon nanotubes.[36]

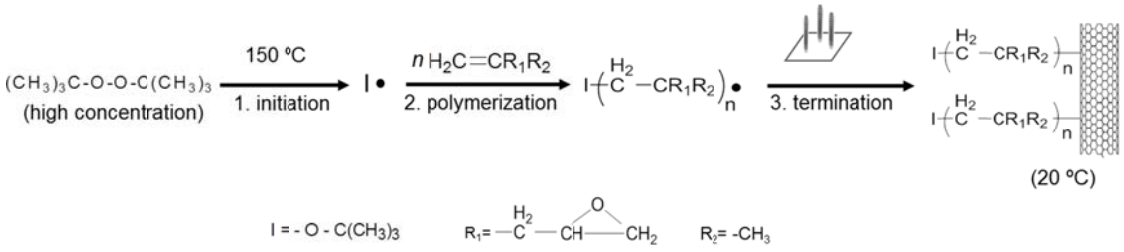

Figure 4-1 Functionalization of aligned SWNTs through vapor-based polymer grafting.

Figure 4-2 shows the SEM images of the pristine and functionalized ASWNT films. Slight bundling between adjacent nanotubes was observed in the pristine ASWNT film due to the Van der Waals force. The solventless functionalization process allowed a complete preservation of the aligned morphology as seen in Figure 4-2b and c. Uniform polymer coatings sheathed around the nanotubes with a slight accumulation at the ends. The porosity of the ASWNT film was retained with a thin PGMA coating. As the deposition proceeded, the space between nanotubes was gradually filled by the coating, which eventually resulted in a polymer composite filled with aligned SWNTs (Figure 4-2c). Because of the mild conditions it employs, the vapor functionalization method poses minimal damage to the SWNTs, as opposed to many solution-based functionalization schemes, which may cause the shortening and end opening of nanotubes.

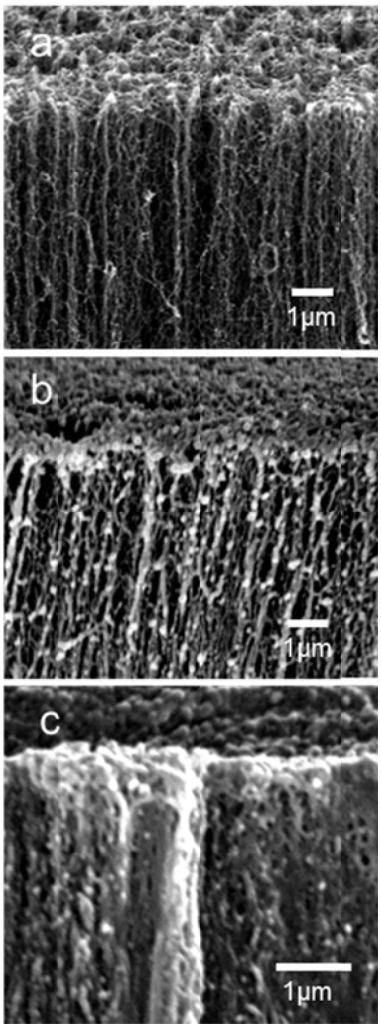

Figure 4-2 SEM images of a) pristine ASWNT film, b) and c) functionalized ASWNT films with different polymer coating thicknesses.

4.3.2 Raman Spectra of Functionalized SWNTs.

Figure 4-3a shows the Raman spectra of SWNTs at the tangential mode before and after functionalization. The intensity ratio (I_D/I_G) of the D-band (1335 cm^{-1}) to G-band (1591 cm^{-1}) increased by a factor of 1.6 after functionalization. The increase of I_D/I_G is not as prominent as that of heavily functionalized SWNTs,[13,14] but comparable with the

increase in polymer grafted SWNTs.[42-44] Since the D band represents the degree of sp^3 hybridization of carbon atoms, this increase of I_D/I_G in functionalized ASWNTs indicates the disruption of the Π-conjugated electronic structure due to the partial conversion of C=C bonds to C-C bonds in SWNTs. The conversion suggests the creation of covalent bonding between the carbon atoms on the SWNTs and the polymer radicals during the vapor grafting process.

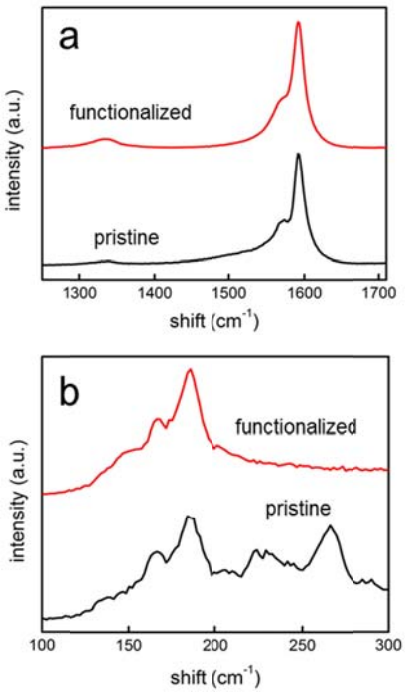

Figure 4-3 Raman spectra of pristine and functionalized ASWNT films at a) tangential mode and b) radial breathing mode.

We further studied the Raman spectra of aligned SWNTs at the radial breathing mode (RBM) from 100 to 300 cm^{-1} (Figure 4-3b). The RBM mode corresponds to the coherent vibration of carbon atoms in the radial direction with the vibration frequency

inversely proportional to the diameter of SWNTs.[45] Two major peaks at 185 and 268 cm^{-1} and several small peaks were observed in the RBM range of pristine ASWNTs, while only peaks below 200 cm^{-1} was observed in PGMA-functionalized ASWNTs. The depression of peaks in the higher frequency range after functionalization is attributed to the loss of resonance resulting from the disruption of the symmetric distribution of sp^3-sites.[46] This depression indicates that vapor-based covalent modification is more favorable to the SWNTs with smaller diameter, since carbon atoms in smaller SWNTs bare more strains and are thus more reactive. This finding is in agreement with previous studies.[17,47,48]

4.3.3 Electric Conductivity of Functionalized ASWNTs.

The effect of vapor grafting on the electric conductivity of ASWNTs was investigated using THz-TDS, which has been demonstrated to be an efficient characterization method in probing the dielectric response as well as the electric properties of SWNT films.[31,32,49-53] The terahertz pulses transmitted through the reference, pristine and functionalized ASWNT films, and the spectra of the transmitted pulses were recorded. The power absorption coefficients (α) and refractive indices (n) of the ASWNT films were subsequently derived from the obtained spectra. The detailed derivation process is described in the supporting information. The frequency-dependent complex dielectric constant (ε_{eff}) of the ASWNT film samples can be expressed using the general function

$$\varepsilon_{eff} = \varepsilon_{eff}^{\infty} + i\sigma/(\omega\varepsilon_0) = (n_r + in_i)^2 \quad (4\text{-}1)$$

where $\varepsilon_{eff}^{\infty}$ is the dielectric constant of the films at infinity; σ is the frequency-dependent

complex conductivity; ω is the frequency; ε_0 is the free-space permittivity; and n_r and $n_i = \alpha\lambda/4\pi$ are the real and imaginary index of refraction, respectively. The real and imaginary conductivity of the pristine and functionalized ASWNT films were thus calculated using equation (4-1) and plotted as the data points shown in Figure 4-4.

Considering the ASWNT film as a system of SWNTs embedded in an air medium, we then model the films using the effective medium approximation (EMA) with Maxwell-Garnett (MG) model:[49,50]

$$\varepsilon_{eff} = \frac{[N + f(1-N)]\varepsilon_{SWNT} + (1-N)(1-f)}{N(1-f)\varepsilon_{SWNT} + (fN + 1 - N)} \tag{4-2}$$

where f and N are the volume and geometrical factors of the MG Model obtained from the best fitting, and ε_{SWNT} is the intrinsic dielectric constant of the SWNTs. Since the SWNTs can be assumed as a mixture of both metallic and semiconducting nanotubes with slight bundling and cross junctions, the intrinsic dielectric function of the SWNTs can be given by the Drude-Lorentzian (DL) model:[49,50,54]

$$\varepsilon_{SWNT}(\omega) = \varepsilon_{SWNT}^{\infty} - \frac{\omega_p^2}{\omega(\omega + i\Gamma)} + \sum_j \frac{\omega_{pj}^2}{(\omega_j^2 - \omega^2) - i\Gamma_j\omega} \tag{4-3}$$

where $\varepsilon_{SWNT}^{\infty}$ is the intrinsic dielectric constant of SWNTs at infinity, ω_p and Γ are the plasma frequency and damping rate, respectively, ω_{pj}, ω_j and Γ_j are the center frequency, spectral width, and oscillator strength, respectively. The first two terms in equation (4-3) represent the Drude model for metals, and the third term represents Lorentz oscillators for semiconductors. Both the Drude and Lorentz oscillator terms are introduced, because the dielectric properties of SWNTs are determined by both free and bound electrons. The fitting parameters for the measurements are listed in Table S4-1.

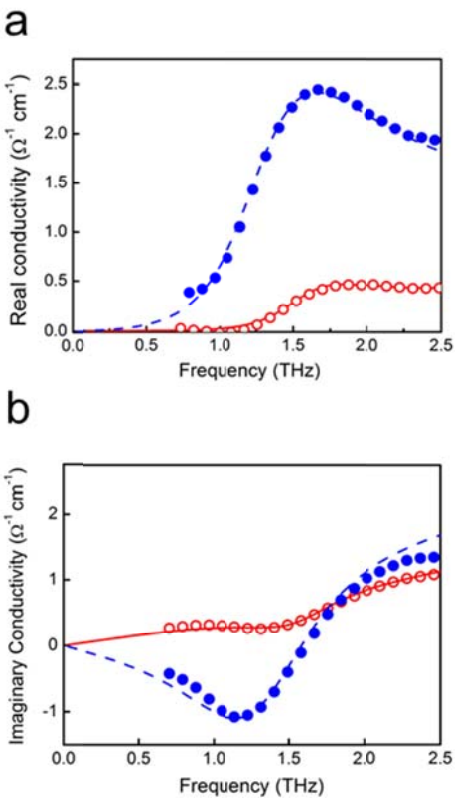

Figure 4-4 Comparison of measurements (dots: pristine ASWNT film; circles: PGMA-functionalized ASWNT film) with theoretical model (dashed lines: pristine ASWNT film; solid lines: PGMA-functionalized ASWNT film): (a) real part of conductivity and (b) imaginary part of conductivity of the ASWNT films.

Figure 4-4 shows the real and imaginary conductivity of the pristine and functionalized ASWNT films compared with the theoretical model. A good fit is achieved using the combination of the DL and MG models for both pristine and functionalized ASWNT films. In the simple Drude model, the conductivity of metals decreases with the increase of electromagnetic frequency.[51] However, similar to previous reports,[31,49,50] an increase of the real conductivity was observed up to 1.7 THz in the pristine ASWNT film. This disagreement confirms that the SWNT film in our study is a mixture of metallic and semiconductor nanotubes with contact junctions, and the

dielectric property cannot be solely explained by the Drude model. The maximum conductivity of the pristine ASWNT film was achieved at 1.7 THz, while the previous reports revealed resonance peaks of SWNT films differing from 0.4 to 1.2 THz.[32,49,50] The difference may originate from the density, synthetic method, and alignment of different SWNT samples.

The vapor-based functionalization resulted in a decrease in the real conductivity to approximately one sixth of that of the pristine ASWNT film within the entire frequency range. Similar findings have been reported on the fluorine- and hydrogen-functionalized SWNTs, where the conductivity decreases were up to one order magnitude and 40% for the F- and H-functionalization processes, respectively.[31,32] The decrease of the conductivity is attributed to the reduced concentration of free electrons, caused by the creation of covalent bonding between the polymer radicals and SWNTs. In addition, the closer resemblance of the fitted real conductivity curve to the Lorentz oscillator curve than to that of the simple Drude model[50] suggests that the covalent functionalization has weakened the metallic behavior of SWNTs, which has also been reported in other vapor-functionalized SWNTs.[9,31] The THz-TDS observation is in good agreement with the results from Raman spectroscopy.

4.4 Conclusions

This paper demonstrates a vapor-based functionalization method that covalently grafts functional polymers to aligned single walled carbon nanotubes. The grafting process employed a mild solventless functionalization environment, which enabled a complete preservation of the nanotube alignment and minimal damage to the individual

nanotubes. The covalent functionalization resulted in a partial conversion of sp^2 to sp^3 hybridization of carbon atoms, manifested by an increased intensity ratio of D- to G-band in the Raman spectra. Further evidence of the covalent grafting was provided by the reduced electric conductivity of the ASWNT film as measured by terahertz time-domain spectroscopy. The measured real and imaginary conductivities were fit using the combination of the Drude-Lorentizan and Maxwell-Garnett model. From the theoretical fitting, a weakened metallic property of the ASWNT film was observed after functionalization. The vapor-based polymer grafting method offers a convenient approach towards the modulation of electronic property and surface functionality of ASWNTs without the assist of any solvent, suggesting promising applications in the ASWNT-based device fabrications.

4.5 Acknowledgements.

Support for this research was provided by the Oklahoma Center for the Advancement of Science and Technology under AR08.2-033.

4.6 References:

1. W. Y. Zhou, X. D. Bai, E. G. Wang and S. S. Xie, *Adv. Mater.*, 2009, **21**, 4565-4583.
2. M. Ouyang, J. L. Huang and C. M. Lieber, *Accounts of Chemical Research*, 2002, **35**, 1018-1025.
3. Z. Chen, X. B. Zhang, R. H. Yang, Z. Zhu, Y. Chen and W. H. Tan, *Nanoscale*, 2011, **3**, 1949-1956.
4. Z. Liu, L. Jiao, Y. Yao, X. Xian and J. Zhang, *Adv. Mater.*, 2010, **22**, 2285-2310.
5. P. Diao and Z. Liu, *Adv. Mater.*, 2010, **22**, 1430-1449.
6. K. Hata, D. N. Futaba, K. Mizuno, T. Namai, M. Yumura and S. Iijima, *Science*, 2004, **306**, 1362-1364.
7. L. Zhang, Y. Q. Tan and D. E. Resasco, *Chem. Phys. Lett.*, 2006, **422**, 198-203.
8. K. Kamaras, M. E. Itkis, H. Hu, B. Zhao and R. C. Haddon, *Science*, 2003, **301**, 1501-1501.
9. K. S. Kim, D. J. Bae, J. R. Kim, K. A. Park, S. C. Lim, J. J. Kim, W. B. Choi, C. Y. Park and Y. H. Lee, *Adv. Mater.*, 2002, **14**, 1818-1821.
10. J. E. Fischer, *Accounts of Chemical Research*, 2002, **35**, 1079-1086.
11. X. H. Peng and S. S. Wong, *Adv. Mater.*, 2009, **21**, 625-642.
12. C. S. Yeung, W. Q. Tian, L. V. Liu and Y. A. Wang, *Journal of Computational and Theoretical Nanoscience*, 2009, **6**, 1213-1235.
13. B. K. Price, J. L. Hudson and J. M. Tour, *J. Am. Chem. Soc.*, 2005, **127**, 14867-14870.
14. J. L. Bahr, J. P. Yang, D. V. Kosynkin, M. J. Bronikowski, R. E. Smalley and J. M. Tour, *J. Am. Chem. Soc.*, 2001, **123**, 6536-6542.
15. P. S. Engel, W. E. Billups, D. W. Abmayr, K. Tsvaygboym and R. Wang, *J. Phys. Chem. C*, 2008, **112**, 695-700.
16. H. P. Peng, P. Reverdy, V. N. Khabashesku and J. L. Margrave, *Chemical Communications*, 2003, 362-363.
17. P. Umek, J. W. Seo, K. Hernadi, A. Mrzel, P. Pechy, D. D. Mihailovic and L. Forro, *Chemistry of Materials*, 2003, **15**, 4751-4755.
18. Y. Q. Liu, Z. L. Yao and A. Adronov, *Macromolecules*, 2005, **38**, 1172-1179.
19. X. D. Lou, C. Detrembleur, C. Pagnoulle, R. Jerome, V. Bocharova, A. Kiriy and M. Stamm, *Adv. Mater.*, 2004, **16**, 2123-+.
20. Z. L. Yao, N. Braidy, G. A. Botton and A. Adronov, *J. Am. Chem. Soc.*, 2003, **125**, 16015-16024.
21. G. Viswanathan, N. Chakrapani, H. C. Yang, B. Q. Wei, H. S. Chung, K. W. Cho, C. Y. Ryu and P. M. Ajayan, *J. Am. Chem. Soc.*, 2003, **125**, 9258-9259.
22. S. H. Qin, D. Q. Qin, W. T. Ford, J. E. Herrera and D. E. Resasco, *Macromolecules*, 2004, **37**, 9963-9967.
23. G. Y. Zhang, P. F. Qi, X. R. Wang, Y. R. Lu, D. Mann, X. L. Li and H. J. Dai, *J. Am. Chem. Soc.*, 2006, **128**, 6026-6027.
24. B. N. Khare, M. Meyyappan, A. M. Cassell, C. V. Nguyen and J. Han, *Nano Letters*, 2002, **2**, 73-77.
25. N. O. V. Plank, G. A. Forrest, R. Cheung and A. J. Alexander, *J. Phys. Chem. B*, 2005, **109**, 22096-22101.
26. L. Valentini, D. Puglia, I. Armentano and J. M. Kenny, *Chem. Phys. Lett.*, 2005, **403**, 385-389.
27. N. O. V. Plank, L. D. Jiang and R. Cheung, *Applied Physics Letters*, 2003, **83**, 2426-2428.
28. B. Khare, P. Wilhite, B. Tran, E. Teixeira, K. Fresquez, D. N. Mvondo, C. Bauschlicher and M. Meyyappan, *J. Phys. Chem. B*, 2005, **109**, 23466-23472.
29. B. N. Khare, P. Wilhite, R. C. Quinn, B. Chen, R. H. Schingler, B. Tran, H. Imanaka, C. R. So, C. W. Bauschlicher and M. Meyyappan, *J. Phys. Chem. B*, 2004, **108**, 8166-8172.

30. L. Dumitrescu, N. R. Wilson and J. V. Macpherson, *J. Phys. Chem. C*, 2007, **111**, 12944-12953.
31. T. I. Jeon, J. H. Son, K. H. An, Y. H. Lee and Y. S. Lee, *Journal of Applied Physics*, 2005, **98**.
32. C. Kang, I. H. Maeng, S. J. Oh, S. C. Lim, K. H. An, Y. H. Lee and J.-H. Son, *Physical Review B*, 2007, **75**.
33. Y. H. Yan, M. B. Chan-Park, Q. Zhou, C. M. Li and C. Y. Yue, *Applied Physics Letters*, 2005, **87**.
34. H. O. Pierson, *Handbook of chemical vapor depostion: principles, technology and applications*, Noyes Publications, Norwich, 1999.
35. G. Lolli, L. A. Zhang, L. Balzano, N. Sakulchaicharoen, Y. Q. Tan and D. E. Resasco, *J. Phys. Chem. B*, 2006, **110**, 2108-2115.
36. Y. Ye, Y. Mao, F. Wang, H. Lu, L. Qu and L. Dai, *Journal of Materials Chemistry*, 2011, **21**, 837-842.
37. D. Grischkowsky, S. Keiding, M. Vanexter and C. Fattinger, *Journal of the Optical Society of America B-Optical Physics*, 1990, **7**, 2006-2015.
38. A. K. Azad, J. M. Dai and W. L. Zhang, *Optics Letters*, 2006, **31**, 634-636.
39. S. H. Baxamusa, S. G. Im and K. K. Gleason, *PCCP*, 2009, **11**, 5227-5240.
40. K. K. S. Lau and K. K. Gleason, *Adv. Mater.*, 2006, **18**, 1972-+.
41. Y. Mao and K. K. Gleason, *Langmuir*, 2004, **20**, 2484-2488.
42. S. H. Qin, D. Q. Qin, W. T. Ford, J. E. Herrera, D. E. Resasco, S. M. Bachilo and R. B. Weisman, *Macromolecules*, 2004, **37**, 3965-3967.
43. S. H. Qin, D. Q. Qin, W. T. Ford, D. E. Resasco and J. E. Herrera, *Macromolecules*, 2004, **37**, 752-757.
44. S. H. Qin, D. Q. Oin, W. T. Ford, D. E. Resasco and J. E. Herrera, *J. Am. Chem. Soc.*, 2004, **126**, 170-176.
45. M. S. Dresselhaus, G. Dresselhaus, R. Saito and A. Jorio, *Physics Reports-Review Section of Physics Letters*, 2005, **409**, 47-99.
46. R. Graupner, *Journal of Raman Spectroscopy*, 2007, **38**, 673-683.
47. P. Nikolaev, M. J. Bronikowski, R. K. Bradley, F. Rohmund, D. T. Colbert, K. A. Smith and R. E. Smalley, *Chem. Phys. Lett.*, 1999, **313**, 91-97.
48. A. M. Rao, E. Richter, S. Bandow, B. Chase, P. C. Eklund, K. A. Williams, S. Fang, K. R. Subbaswamy, M. Menon, A. Thess, R. E. Smalley, G. Dresselhaus and M. S. Dresselhaus, *Science*, 1997, **275**, 187-191.
49. H. G. Han, Z. Y. Zhu, Z. X. Wang, W. Zhang, L. P. Yu, L. T. Sun, T. T. Wang, F. He and Y. Liao, *Physics Letters A*, 2003, **310**, 457-459.
50. T. I. Jeon, K. J. Kim, C. Kang, I. H. Maeng, J. H. Son, K. H. An, J. Y. Lee and Y. H. Lee, *Journal of Applied Physics*, 2004, **95**, 5736-5740.
51. T. I. Jeon, K. J. Kim, C. Kang, S. J. Oh, J. H. Son, K. H. An, D. J. Bae and Y. H. Lee, *Applied Physics Letters*, 2002, **80**, 3403-3405.
52. E. P. J. Parrott, J. A. Zeitler, J. McGregor, S.-P. Oei, H. E. Unalan, W. I. Milne, J.-P. Tessonnier, D. S. Su, R. Schloegl and L. F. Gladden, *Adv. Mater.*, 2009, **21**, 3953-+.
53. E. P. J. Parrott, J. A. Zeitler, J. McGregor, S. P. Oei, H. E. Unalan, S. C. Tan, W. I. Milne, J. P. Tessonnier, R. Schlogl and L. F. Gladden, *J. Phys. Chem. C*, 2009, **113**, 10554-10559.
54. A. Ugawa, A. G. Rinzler and D. B. Tanner, *Physical Review B*, 1999, **60**, R11305-R11308.

4.7 Supporting Information

Experimental Real and Imaginary Conductivity

The terahertz pulses transmitted through the samples and reference are shown in Figure S4-3a. The normalized spectra of the reference and signal pulses, obtained by fast Fourier transform, are shown in Figure S4-3b. The amplitude transmission and the corresponding phase change were determined by $|\tilde{t}(\omega)| = |E_s(\omega)/E_r(\omega)|$ and $\phi(\omega)=\arg[\tilde{t}(\omega)]$, respectively, with $E_s(\omega)$ and $E_r(\omega)$ being the Fourier-transformed amplitude spectra of the terahertz pulses transmitted through the sample and reference, respectively. When an electromagnetic wave propagates through a parallel slab, the transmission $\tilde{t}(\omega)$ can be described as

$$\tilde{t}(\omega) = \frac{t_{12}t_{21}\exp(ikL)\exp(-\alpha L/2)}{1+r_{12}r_{21}\exp(-\alpha L)\exp(i2kL)} \quad \text{(S4-1)}$$

where t_{12}, t_{21} and r_{12}, r_{21} are the frequency-dependent complex Fresnel transmission and reflection coefficients, respectively; α is the power absorption coefficient, k is the sample wave vector $k=2\pi n/\lambda_0$, and L is the sample thickness.[1-3] Through this relation, the power absorption coefficient and index of refraction can be retrieved, as shown in Figure S4-3c and d, respectively. Based on the frequency-dependent dielectric function

$$\varepsilon_{eff} = \varepsilon_{eff}^{\infty} + i\sigma/(\omega\varepsilon_0) = (n_r + in_i)^2 \quad \text{(S4-2)}$$

where $\varepsilon_{eff}^{\infty}$ is the dielectric constant of the films at infinity; σ is the frequency-dependent complex conductivity; ω is the frequency; ε_0 is the free-space permittivity; and n_r and $n_i = \alpha\lambda/4\pi$ are the real and imaginary index of refraction, respectively, the real and imaginary conductivity are determined.

References:

1. A. K. Azad, J. M. Dai, and W. Zhang, Opt. Lett. **31**, 634 (2006).
2. W. Zhang, Abul K. Azad and D. Grischkowsky, Appl. Phys. Lett. **82**, 2841 (2003).
3. M. Born and E. Wolf, *Principles of Optics* (Cambridge University Press, New York, 1999).

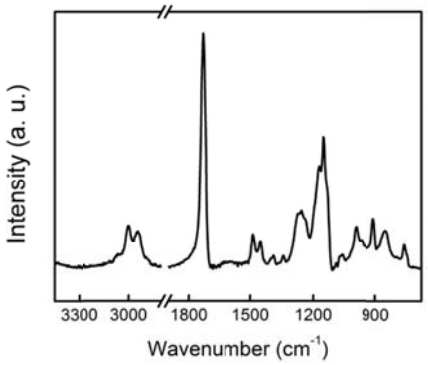

Figure S4-1 FTIR spectrum of the PGMA coating.

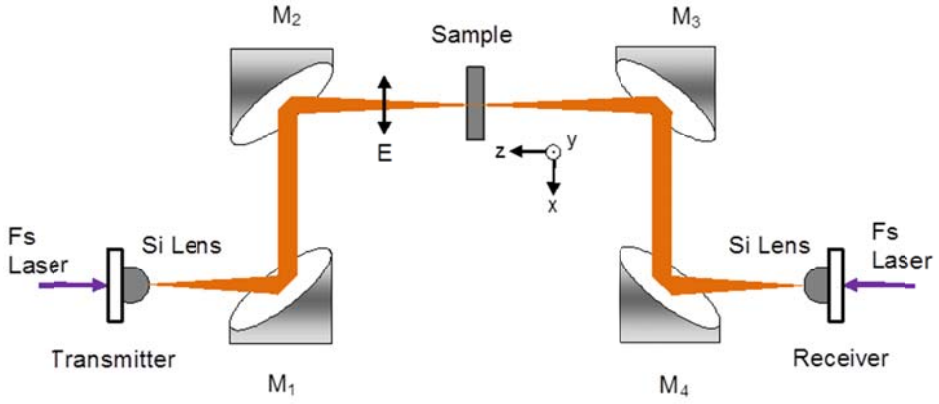

Figure S4-2 Experimental setup of the THz-TDS system.

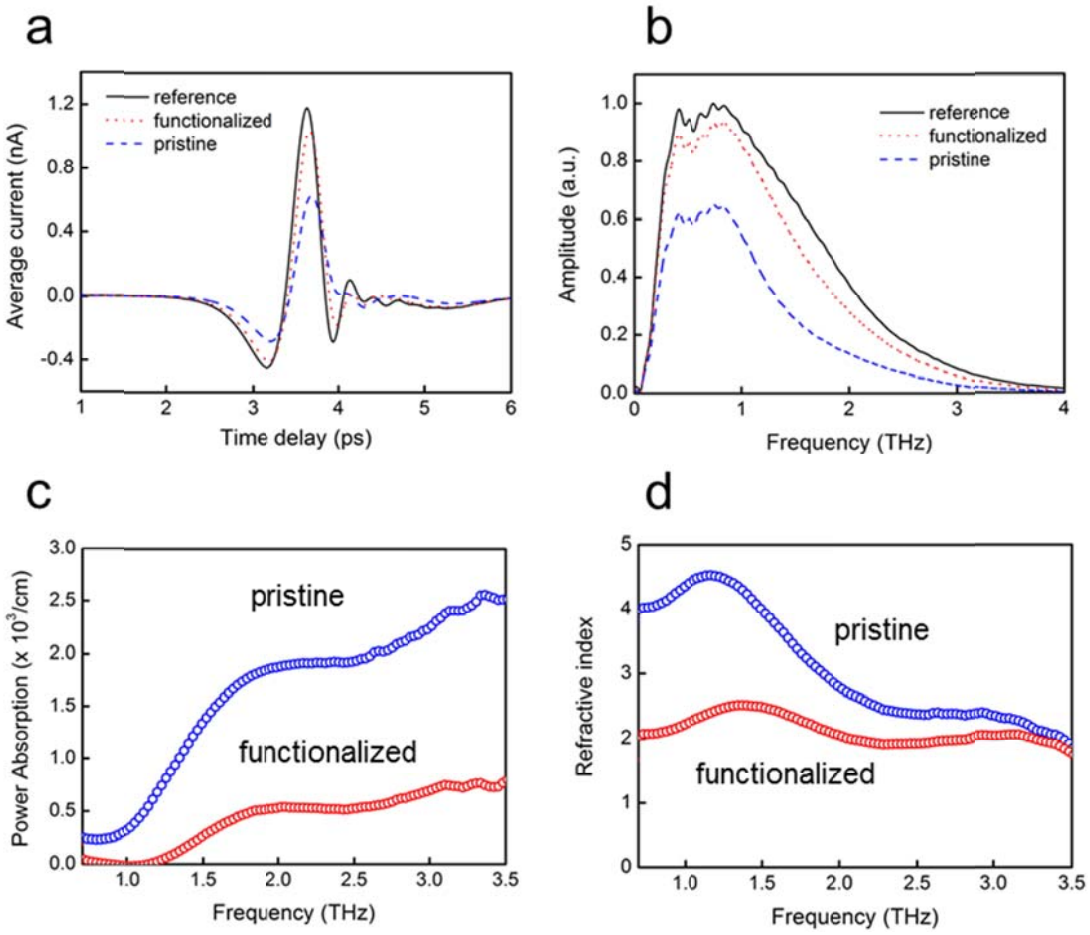

Figure S4-3 (a) Measured terahertz time-domain signals; (b) normalized spectra of the reference and sample signal pulses; (c) power absorption; and (d) refractive index.

Table S4-1 Theoretical fitting parameters for the measurements

parameters	$\omega_p/2\pi$ *(THz)*	$\Gamma/2\pi$ *(THz)*	$\omega_{pj}/2\pi$ *(THz)*	$\omega_j/2\pi$ *(THz)*	$\Gamma_j/2\pi$ *(THz)*	N	f
pristine	9.2	0.15	18.5	4.3	7.6	0.44	0.7
functionalized	8.3	0.4	18.9	3.9	15.6	0.5	0.9

CHAPTER V

HYBRID STRUCTURE OF PH-RESPONSIVE HYDROGEL AND CARBON NANOTUBE ARRAY WITH SUPERWETTABILITY

Y. M. Ye, Y. Mao, Zhifeng Ren, "Hybrid structure of pH-responsive hydrogel and carbon nanotube array with superwettability", *Journal of Materials Chemistry,* DOI: 10.1039/c1jm14547a.

Abstract

We report an all-dry fabrication method of the hybrid structure of pH-responsive hydrogel and carbon nanotube arrays using initiated chemical vapor deposition (iCVD). Vertically aligned carbon nanotube (VACNT) arrays with low site density were coated by vapor-deposited poly(methacrylic acid-*co*-ethylene glycol diacrylate) hydrogel with complete retention of the aligned structure and precise control of the coating thickness on each nanotube. The hydrogel coating imparted pH-responsiveness to the nanotube arrays and significantly enhanced the surface wettability. With an ultrathin 50-nm hydrogel coating, the hybrid hydrogel-VACNT array structure exhibited superwettability in neutral buffer solutions, which was attributed to the synergistic effect of the structure porosity and the ionization of the pH-responsive hydrogel. Under the acidic condition, the wettability depended on the coating thickness, and the apparent contact angle of the hybrid structure was in agreement with the calculated results from the Cassie-Baxter model.

5.1 Introduction

Vertically aligned carbon nanotube (VACNT) arrays offer an ideal platform for miniaturized device fabrication,[1-4] owing to the exceptional electrical and mechanical properties, as well as the ordered structure and easy integration into devices. VACNT arrays have shown great potential in enhancing the detection sensitivity of electrochemical sensors, as the aligned structure enables the fabrication of an electrode array consisting of millions of nanoelectrodes, resulting in significant amplification of electrical signals.[5-8] To enable each nanotube to function as an independent nanoelectrode, low-site-density VACNT arrays are preferred to avoid the overlapping of diffusion layers from each nanotube.[9,10] Generally low-site-density VACNT arrays refer to arrays with the nanotube interspace sufficiently larger than the nanotube radius.[9,11] It has been reported that the detection sensitivity of VACNT nanoelectrode arrays was dramatically improved by lowering the nanotube density.[12] On the other hand, high-site-density VACNT arrays usually perform as a macroelectrode with no nanoelectrode behavior.[9,10]

For sensing applications, surface functionalization of VACNT arrays is important, as it not only provides the functionality needed for analyte detection but also improves the biocompatibility and surface wettability, which play a vital role in applications both *in vitro* and *in vivo*.[13-15] Functionalization of VACNT arrays and the integration into devices have been extensively studied. The conventional approach involves dispersing randomly oriented carbon nanotubes, followed by functionalization in solution and alignment using external forces such as magnetic field[16,17] and mechanical shear.[18,19] However, the post-synthesis assembly strategy involves complex procedures and significant energy input, while the control of the nanotube alignment remains

challenging.[20-22] An alternative approach is to directly grow VACNT arrays using chemical vapor deposition followed by functionalization in solution using *in situ* polymerization[23,24] and polymer infiltration.[25,26] Compared with the post-synthesis assembly method, this approach offers improved alignment of nanotubes and thus the advantage for device fabrication. However, the solution-based functionalization requires the use of closely packed VACNT arrays to prevent the alignment collapse during the wetting and drying process.[27] Additionally, due to the limited control of coating thickness during the solution functionalization process, the resultant structure was usually in the form of nanotube-polymer composite with all the intertube space filled,[23,25,26] which resulted in significant diminishment of the accessible surface area and the sensing capability of the array structure.

Plasma vapor deposition has been explored as an approach to overcome the limitations in solution-based functionalization of VACNT arrays.[28-31] The solventless process prevents the disruption of the nanotube alignment and offers more control on the coating thickness, enabling retention of the original array structure. More importantly, the vapor-based functionalization can be applied on any VACNT array regardless of the nanotube site density. Plasma-deposited coatings with amino,[30] aldehyde,[28] and carboxyl[5] functionalities have been reported in the functionalization of VACNTs. However, the high energy input during the plasma process causes partial damage in the desired functional groups and generates unspecific groups in the resultant coatings.[32] To the best of our knowledge to date, functionalization of VACNTs by polymers with stoichiometric control, such as hydrogels, has not been reported using plasma vapor deposition.

Previously, we demonstrated the functionalization of high-site-density VACNT arrays with poly(glycidyl methacrylate) using initiated chemical vapor deposition (iCVD).[33] The iCVD method shares the advantages of vapor-based process with no plasma excitation needed. Instead, the process involves an initiation step in the heated vapor phase to generate radicals followed by adding monomers to the chain radicals to form polymer coatings on the un-heated substrate surface (Figure 5-1a).[34,35] The use of an initiator significantly lowers the energy input compared with conventional vapor deposition processes, which allows the preservation of a variety of delicate chemical functionalities.[36-40] Different from the non-selective chemistry in plasma vapor deposition, the controlled radical polymerization chemistry in iCVD allows both linear[36-38] and crosslinked polymers[41-43] with stoichiometric composition to be synthesized.

In this paper, we report one-step functionalization of low-site-density VACNT arrays with pH-responsive poly(methacrylic acid-*co*-ethylene glycol diacrylate) (P(MAA-*co*-EGDA)) hydrogel using iCVD (Figure 5-1). Poly(methacrylic acid) hydrogel has been employed in the fabrication of electrochemical sensors.[44,45] In addition, the hydrogel allows wettability improvement and further derivation for molecular immobilization.[45] We used P(MAA-*co*-EGDA) hydrogel to demonstrate the iCVD functionalization of VACNT arrays with the retention of nanotube alignment, control of coating thickness, and stoichiometric control of the hydrogel composition. The hydrogel imparted pH-responsive property to the nanotube arrays and significantly enhanced the surface wettability. With an ultrathin 50-nm hydrogel coating, the hybrid hydrogel-VACNT array structure exhibited superwettability in neutral buffer solutions. Analysis on the

wettability of the hydrogel-VACNT array using the Cassie-Baxter model will be presented.

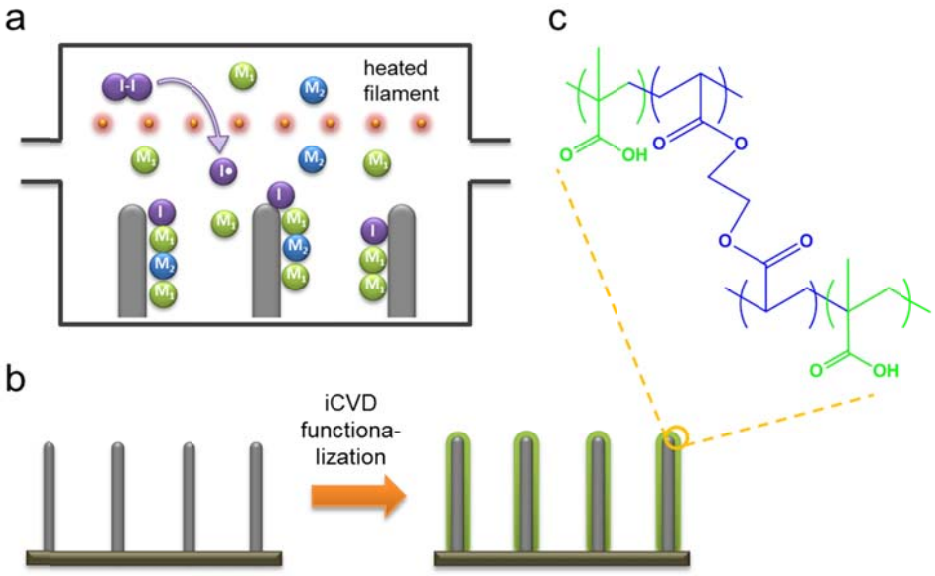

Figure 5-1 a) The controlled radical polymerization during iCVD. I-I, I•, M_1, and M_2 stand for *tert*-butyl peroxide initiator, *tert*-butoxy radical, methacrylic acid, and ethylene glycol diacrylate, respectively; b) iCVD functionalization of the VACNT array with hydrogel; c) chemical structure of the P(MAA-*co*-EGDA) hydrogel.

5.2 Experimental

5.2.1 Growth of low site density VACNT arrays

VACNTs were prepared following the procedures previously reported.[46] Briefly, nickel (Ni) catalyst was deposited by electron beam evaporation on chromium coated glass substrates of 10 mm X 10 mm with the self-assembled polystyrene microspheres as a mask. The polystyrene microspheres were subsequently removed by sonication to reveal the periodically patterned Ni dots. The substrates were then placed in a plasma enhanced chemical vapor deposition system with the stage heated to 450-600 °C. After

the Ni dots were annealed for 2 min, growth of VACNTs was triggered by supplying NH_3 at 160 sccm and C_2H_2 at 60 sccm in the presence of plasma. The length of VACNTs was determined by the growth time.

5.2.2 Vapor deposition of hydrogel

The vapor-based functionalization of VACNT arrays was performed in a custom-built iCVD reactor (Sharon Vacuum) as previously described.[33,42,47] Methacrylic acid (MAA) and ethylene glycol diacrylate (EGDA) were used as the precursor monomers and *tert*-butyl peroxide (TBP) was used as the initiator. TBP, MAA, and EGDA were heated to 25 °C, 50 °C and 60 °C, and the vapors were fed into the reactor at the flow rates of 0.4, 0.8, and 0.2 sccm, respectively. The flow rate was controlled using two mass flow controllers (MKS, Type 1150 and Type 1479A) and a manual needle valve. TBP was thermally decomposed at the vicinity of a Nichrome filament (Ni80/Cr20, Goodfellow), which was mounted in parallel arrays at 2.5 cm above the stage and resistively heated to 190 °C. The thermally generated radicals initiated the copolymerization of MAA and EGDA, which formed the copolymer coatings on the VACNT arrays. The substrate temperature was maintained at 30 °C, as measured by directly attached thermal couples (Omega, Type K). The pressure in the reactor was maintained at 250 mTorr using a throttling butterfly valve (MKS, Type 253B). The deposition process was monitored using an interferometer by measuring the real-time growth of the coating on a reference silicon wafer placed close to the VACNT arrays. P(MAA-*co*-EGDA) coatings with two different thicknesses were synthesized by controlling the deposition time at 5 and 15 min. As a comparison, homopolymer coatings of poly(methacrylic acid) (PMAA) and

poly(ethylene glycol diacrylate) (PEGDA) were deposited using the corresponding monomer under the same processing condition as that of the P(MAA-*co*-EGDA) coating.

5.2.3 Characterizations

The morphology of the VACNT arrays was observed using an FEI Quanta 600F scanning electron microscope (SEM). The FTIR spectra of the iCVD coatings were collected by a Nicolet 6700 FTIR spectrometer under the transmission mode using a DTGS detector over the range of 400-4000 cm^{-1} at 4 cm^{-1} resolution.

The thickness of the hydrogel coatings on planar silicon wafer before (t_{dry}) and after immersing (t_{wet}) in phosphate buffer solutions (PBS) was measured using a Veeco Multimode SPM atomic force microscope (AFM) under the tapping mode. A Z-shaped scratch penetrating the soft hydrogel coating was made prior to the measurement. The thickness of the coating was obtained by analyzing the depth profile of the scratch. The swelling ratio (*SR*) of the hydrogel coating was determined using $SR=(t_{wet}-t_{dry})*100\%/t_{dry}$. The surface topography of the coated VACNT arrays was measured using the same AFM under the tapping mode.

The contact angle measurement was conducted at 23 °C under a relative humidity of approximately 50% using a standard contact angle goniometer (Rame Hart, Model 250-F1) equipped with an automatic liquid dispensing system. For each measurement, a droplet of 2 μL was placed on top of the VACNT surface, and the static contact angle was measured using images taken by the camera and analyzed by the DROPimage software. Multiple measurements were taken on each sample, and the deviations are within 2° for flat hydrogel surfaces and 3° for hydrogel coated nanotube arrays.

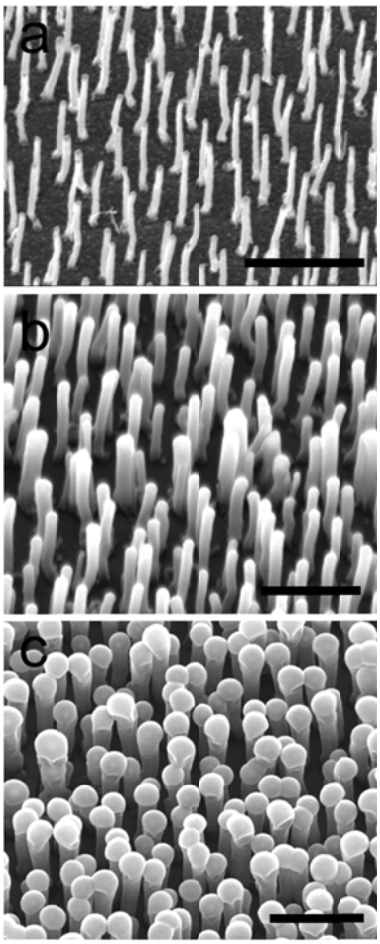

Figure 5-2 SEM images of pristine VACNT arrays (a), hydrogel coated VACNT arrays with coating thicknesses of 50 nm (b) and 140 nm (c). The scale bar is 2 μm.

5.3 Results and Discussion

5.3.1 Functionalization of VACNT arrays

Figure 5-2 shows the VACNT arrays before and after the iCVD functionalization of P(MAA-*co*-EGDA) hydrogel. The pristine carbon nanotubes are estimated to have an average diameter of 100 nm and length of 2 μm, with an average distance of 500 nm between adjacent nanotubes. The VACNT arrays were coated with 50 nm (Figure 5-2b)

and 140 nm (Figure 5-2c) hydrogels on the nanotube sidewalls by controlling the iCVD deposition time. The aligned morphology was completely preserved. The hydrogel coating was uniform in the 50-nm coated VACNTs, while accumulation of the coating was observed at the top of the 140-nm coated VACNTs, possibly due to the difference in the mass transport of vapor reactants as the coating deposition time increased. The capability to functionalize VACNT arrays in a controlled manner while maintaining the aligned morphology is important for the successful fabrication of sensing devices.[48-50] Compared with the solution-based functionalization methods used in device fabrications, which only allowed the nanotube tips to be derivatized because of the encapsulation of VACNT arrays inside a supportive matrix,[51,52] the vapor-based process enabled functionalization of both nanotube tips and sidewalls, providing high surface area for sensing.

The iCVD P(MAA-*co*-EGDA) coating was characterized using FTIR and compared with iCVD poly(methacrylic acid) (PMAA) and poly(ethylene glycol diacrylate) (PEGDA) coatings, as shown in Figure 5-3a. No trace of vinyl moiety around 985, 1410 or 1640 cm^{-1} was observed in any of the spectrum, indicating a complete conversion of monomer vapors to polymer coatings. The broad absorption at 2500-3500 cm^{-1} and the absorption centered at 1700 cm^{-1} are assigned to the –OH and C=O stretching of the PMAA coating, respectively, while the strong absorption at 1735 cm^{-1} is assigned to the C=O stretching of the PEGDA coating. The spectrum of the P(MAA-*co*-EGDA) hydrogel shows characteristic peaks from both PMAA and PEGDA, with a reduced intensity in the –OH absorption region. The enlarged C=O stretching of the three coatings (Figure 5-3b) clearly shows that the carbonyl peak of the P(MAA-*co*-EGDA)

coating is comprised of two peaks at 1700 and 1735 cm^{-1}, which are stemmed from the C=O stretching in PMAA and PEGDA, respectively. After decoupling the C=O absorption peak of the P(MAA-*co*-EGDA) copolymer using the Omnic software and comparing with the C=O peaks in homopolymer PMAA and PEGDA, the composition of the P(MAA-*co*-EGDA) hydrogel was quantified using procedures previously reported.[37,42] The molar ratio of MAA/EGDA in the P(MAA-*co*-EGDA) hydrogel coating was calculated to be 1.00 ±0.05.

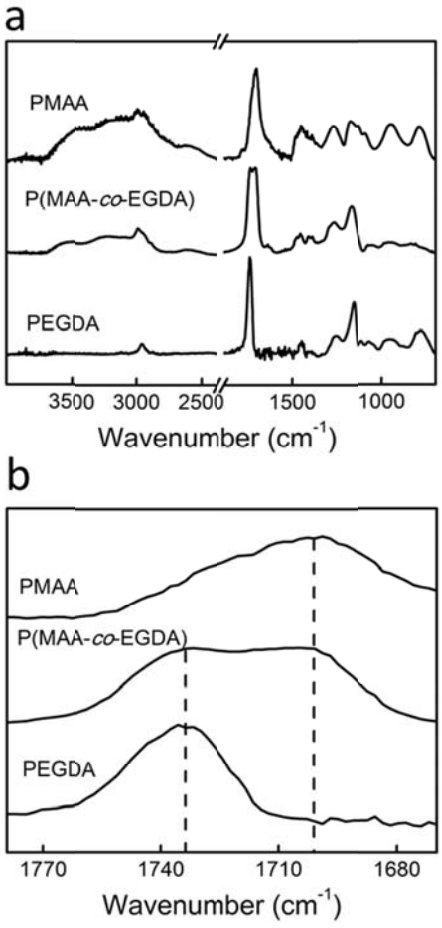

Figure 5-3 FTIR spectra of a) the iCVD PMAA, P(MAA-*co*-EGDA), and PEGDA coatings; b) the enlarged C=O stretching region.

5.3.2 pH-responsive swelling

The pH-responsive swelling of the P(MAA-*co*-EGDA) coating was examined both quantitatively on planar surfaces and qualitatively on VACNT arrays. Quantitative measurement of the swelling ratio was performed by measuring the thickness change of the coating after immersing in buffer solutions with different pH values. As shown in Figure 5-4, the hydrogel did not swell appreciably when immersed in acidic solutions. At pH 7, a swelling ratio of 38%, defined as the thickness increase relative to the dry thickness, was observed, indicating the ionization of carboxyl groups in the P(MAA-*co*-EGDA) hydrogel.[53] The swelling ratio of the P(MAA-*co*-EGDA) hydrogel coating was close to that of the reported poly(methacrylic acid-*co*-ethylene glycol dimethacrylate) hydrogel with a MAA molar composition of 0.52.[41]

Surface topography of the hydrogel coated VACNT arrays at different pH was investigated using AFM. Figure 5-5 shows the 140 nm-coated VACNT arrays in the dry, wet, and swollen states. At dry state, the coated VACNT arrays showed features like what was observed under SEM. At pH 2, the swelling of the hydrogel coating was not significant, and the morphology of the coated VACNTs resembled that of the dry state. At pH 7, the hydrogel swelling was evident, and the coated nanotube arrays showed a smoother surface due to the expansion of the hydrogel, similar to what was observed in the wetting of PNIPAAm infiltrated VACNTs.[23] The slightly higher surface roughness of the P(MAA-*co*-EGDA) coated VACNTs at the swollen state is possibly due to the lower site-density of nanotubes and the less swelling of the hydrogel compared with the counterparts in the PNIPAAm infiltrated VACNTs.

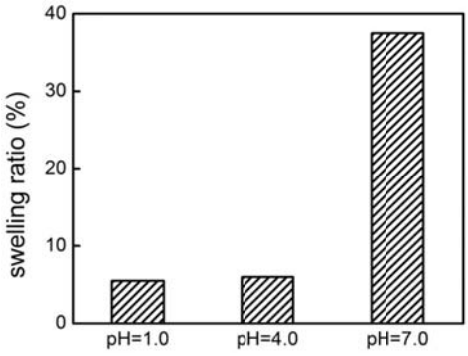

Figure 5-4 The swelling ratio of the P(MAA-*co*-EGDA) hydrogel coatings at different pH.

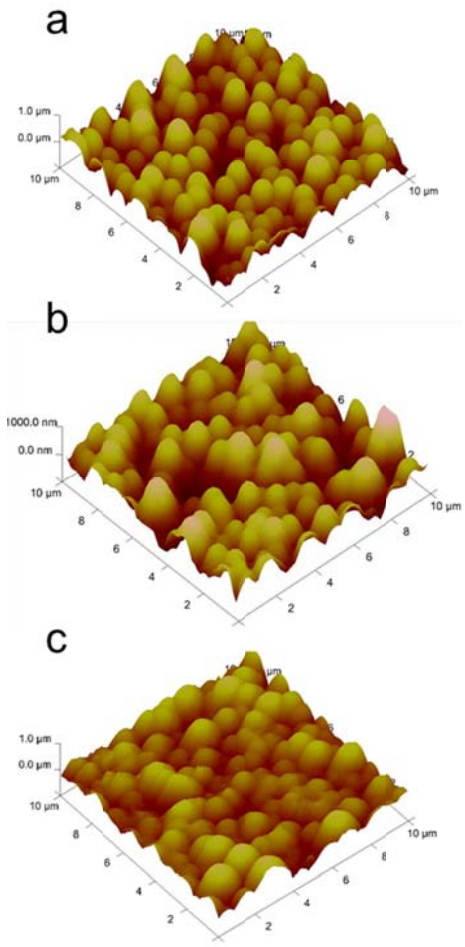

Figure 5-5 AFM surface topography of the 140 nm-coated VACNT arrays at dry state (a), and immersed in pH 2 (b) and pH 7 (c) solutions.

5.3.3 Surface wettability

The wettability of the pristine and coated VACNTs was compared by first measuring the sessile drop contact angle (CA) at pH 2 (Figure 5-6). The pristine VACNT film is hydrophobic with a CA of 112°. Given the fact that the graphitic surface has a CA of 84-86°,[54] the hydrophobicity of the pristine VACNTs is mainly attributed to the surface topography of the aligned nanotubes.[13] The P(MAA-*co*-EGDA) hydrogel imparted significant wettability to the VACNT arrays, resulting in dramatic decreases of the CA to 18° and 24° for the 50-nm and 140-nm coated nanotubes, respectively. It is noted that the hydrogel coated VACNTs were more readily wetted than the corresponding hydrogel, which has a CA of 58° at pH 2. As to be discussed below, both the hydrogel coating and the porous VACNT structure contributed to the enhanced wettability of coated VACNTs.

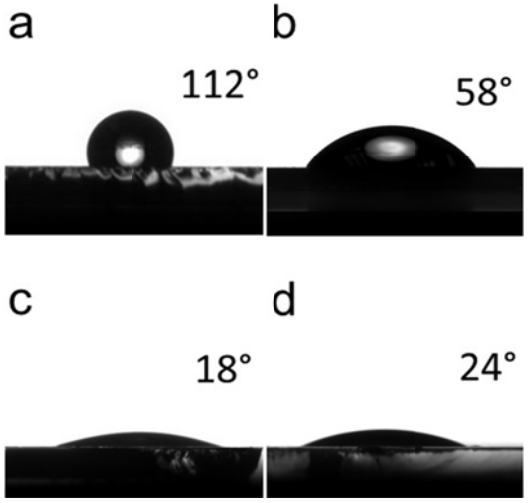

Figure 5-6 Contact angle of a pH 2 solution on pristine VACNTs (a), P(MAA-*co*-EGDA) hydrogel (b) , and hydrogel coated VACNTs with coating thicknesses of 50 nm (c) and 140 nm (d).

According to the Cassie-Baxter model,[55,56] the apparent CA of a porous surface can be derived from the cosine of each surface component's CA. When a liquid droplet sits on the surface of VACNT films, the pores between nanotubes can be 1) wetted and filled with the liquid or 2) non-wetted with the air trapped inside the pockets, depending on the surface wettability of the nanotube.[57,58] The criterion for the wetting transition can be assessed using the critical imbibition angle (θ_c)[56,59]:

$$\theta_c = \frac{1-f}{r-f} \tag{5-1}$$

where f is the area fraction of the nanotube top surface and can be calculated from SEM observations, and r is the roughness factor defined as the ratio of actual to projected surface area.

The critical imbibition angle for the pristine VACNT surface is calculated to be 60.5°, which is lower than the CA of the graphitic surface (84-86°),[49] suggesting that the liquid bridges over the pores between nanotubes with low tendency to spread (Figure 5-7a). On the other hand, θ_c for the hydrogel coated VACNTs is calculated to be in the range of 73-84°, depending on the coating thickness. Since the hydrogel is hydrophilic with a lower CA of 58°, the liquid is predicted to invade into the interspace between the hydrogel-sheathed nanotubes (Figure 5-7b). In this imbibition regime, the CA of the liquid becomes 0° for the droplets of the same liquid, and the theoretical apparent CA (θ) of the hybrid structure can be calculated using the following equation:[56,60,61]

$$\cos\theta = f\cos\theta_s + (1-f) \tag{5-2}$$

where θ_s is the CA of the hydrogel on a planar surface.[62] According to this equation, the apparent CA at pH 2 was calculated to be 20° and 30° for the 50-nm and 140-nm coated VACNTs, respectively. As shown in Table 5-1, the calculated CAs were close to the measured results at pH 2. The coated VACNTs with a thinner hydrogel layer of 50 nm showed better wettability than the VACNTs with a coating of 140 nm, because of the smaller area fraction of the solid surface *f*.

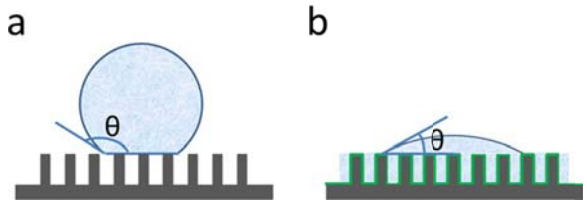

Figure 5-7 Porous VACNT structure with liquid non-imbibed (a) and imbibed (b), depending on the wettability of the nanotubes.

We further studied the wetting behavior of the coated VACNTs under the neutral condition. At pH 7, the CA of the pristine VACNTs remains at 112°, while the hydrogel coated VACNTs showed significant increase in the wettability. The droplet spread rapidly upon contact with the surface of the 50 nm-coated VACNTs, and the CA reached 0° in 2 s, resulting in a "superwettable" surface (Figure 5-8). Similarly, the CA of the 140 nm-coated VACNTs decreased to 7°.

To understand the superwettability at pH 7, we tested the CA of the flat hydrogel surface and observed a CA of 46°. The increase in the hydrogel hydrophilicity was attributed to the ionization of the carboxyl groups at neutral conditions.[63] Under the assumption that the hydrogel swells to the same extent on the nanotube sidewalls as on

the planar surface, the nanotube area fraction f at the swollen state can be calculated. Using equation (5-2), the theoretical CAs of the hydrogel coated VACNTs at pH 7 were calculated to be 14° and 28° for the 50-nm and 140-nm coated VACNTs, respectively. The deviation of the measured CAs from the calculated values suggests that the hydrogel surface property and the porous structure of the hydrogel coated VACNTs synergistically contribute to the enhanced wettability. At pH 7, the ionization of the carboxyl groups increased the hydrophilicity of each hydrogel-coated nanotube and facilitated the invasion of the liquid into the intertube space, which was reflected in the experimental observation that the buffer droplets were quickly absorbed within the porous structure. The swelling of the hydrogel is expected to further enhance the impregnation process by absorbing part of the liquid, resulting in more liquid invasion into the porous hydrogel-VACNT structure and thereby the surface superwettability. Theoretically, equation (5-2) predicts that superwettability cannot be obtained unless θ_s is close to zero. Our work demonstrated that superwettability can be achieved through the synergistic effect of porosity control and coating chemistry.[56,61]

Table 5-1 Measured (θ_{mea}) and calculated (θ_{cal}) contact angle of the hydrogel-coated VACNTs at different pH.

coating thickness	pH 2		pH 7	
	θ_{mea}	θ_{cal}	θ_{mea}	θ_{cal}
50 nm	18°	20°	0°	14°
140 nm	24°	30°	7°	28°

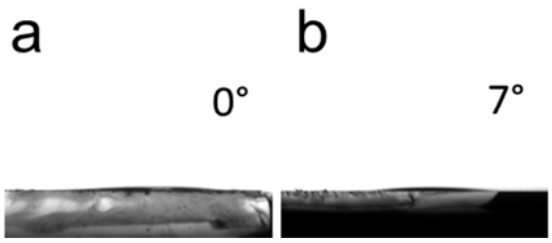

Figure 5-8 Contact angle of hydrogel-coated VACNTs with coating thicknesses of a) 50 nm and b) 140 nm at pH 7.

5.4 Conclusions

Hybrid structure of aligned carbon nanotubes and a pH-responsive hydrogel was fabricated by iCVD deposition of P(MAA-*co*-EGDA) hydrogel directly on carbon nanotube arrays with low site density from monomer vapors. The iCVD process allowed preservation of the monomer functionality, retention of the nanotube alignment, and control of the coating thickness at the sub-100 nm level. The P(MAA-*co*-EGDA) hydrogel demonstrated pH-responsive swelling on both planar surfaces and carbon nanotube arrays. The hydrogel coating significantly enhanced the wettability of the VACNT surface. The wettability of the coated VACNTs depended on both the coating thickness and the pH condition. At pH 2, the wettability of the coated VACNTs with different coating thickness was in agreement with the calculated results of the Cassie-Baxter model. Under the neutral pH condition, the coated VACNT surface exhibited an apparent contact angle of nearly zero. The superwettability was attributed to the synergistic effect of the structure porosity and the ionization of the pH-responsive hydrogel.

5.5 Acknowledgement

We are grateful for the support from the CAREER Award of National Science Foundation (CMMI 1056074). We also thank the Oklahoma State University Microscopy Laboratory for the SEM and AFM experiments. The work performed at Boston College is funded by US Department of Energy under contract number DOE DE-FG02-00ER45805 (ZFR).

5.6 References

1. Z. F. Ren, Z. P. Huang, J. W. Xu, J. H. Wang, P. Bush, M. P. Siegal and P. N. Provencio, *Science*, 1998, **282**, 1105-1107.
2. A. Bachtold, P. Hadley, T. Nakanishi and C. Dekker, *Science*, 2001, **294**, 1317-1320.
3. S. Ghosh, A. K. Sood and N. Kumar, *Science*, 2003, **299**, 1042-1044.
4. B. J. Hinds, N. Chopra, T. Rantell, R. Andrews, V. Gavalas and L. G. Bachas, *Science*, 2004, **303**, 62-65.
5. P. G. He and L. M. Dai, *Chem. Commun.*, 2004, 348-349.
6. G. D. Withey, A. D. Lazareck, M. B. Tzolov, A. Yin, P. Aich, J. I. Yeh and J. M. Xu, *Biosens. Bioelectron.*, 2006, **21**, 1560-1565.
7. S. Sotiropoulou, Chaniotakis, N. , *Anal. Bioanal. Chem.*, 2003, **315**, 103-105.
8. D. Cai, L. Ren, H. Zhao, C. Xu, L. Zhang, Y. Yu, H. Wang, Y. Lan, M. F. Roberts, J. H. Chuang, M. J. Naughton, Z. Ren and T. C. Chiles, *Nat. Nanotechnol.*, 2010, **5**, 597-601.
9. Y. Tu, Y. H. Lin and Z. F. Ren, *Nano Lett.*, 2003, **3**, 107-109.
10. W. E. Morf and N. F. de Rooij, *Sens. Actuat. B-Chem.*, 1997, **44**, 538-541.
11. Y. Tu, Y. H. Lin, W. Yantasee and Z. F. Ren, *Electroanalysis*, 2005, **17**, 79-84.
12. J. Li, H. T. Ng, A. Cassell, W. Fan, H. Chen, Q. Ye, J. Koehne, J. Han and M. Meyyappan, *Nano Lett.*, 2003, **3**, 597-602.
13. H. Liu, J. Zhai and L. Jiang, *Soft Matter*, 2006, **2**, 811-821.
14. M. Foldvari and M. Bagonluri, *Nanomed. Nanotechnol. Biol. Med.*, 2008, **4**, 183-200.
15. N. Saito, Y. Usui, K. Aoki, N. Narita, M. Shimizu, K. Hara, N. Ogiwara, K. Nakamura, N. Ishigaki, H. Kato, S. Taruta and M. Endo, *Chem. Soc. Rev.*, 2009, **38**, 1897-1903.
16. T. Kimura, H. Ago, M. Tobita, S. Ohshima, M. Kyotani and M. Yumura, *Adv. Mater.*, 2002, **14**, 1380-1383.
17. K. Kordas, T. Mustonen, G. Toth, J. Vahakangas, A. Uusimaki, H. Jantunen, A. Gupta, K. V. Rao, R. Vajtai and P. M. Ajayan, *Chem. Mater.*, 2007, **19**, 787-791.
18. C. Zamora-Ledezma, C. Blanc, M. Maugey, C. Zakri, P. Poulin and E. Anglaret, *Nano Lett.*, 2008, **8**, 4103-4107.
19. L. H. Lu and W. Chen, *Acs Nano*, 2010, **4**, 1042-1048.
20. P. M. Ajayan and J. M. Tour, *Nature*, 2007, **447**, 1066-1068.
21. L. Li, Z. B. Yang, H. J. Gao, H. Zhang, J. Ren, X. M. Sun, T. Chen, H. C. Kia and H. S. Peng, *Adv. Mater.*, 2011, **23**, 3730-3735.
22. Y. F. Ma, B. Wang, Y. P. Wu, Y. Huang and Y. S. Chen, *Carbon*, 2011, **49**, 4098-4110.
23. W. Chen, L. Qu, D. Chang, L. Dai, S. Ganguli and A. Roy, *Chem. Commun.*, 2008, 163-165.
24. Z. H. Yang, Z. Cao, H. Sun and Y. Li, *Adv. Mater.*, 2008, **20**, 2201-2205.
25. C. Wei, L. M. Dai, A. Roy and T. B. Tolle, *J. Am. Chem. Soc.*, 2006, **128**, 1412-1413.
26. N. R. Raravikar, L. S. Schadler, A. Vijayaraghavan, Y. P. Zhao, B. Q. Wei and P. M. Ajayan, *Chem. Mater.*, 2005, **17**, 974-983.
27. C. V. Nguyen, L. Delzeit, A. M. Cassell, J. Li, J. Han and M. Meyyappan, *Nano Lett.*, 2002, **2**, 1079-1081.
28. Q. D. Chen, L. M. Dai, M. Gao, S. M. Huang and A. Mau, *J. Phys. Chem. B*, 2001, **105**, 618-622.
29. H. Chen, A. Roy, J. B. Baek, L. Zhu, J. Qu and L. M. Dai, *Mater. Sci. Eng., R*, 2010, **70**, 63-91.
30. E. Luais, C. Thobie-Gautier, A. Tailleur, M. A. Djouadi, A. Granier, P. Y. Tessier, D. Debarnot, F. Poncin-Epaillard and M. Boujtita, *Electrochim. Acta*, 2010, **55**, 7916-7922.
31. W. Lin, Y. H. Xiu, H. J. Jiang, R. W. Zhang, O. Hildreth, K. S. Moon and C. P. Wong, *J. Am. Chem. Soc.*, 2008, **130**, 9636-9637.

32. H. O. Pierson, *Handbook of chemical vapor depostion: principles, technology and applications*, Noyes Publications, Norwich, 1999.
33. Y. M. Ye, Y. Mao, F. Wang, H. B. Lu, L. T. Qu and L. M. Dai, *J. Mater. Chem.*, 2011, **21**, 837-842.
34. S. H. Baxamusa, S. G. Im and K. K. Gleason, *PCCP*, 2009, **11**, 5227-5240.
35. W. E. Tenhaeff and K. K. Gleason, *Adv. Funct. Mater.*, 2008, **18**, 979-992.
36. Y. Mao and K. K. Gleason, *Langmuir*, 2004, **20**, 2484-2488.
37. K. Chan and K. K. Gleason, *Langmuir*, 2005, **21**, 8930-8939.
38. M. Gupta and K. K. Gleason, *Langmuir*, 2006, **22**, 10047-10052.
39. T. P. Martin, S. E. Kooi, S. H. Chang, K. L. Sedransk and K. K. Gleason, *Biomaterials*, 2007, **28**, 909-915.
40. Y. Mao and K. K. Gleason, *Macromolecules*, 2006, **39**, 3895-3900.
41. K. K. S. Lau and K. K. Gleason, *Macromol. Biosci.*, 2007, **7**, 429-434.
42. Y. M. Ye, Q. Song and Y. Mao, *J. Mater. Chem.*, 2011, **21**, 257-262.
43. Y. M. Ye and Y. Mao, *J. Mater. Chem.*, 2011, **21**, 7946-7952.
44. R. Thoelen, R. Vansweevelt, J. Duchateau, F. Horemans, J. D'Haen, L. Lutsen, D. Vanderzande, M. Ameloot, M. VandeVen, T. J. Cleij and P. Wagner, *Biosens. Bioelectron.*, 2008, **23**, 913-918.
45. P.-Y. Chen, P.-C. Nien, C.-W. Hu and K.-C. Ho, *Sens. Actuat. B-Chem.*, 2010, **146**, 466-471.
46. Y. Wang, J. Rybczynski, D. Z. Wang, K. Kempa, Z. F. Ren, W. Z. Li and B. Kimball, *Appl. Phys. Lett.*, 2004, **85**, 4741-4743.
47. Y. Ye and Y. Mao, *J. Mater. Chem.*, 2011, **21**, 7946-7952.
48. L. M. Dai, A. Patil, X. Y. Gong, Z. X. Guo, L. Q. Liu, Y. Liu and D. B. Zhu, *Chemphyschem*, 2003, **4**, 1150-1169.
49. D. Vairavapandian, P. Vichchulada and M. D. Lay, *Anal. Chim. Acta*, 2008, **626**, 119-129.
50. J. Wang, *Electroanalysis*, 2005, **17**, 7-14.
51. J. E. Koehne, H. Chen, A. M. Cassell, Q. Yi, J. Han, M. Meyyappan and J. Li, *Clin. Chem.*, 2004, **50**, 1886-1893.
52. Y. H. Lin, F. Lu, Y. Tu and Z. F. Ren, *Nano Lett.*, 2004, **4**, 191-195.
53. V. A. Izumrudov, E. Kharlampieva and S. A. Sukhishvili, *Biomacromolecules*, 2005, **6**, 1782-1788.
54. F. M. Fowkes and W. D. Harkins, *J. Am. Chem. Soc.*, 1940, **62**, 3377-3386.
55. A. B. D. Cassie and S. Baxter, *Trans. Faraday Soc.*, 1944, **40**, 0546-0550.
56. D. Quere, *Physica A*, 2002, **313**, 32-46.
57. F. Xie, P. Weiss, O. Chauvet, J. Le Bideau and J. F. Tassin, *J. Mater. Sci. - Mater. Med.*, 2010, **21**, 1163-1168.
58. N. Havens, P. Trihn, D. Kim, M. Luna, A. K. Wanekaya and A. Mugweru, *Electrochim. Acta*, 2010, **55**, 2186-2190.
59. J. Bico, C. Tordeux and D. Quere, *Europhys. Lett.*, 2001, **55**, 214-220.
60. J. Bico, U. Thiele and D. Quere, *Colloids Surf., A*, 2002, **206**, 41-46.
61. J. Drelich and E. Chibowski, *Langmuir*, 2010, **26**, 18621-18623.
62. N. J. Shirtcliffe, G. McHale, M. I. Newton, C. C. Perry and P. Roach, *Chem. Commun.*, 2005, 3135-3137.
63. A. J. Parnell, S. J. Martin, C. C. Dang, M. Geoghegan, R. A. L. Jones, C. J. Crook, J. R. Howse and A. J. Ryan, *Polymer*, 2009, **50**, 1005-1014.

CHAPTER VI

VAPOR-BASED SYNTHESIS OF ULTRATHIN HYDROGEL COATINGS FOR THERMO-RESPONSIVE NANOVALVES

Y. M. Ye, Y. Mao, "Vapor-based synthesis of ultrathin hydrogel coatings for thermo-responsive nanovalves", *Journal of Materials Chemistry,* 2011, 21, 7946-7952.

Abstract

We report vapor-based, single-step synthesis of hydrogel coatings and the fabrication of thermo-responsive nanovalves with fine flow regulation. The hydrogel films exhibited swelling ratios as high as 15.4 at room temperature. The swelling ratio dramatically decreased with the increase of the temperature. The increase of the crosslinking degree in the hydrogel reduced the swelling ratio of the coatings and broadened the transition temperature region. Thermo-responsive nanovalves were fabricated by depositing ultrathin hydrogel coatings inside nanoporous track-etched polycarbonate membranes. Electron microscopy observations revealed hydrogel coatings along the sidewalls of the nanopores with controllable thicknesses in the sub-50 nm range. The "closed" and "open" states of the nanopores for the flow of bovine serum albumin were achieved by varying the temperature. Fine regulation of the protein flow was also demonstrated in nanopores with different hydrogel coating thickness. The hydrogel coatings were estimated to have smaller temperature-induced swelling change in the nanopores compared with the same coatings on planar surfaces.

6.1 Introduction

Stimuli-responsive polymers are promising candidates for building smart devices, as they sensitively respond to environmental alterations such as temperature, pH, and ion concentrations by changing a variety of properties, including volume, surface hydrophilicity, and permeability.[1-5] These responsive behaviors can be exploited for applications in tunable transportation of molecules,[6,7] sensors and actuators,[8-10] and controlled release.[11] Among the various responsive polymers, thermo-responsive hydrogel is of particular interest in biological applications, since temperature can be conveniently controlled to trigger the response using direct heating/cooling or remotely controlled stimuli such as magnetic fields or near-infrared irradiation.[12-14] Furthermore, the biocompatibility of the hydrogel offers another advantage for applications in biological entities.

Smart membranes that respond to external stimuli in controlled ways have been developed by incorporating stimuli-responsive polymers.[15-17] Thermo-responsive membranes have gathered considerable attention because of their potential applications in drug delivery.[13,16,18] The design of thermo-responsive membranes usually falls into two categories: direct membrane fabrication using thermo-responsive polymers[19-21] and modification of existing membranes with the responsive polymers.[22-25] The direct fabrication method involves synthesis of thermo-responsive copolymers followed by polymer processing such as solvent casting[24,26] and phase separation.[20,27] In order to obtain good mechanical strength of the membranes, a non-responsive polymer needs to be incorporated as the major component. For example, thermo- and pH- dual responsive porous membranes were fabricated using block copolymers of polystyrene and poly(N,N-

dimethylaminoethyl methacrylate) with 81 wt% of polystyrene.[20] By combining the variation of both temperature and pH, a 7-fold change in the water flux through the membrane was achieved.

Another method of fabricating thermo-responsive membranes is to graft responsive polymers onto existing porous membranes with the desired mechanical robustness. Poly(N-isopropylacrylamide) (PNIPAm) and its copolymers with a range of response temperatures were grafted onto polyvinylidene fluoride and nylon membranes by pretreating membranes with plasma followed by the grafting reaction. Water flux through the membrane exhibited discontinuous change at the phase transition temperature of the gating polymers, indicating the thermo-response of the membranes.[23] In another study, poly(ethylene terephthalate) microfiltration membranes were photografted with PNIPAm.[28] If the grafting density is high enough, the membrane surface can be completely and partially covered with PNIPAm at the swollen and collapsed state, respectively, resulting in the thermo-responsive permeation of bovine serum album (BSA) through the pores. However, the precise control of grafting density and thickness is hard to achieve using the grafting-based membrane modification.[7]

Vapor-based polymer coating represents an alternative approach for surface modification.[29] It is a solventless, one-step process that does not require any surface pretreatment. Thermo-responsive PNIPAm films have been deposited by plasma polymerization with swelling behavior and surface properties studied.[30-32] Thermal responsiveness of the plasma PNIPAm films was demonstrated; however, the hydrogel swelling was only quantitatively measured using moisture sorption experiments. To the

best of our knowledge, fabrication of thermo-responsive nanoporous membranes using vapor-based polymer coating has not been reported.

Herein we report one-step vapor deposition of poly(N,N-dimethylaminoethyl methacrylate-*co*-ethylene glycol diacrylate) (P(DMAEMA-*co*-EGDA)) hydrogel coatings and the fabrication of thermo-responsive hydrogel nanovalves. The vapor deposition process exploits the thermal decomposition of initiator *tert*-butyl peroxide (TBP) [33, 34] to copolymerize DMAEMA and EGDA vapors,[33,34] resulting in direct deposition of hydrogel coatings on both planar surfaces and nanoporous polycarbonate membranes. We investigate the thermo-responsive swelling of the synthesized hydrogel films with different crosslinking densities. We demonstrate the switch between the "open" and "closed" states of the nanopores and fine flow regulation enabled by the thermo-induced phase transition of hydrogel coatings at different thickness inside the nanopores. The disparity between the hydrogel swelling in confined nanopores and that on planar surfaces will also be discussed.

6.2 Experimental

6.2.1 Materials

DMAEMA (98%), EGDA (90%), and TBP (98%) were all purchased from Sigma-Aldrich and directly used without further purification. Silicon wafers (MEMC Electronic Materials) and glass slides were used as the planar substrates for the hydrogel coating deposition. Track-etched polycarbonate membranes (Nuclepore) with pore

density of 3 X 10^8 pores/cm^2 and thickness of 10 μm were purchased from Fisher Scientific and used as the porous substrate.

6.2.2 Synthesis

Vapor deposition of hydrogel coatings was implemented in a custom-built reactor (Sharon Vacuum) with 25 cm in diameter and covered with a quartz plate for visual inspection. The reactor was equipped with a parallelly mounted Nichrome filament array (Ni80/Cr20, Goodfellow) 2.5 cm above the stage, where the planar and porous substrates were placed on. During deposition, the DMAEMA and EGDA monomers were vaporized at 50 °C and 60 °C in glass jars respectively, while the initiator TBP was vaporized at room temperature. The vapors were metered using mass flow controllers (MKS, model 1153, 1150, and 1479A), mixed and fed into the reactor. The flow rate of TBP was kept constant at 0.4 sccm. The flow rates of DMAEMA and EGDA were varied in the range of 0.45-0.75 sccm and 0.05-0.1 sccm, respectively, to obtain coatings with different composition. The filament was resistively heated to 210 °C during deposition, while the temperature of the substrate was maintained at 40 °C by water circulation at the backside of the stage. The temperatures were monitored by thermocouples (Omega, Type K) directly attached to the filament and the stage. The pressure inside the reactor was maintained at 0.25 Torr during deposition by a throttling butterfly valve (MKS, Type 253B). The growth of the hydrogel coatings on the reference surface of a silicon wafer was monitored real time using an interferometry system with a 633 nm He-Ne laser (JDS Uniphase). The average deposition rate on planar substrates was 20 nm/min.

6.2.3 Characterizations

Fourier transform infrared (FTIR) spectra of the hydrogel coatings were collected by a Nicolet 6700 FTIR spectrometer using a DTGS detector under the transmission mode at a 4 cm^{-1} resolution. The morphology of the pristine and coated membranes was observed using a FEI Quanta 600F scanning electron microscope (SEM). To observe hydrogel coatings inside the membrane pores, the coated membranes were immersed in chloroform (99%, Sigma-Aldrich) to dissolve the polycarbonate membrane, resulting in hydrogel nanotube structures. The remained hydrogel nanotubes were collected on copper grids and observed using a JEOL JEM 100CX II transmission electron microscope (TEM).

6.2.4 Swelling test and flow measurement

The swelling ratio of the synthesized hydrogel coatings at different temperatures was tested by measuring the water uptake of each coating. The thickness of the as-deposited coatings was approximately 1 μm. Prior to the test, each coating was soaked in deionized water to remove any un-crosslinked component. The dry-state weight of the coating was then determined by subtracting the weight of the substrate before deposition from the weight of the coated substrate. In each swelling test, a hydrogel coating was immersed in deionized water at a specific temperature for 3 min. After taking out the coating, the excess water on the coating surface was removed by gently tapping a wetted filter paper on the surface. The coating was weighed and reimmersed repeatedly until the amount of water uptake reached a stable value. At least four tests were taken for each coating composition at a particular temperature. The swelling ratio (*SR*) was calculated as

$SR= (W-W_0)/W_0$, where W is the weight of the hydrated coating and W_0 is the dry-state weight of the coating.

Flow measurement was conducted on both pristine and hydrogel coated polycarbonate membranes using a filtration cell with an effective filtration area of 1.1 cm^2. BSA (Sigma-Aldrich) was used as the model permeant, and a phosphate buffer solution (PBS) with an ionic strength of 30 mM was used as the carrier solution. The filtration cell has an initial BSA concentration of 10 and 0 mg/ml on the donor and receptor side, respectively. All measurements were performed in an incubator (Isotemp, Fisher Scientific) at the desired temperature. The hydrogel coated membrane was pretreated by soaking in PBS for 5 min and loaded into the filtration cell. The gravimetric flow measurement was carried out over a 2-hr period, and repeated for at least three times. The hydraulic pressure applied on the membrane was kept at 450 Pa. The amount of released BSA was determined by measuring the UV absorbance of the receptor solution at 280 nm at room temperature using a UV-Vis spectrometer (Cary 50 Bio) and converted to the mass of BSA using a calibration curve. The volumetric flow rate (Q) of the BSA solution was calculated from the slope of the mass-time curve according to the equation of $Q=m/(c_0 \cdot t)$, where m is the mass of the released BSA, t is the time of flow, c_0 is the concentration of BSA solution in the donor compartment, which was maintained constant at 10 mg/ml.

6.3 Results and discussion

6.3.1 Synthesis of P(DMAEMA-*co*-EGDA) hydrogels

P(DMAEMA-*co*-EGDA) films with systematically varied composition were synthesized using vapor deposition. Figure1a shows the FTIR spectra of the synthesized copolymer films compared with that of the PDMAEMA film. The vapor-based process well preserved the desired functional groups. The absorption peaks at 2823 and 2774 cm^{-1} are assigned to the C-H stretching in the $-N(CH_3)_2$ groups (N-C-H), while the strong absorption peaks centered in the range of 1729 to 1735 cm^{-1} are assigned to the C=O stretching absorption from both DMAEMA and EGDA units. In the spectra of PDMAEMA and PEGDA films, the C=O stretching from DMAEMA and EGDA centers at 1729 cm^{-1} and1735 cm^{-1}, respectively. Figure1b shows an enlargement of the carbonyl absorption in P(DMAEMA-*co*-EGDA) films. The peak position of the C=O stretching gradually shifts from 1729 to 1735 cm^{-1}, indicating an increase of the EGDA content in the copolymer. As the EGDA content increases, the overall intensity of the C=O stretching increases because of the two C=O bonds in each EGDA unit, while the intensity of the N-C-H peaks at 2823 and 2774 cm^{-1} decreases due to the reduced percentage of DMAEMA.

The molar ratio of EGDA to DMAEMA in each hydrogel was calculated using FTIR quantification. Details of the calculation have been reported previously.[33,35] The FTIR spectra of the P(DMAEMA-*co*-EGDA), PDMAEMA and PEGDA (not shown) films were normalized to the thickness of each film. The peak area ratio of the C=O

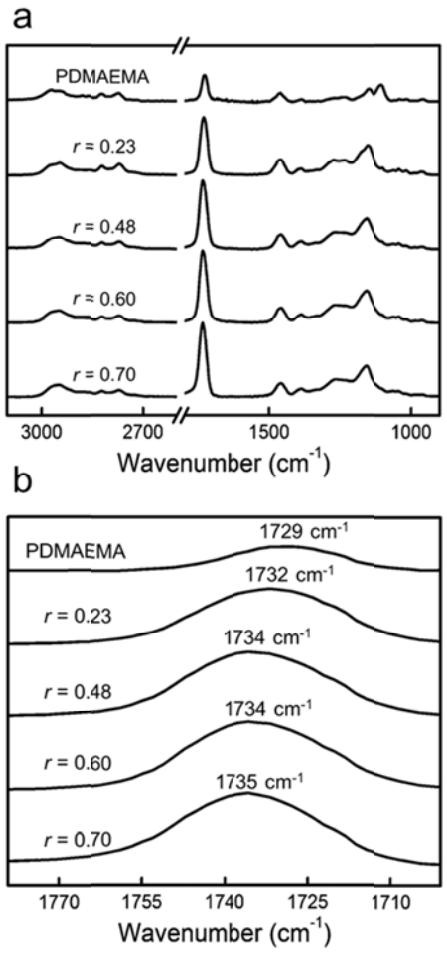

Figure 6-1: a) FTIR spectra of the vapor-deposited PDMAEMA and P(DMAEMA-*co*-EGDA) films with different molar ratio of EGDA to DMAEMA (*r*), b) the enlarged region of the carbonyl absorption peaks.

stretching at 1729 cm^{-1} ($A_{C=O}$') to the N-C-H stretching at 2773 cm^{-1}($A_{N\text{-}C\text{-}H}$') in the PDMAEMA homopolymer was calculated and denoted as $X=A_{C=O}'/A_{N\text{-}C\text{-}H}'$. The peak areas of the C=O ($A_{C=O}$) and N-C-H stretching ($A_{N\text{-}C\text{-}H}$) in the copolymer films were also measured. Under the assumption that the absorption coefficients of C=O and N-C-H stretching are the same both in the PDMAEMA homopolymer and copolymer, the peak area of the C=O stretching contributed by DMAEMA in the copolymer can be expressed

as $A_{C=O(DMAEMA)}=X\cdot A_{N\text{-}C\text{-}H}$. Hence, the area of the C=O stretching contributed by EGDA in the copolymers can be calculated as $A_{C=O(EGDA)}=A_{C=O}-X\cdot A_{N\text{-}C\text{-}H}$. It should be noted that the absorption coefficient of the C=O stretching in EGDA and DMAEMA may vary. This difference was recognized by comparing the C=O stretching absorbance in the spectra of PDMAEMA ($A_{C=O(PDMAEMA)}$) and PEGDA ($A_{C=O(PEGDA)}$) at the same coating thickness. Assuming equal density of the two homopolymer films, the ratio of the C=O group molar concentration in PDMAEMA and PEGDA can be calculated as $M_{EGDA}/2M_{DMAEMA}$, where M_{EGDA} and M_{DMAEMA} are the molecular weight of the repeating unit of EGDA and DMAEMA, respectively. There is a factor of 2, because each EGDA unit contains two C=O groups. Therefore, the ratio of the absorption coefficient of the C=O stretching in PDMAEMA and PEGDA (R) was calculated using the equation:

$$R=\frac{2A_{C=O(PDMAEMA)}M_{DMAEMA}}{A_{C=O(PEGDA)}M_{EGDA}} \tag{6-1}$$

From the Beer-Lambert equation, the peak area of a particular oscillation mode is proportional to the mole concentration and absorption coefficient of the corresponding moiety. Therefore, the molar ratio of EGDA to DMAEMA in each copolymer film (r) can be calculated using the equation:

$$r=\frac{(A_{C=O}-XA_{N-C-H})R}{2XA_{N-C-H}} \tag{6-2}$$

A factor of 2 was introduced because of the two C=O bonds in each EGDA unit. The calculated molar ratios are listed in Figure 6-1a.

6.3.2 Thermo-responsive swelling of hydrogel coatings

The thermo-responsive behavior of the vapor deposited hydrogel thin films was examined by measuring their swelling ratios as a function of temperature. The swelling ratio is defined as the weight of water uptake relative to the dry-state weight of the thin films. Though PDMAEMA-based hydrogels have been reported to swell more than 40 times at the free state,[36] the thin film counterparts are expected to have lower swelling ratio than that of bulk hydrogels due to the confinement imposed by solid surfaces.[37] For the vapor deposited P(DMAEMA-*co*-EGDA) hydrogel, a swelling ratio of 15.4 was observed for the coating with r=0.23 at 23 °C (Figure 6-2). The high water uptake of the coatings can be meaningful in membrane applications to prevent protein fouling.[38]

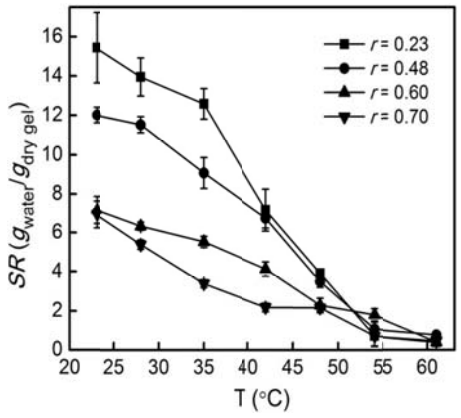

Figure 6-2: The temperature dependence of the swelling ratio (*SR*) of P(DMAEMA-*co*-EGDA) hydrogel.

As the temperature increased, the swelling ratio decreased significantly. At 54 °C and 61 °C, most films showed swelling ratios of less than 0.5. This transition is attributed to the change of intermolecular hydrogel-water hydrogen bonding to intramolecular hydrogen bonding in the hydrogel with the elevation of temperature.[39,40] The transition

temperature was estimated to be in the range of 40 to 45 °C. The broad transition temperature range is attributed to the crosslinked structure of the hydrogel, which is consistent with findings from previous studies.[36,41]

Another clear trend is that the swelling ratio of the film decreased with the increase of the EGDA content, because the increasing degree of crosslinking prevents the hydrogel network from swelling. It is also observed that hydrogel films with lower EGDA/DMAEMA ratio showed much steeper temperature response, while the response became linear as the EGDA/DMAEMA ratio increases. The linearization of temperature response with the increase of crosslinking density is in good agreement with results reported on crosslinked PNIPAm hydrogels.[10] As hydrogels with sharp responses are perfect candidate materials for fast-response and sensitive devices, hydrogels with linear transition region may have potential applications in linear temperature-sensitive actuators.

6.3.3 Fabrication of thermo-responsive nanovalves

Thermo-responsive nanovalves were fabricated by depositing the P(DMAEMA-*co*-EGDA) hydrogels along the sidewalls of the nanopores in the polycarbonate membranes (Figure 6-3). The P(DMAEMA-*co*-EGDA) hydrogel with r = 0.60 was used to demonstrate the concept. The swollen and collapsed states of the hydrogel coatings were exploited to realize the "closed" and "open" states of the nanopores, respectively. The pristine polycarbonate membranes (M_0) were track-etched with parallel cylindrical pores with an average diameter of ca. 166 nm as observed from SEM (Figure 6-4a). It is noted that the etching process created enlarged openings in some areas due to the connection of neighboring pores (Figure S6-1). Taking advantage of the vapor deposition method,

ultrathin hydrogel coatings were deposited into the nanopores at controlled coating thickness, resulting in coated membranes M_1, M_2, and M_3 with decreasing pore sizes (Figure 6-4(b-d)). The pores at the bottom surface were observed to be larger than the pores at the top of the same membrane. For example, the average pore radius of M_1 is 60 nm at the bottom (Figure S6-2) and 48 nm at the top. The difference between pore size at the top and bottom surfaces may be caused by the competition between monomer vapor diffusion and monomer consumption to form coatings along the cylindrical pores (aspect ratio ~60), which resulted in faster coating growth around the entrance region compared to the bottom part of the pores. This issue can be alleviated by lowering the coating growth rate through the adjustment of process conditions such as the initiator partial pressure.[42,43] Nevertheless, the distribution of the hydrogel coatings are uniform locally, with a gradual variation of thickness at different sections of the cylindrical pores, as shown in the TEM images of the remained hydrogel nanotubes (Figure 6-5) after dissolving the polycarbonate membrane.

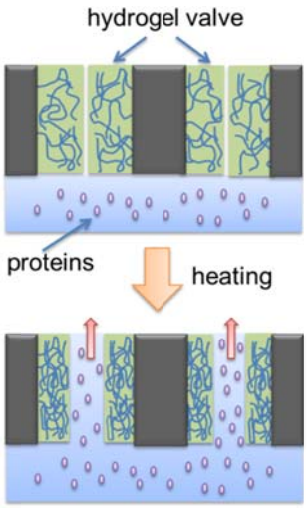

Figure 6-3: Schematics of the thermo-responsive hydrogel nanovalves for flow regulation.

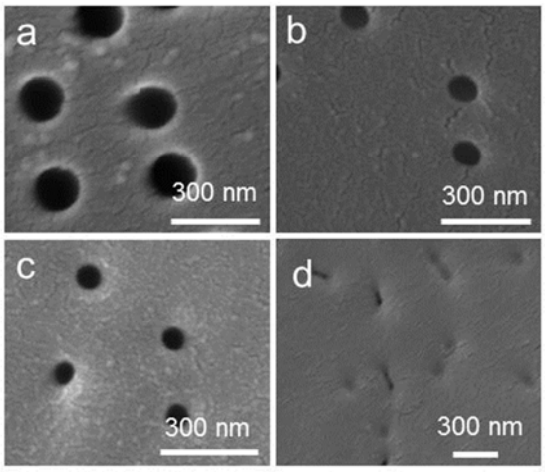

Figure 6-4: SEM images of a) pristine polycarbonate membrane (M_0), hydrogel-coated membranes with coating thicknesses of ca. b) 35 nm (M_1), c) 47 nm (M_2) and d)83 nm (M_3).

The thermo-responsive gating of the hydrogel nanovalves was examined by measuring the amount of BSA released through the hydrogel coated membranes at different temperatures. The release profile of BSA at 25 °C and 60 °C was plotted in Figure 6-6. At 60 °C, the total amount of released BSA is linear with time during the test period, while the BSA release profile at 25°C is flat with negligible release. The BSA flow rate at 60 °C is approximately 10 times that of 25 °C. The data confirms that the nanopores can be switched "open" or "closed" by responding to the temperature change. This phenomenon also indicates that the hydrogel swells at 25 °C to block the flow of BSA molecules through the nanopores and collapses at 60 °C to open the nanopores for the BSA release. The non-zero release of BSA at 25 °C is ascribed to the possible incomplete coverage of the interconnected pores (Figure S6-1) even at the hydrogel swollen state. Another possible reason is the diffusion of BSA through the meshes inside the hydrogel at the swollen state. However, as to be discussed below, the swelling of the hydrogel in the nanopores is suppressed due to the confined geometry, which may

significantly restrict the expansion of the meshes to allow the BSA molecules to diffuse through.

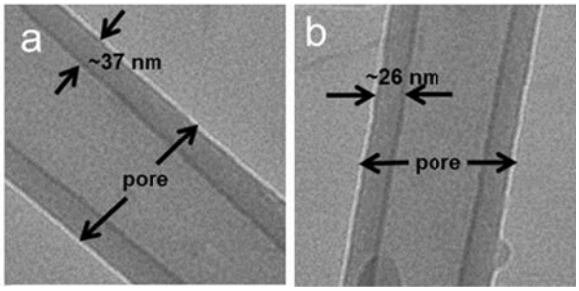

Figure 6-5: TEM images of the hydrogel nanotubes after dissolving the polycarbonate membrane. a) and b) are different sections of the nanotubes. The marked thickness indicates the local coating thickness.

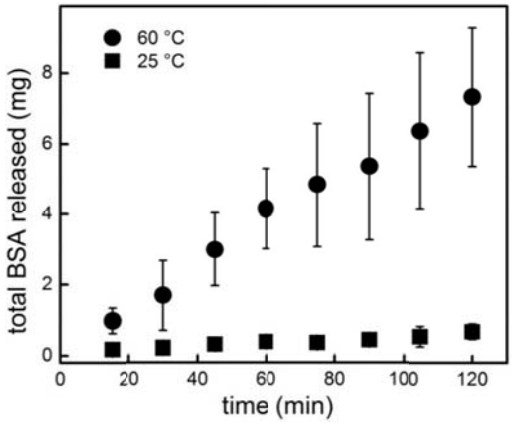

Figure 6-6: The total amount of BSA released through the membrane of M_2 as a function of time at 25 °C and 60 °C.

6.3.4 Flow regulation

In addition to the gating of the nanopores, the vapor-deposited hydrogel coatings enable fine regulation of the permeant flow through the nanopores by forming pores with varied dimensions. Figure 6-7 shows the flow rates of BSA solution through membranes of M_0, M_1, M_2, and M_3 at 60 °C and 25 °C. To exclude the effect of temperature-induced viscosity change, the flow rate of BSA at 60 °C was corrected with respect to the viscosity.[20,44] It is evident that the flow rates at both 60 °C and 25 °C decreased dramatically with the decrease of pore size. For the membranes of M_1 and M_2, the flow rate was larger at 60 °C than at 25 °C at the same pore size, indicating the enlargement of nanopores due to the collapse of the hydrogel above the transition temperature. The flow was negligible in M_3 at both 60 °C and 25 °C because of the sealing of the nanopores at both temperatures.

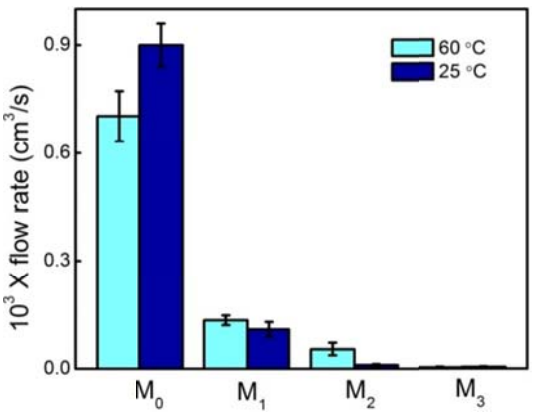

Figure 6-7: Flow rate of BSA solution through the pristine membrane (M_0) and coated membranes (M_1, M_2 and M_3) at 60 °C and 25 °C. The flow rates at 60 °C were corrected with respect to the viscosity.

Swelling of hydrogels in a confined space can be significantly different from hydrogel swelling in a less restricted space. The swelling ratio of hydrogel films in 800-nm pores has been reported to be three times smaller than that on planar surfaces.[7] To quantitatively analyze the swelling of the P(DMAEMA-*co*-EGDA) hydrogel inside the nanopores, the Hagen-Poiseuille (HP) equation[45] was introduced:

$$Q = \frac{nA\pi r^4 \Delta P}{8\tau\mu l} \tag{6-3}$$

where Q is the volumetric flow rate, n is the pore density defined as the number of pores per unit area, A is the total area of the membrane, r is the radius of the pores, ΔP is the pressure difference across the membrane, τ is the tortuosity of the pores, μ is the viscosity of the fluid, and l is the thickness of the membrane. Using equation (6-3), the HP effective pore size of hydrogel coated membranes at different temperatures can be calculated from the flow rates.

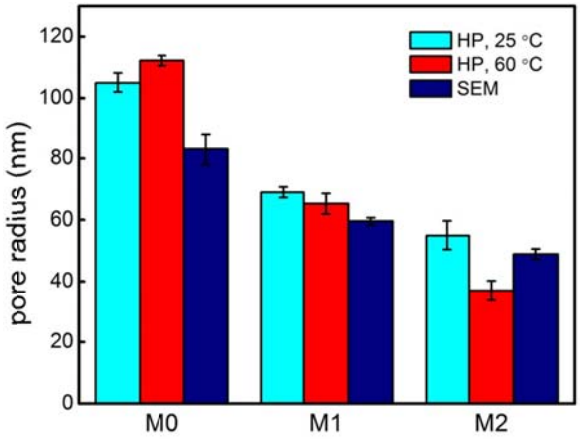

Figure 6-8: The HP pore radius of the membranes calculated based on the flow rate, compared with the dry-state pore radius observed from SEM.

Figure 6-8 shows the HP pore size of the membranes at 25 and 60°C compared with the dry-state pore size, which is the average of the pore sizes at the top and bottom surfaces observed from SEM. Interestingly, the estimated pore size of both the pristine and coated membranes at 60°C was larger than the dry-state pore size. It has been reported in several studies that the calculation using HP equation tends to overestimate the size of cylindrical pores in polycarbonate membranes.[7,46,47] The disparity may originate from the overlapping of some neighboring pores in the membrane manufacturing process (Figure S6-1), which was not taken into consideration in the calculation of the dry-state pore size.

While we do not expect a precise calculation of the pore size from the HP equation, it provides a relative scale estimation of the pore dimensions at different temperatures. By comparing the HP pore radiuses of M_1 and M_2 at 60 °C and 25 °C, the hydrogel coating thickness was calculated (Table 6-1). The coating thickness increased with the decrease of temperature, indicating temperature-induced swelling inside the nanopores. However, compared with the swelling change for the same coating from 60 °C to 25 °C on planar surfaces in the PBS solution, which is more than 5-fold (Figure S6-3), the swelling change inside the nanopores is much smaller. The suppressed swelling is mainly resulted from the space confinement imposed by the sub-100 nm pores.[7] It is noted that the temperature-induced swelling change in the membrane of M_2 (~80%) is more significant than that of M_1 (~30%), possibly due to the weakened surface constraint with the increase of coating thickness.[37]

Table 6-1: The effective coating thicknesses calculated using the HP equation.

	estimated coating thickness (nm)	
membrane	60 °C	25 °C
M_1	14 ± 2	18 ± 3
M_2	26 ± 4	47 ± 3

6.4 Conclusions

Thermo-responsive hydrogel coatings of P(DMAEMA-*co*-EGDA) were synthesized using chemical vapor deposition. High swelling ratios of more than 15-fold were observed at room temperature. The hydrogel coatings showed dramatic decrease in the swelling ratio with the elevation of temperature. The swelling was also affected by the crosslinking density of the hydrogel. Thermo-responsive hydrogel nanovalves were fabricated inside the nanoporous membranes using the single-step vapor deposition process. SEM and TEM observations demonstrated sub-50 nm coatings with controllable thicknesses along the sidewall of the nanopores. The "closed" and "open" states of the nanopores for the BSA flow were achieved by varying the temperature. We also demonstrated fine regulation of flow through the nanopores by varying the hydrogel coating thickness. The temperature-induced swelling change in the nanopores was estimated to be much smaller compared with the swelling change of the same coating on planar surfaces. Although we used the track-etched polycarbonate membrane as a model substrate, this vapor-based hydrogel coating method can be applied on a wide variety of substrates, since it bypasses the use of any organic solvent and employs only mild

conditions during the process. We expect a wide spectrum of potential applications for the vapor deposited responsive coatings, including controlled release, sensors and actuators.

6.5 Acknowledgements

Financial support for this research was provided by the Oklahoma Center for the Advancement of Science and Technology (Award # ONAP 09-12 and AR 09.02-024). We also thank the Oklahoma State University Microscopy Laboratory for SEM and TEM experiments.

6.6 References:

1. S. Chaterji, I. K. Kwon and K. Park, *Prog. Polym. Sci.*, 2007, **32**, 1083-1122.
2. E. S. Gil and S. M. Hudson, *Prog. Polym. Sci.*, 2004, **29**, 1173-1222.
3. D. Roy, J. N. Cambre and B. S. Sumerlin, *Prog. Polym. Sci.*, 2010, **35**, 278-301.
4. M. A. C. Stuart, W. T. S. Huck, J. Genzer, M. Muller, C. Ober, M. Stamm, G. B. Sukhorukov, I. Szleifer, V. V. Tsukruk, M. Urban, F. Winnik, S. Zauscher, I. Luzinov and S. Minko, *Nature Mater.*, 2010, **9**, 101-113.
5. I. Tokarev and S. Minko, *Soft Matter*, 2009, **5**, 511-524.
6. J. Wu and M. Sailor, *Adv. Funct. Mater.*, 2009, **19**, 733-741.
7. D. Lee, A. J. Nolte, A. L. Kunz, M. F. Rubner and R. E. Cohen, *J. Am. Chem. Soc.*, 2006, **128**, 8521-8529.
8. A. Richter, G. Paschew, S. Klatt, J. Lienig, K. F. Arndt and H. J. P. Adler, *Sensors*, 2008, **8**, 561-581.
9. S. Singamaneni, M. C. LeMieux, H. P. Lang, C. Gerber, Y. Lam, S. Zauscher, P. G. Datskos, N. V. Lavrik, H. Jiang, R. R. Naik, T. J. Bunning and V. V. Tsukruk, *Adv. Mater.*, 2008, **20**, 653-680.
10. H. van der Linden, W. Olthuis and P. Bergveld, *lab chip*, 2004, **4**, 619-624.
11. A. K. Bajpai, S. K. Shukla, S. Bhanu and S. Kankane, *Prog. Polym. Sci.*, 2008, **33**, 1088-1118.
12. N. S. Satarkar, D. Biswal and J. Z. Hilt, *Soft Matter*, 2010, **6**, 2364-2371.
13. T. Hoare, J. Santamaria, G. F. Goya, S. Irusta, D. Lin, S. Lau, R. Padera, R. Langer and D. S. Kohane, *Nano Lett.*, 2009, **9**, 3651-3657.
14. E. Miyako, H. Nagata, K. Hirano and T. Hirotsu, *Small*, 2008, **4**, 1711-1715.
15. R. P. Shaikh, V. Pillay, Y. E. Choonara, L. C. du Toit, V. M. K. Ndesendo, P. Bawa and S. Cooppan, *Aaps Pharmscitech*, 2010, **11**, 441-459.
16. D. Wandera, S. R. Wickramasinghe and S. M. Husson, *J. Membr. Sci.*, 2010, **357**, 6-35.
17. I. Tokarev and S. Minko, *Adv. Mater.*, 2010, **22**, 3446-3462.
18. H. J. Dai, Q. Chen, H. L. Qin, Y. Guan, D. Y. Shen, Y. Q. Hua, Y. L. Tang and J. Xu, *Macromolecules*, 2006, **39**, 6584-6589.
19. F. Schacher, T. Rudolph, F. Wieberger, M. Ulbricht and A. H. E. Muller, *ACS Appl. Mater. Interfaces*, 2009, **1**, 1492-1503.
20. F. Schacher, M. Ulbricht and A. H. E. Muller, *Adv. Funct. Mater.*, 2009, **19**, 1040-1045.
21. K. Zhang and X. Y. Wu, *Biomaterials*, 2004, **25**, 5281-5291.
22. W. Lequieu, N. I. Shtanko and F. E. Du Prez, *J. Membr. Sci.*, 2005, **256**, 64-71.
23. R. Xie, Y. Li and L. Y. Chu, *J. Membr. Sci.*, 2007, **289**, 76-85.
24. T. Yamakawa, S. Ishida and M. Higa, *J. Membr. Sci.*, 2005, **250**, 61-68.
25. B. Yang and W. T. Yang, *J. Membr. Sci.*, 2003, **218**, 247-255.
26. T. Nonaka, T. Ogata and S. Kurihara, *J. Appl. Polym. Sci.*, 1994, **52**, 951-957.
27. L. Ying, E. T. Kang, K. G. Neoh, K. Kato and H. Iwata, *J. Membr. Sci.*, 2004, **243**, 253-262.
28. M. Vertommen, H. J. L. Cornelissen, C. Dietz, R. Hoogenboom, M. F. Kemmere and J. T. F. Keurentjes, *J. Membr. Sci.*, 2008, **322**, 243-248.
29. A. Asatekin, M. C. Barr, S. H. Baxamusa, K. K. S. Lau, W. Tenhaeff, J. J. Xu and K. K. Gleason, *Mater. Today*, 2010, **13**, 26-33.
30. Y. V. Pan, R. A. Wesley, R. Luginbuhl, D. D. Denton and B. D. Ratner, *Biomacromolecules*, 2001, **2**, 32-36.
31. P. A. Tamirisa, J. Koskinen and D. W. Hess, *Thin Solid Films*, 2006, **515**, 2618-2624.
32. P. A. Tamirisa and D. W. Hess, *Macromolecules*, 2006, **39**, 7092-7097.
33. K. Chan and K. K. Gleason, *Langmuir*, 2005, **21**, 8930-8939.

34. Y. Mao and K. K. Gleason, *Macromolecules*, 2006, **39**, 3895-3900.
35. Y. M. Ye, Q. Song and Y. Mao, *J. Mater. Chem.*, 2011, **21**, 257-262.
36. S. H. Yuk and S. H. Cho, *Eur. Polym. J.*, 2001, **37**, 1985-1989.
37. R. Toomey, D. Freidank and J. Ruhe, *Macromolecules*, 2004, **37**, 882-887.
38. H. Susanto and M. Ulbricht, *Langmuir*, 2007, **23**, 7818-7830.
39. F. Xia, L. Feng, S. T. Wang, T. L. Sun, W. L. Song, W. H. Jiang and L. Jiang, *Adv. Mater.*, 2006, **18**, 432-436.
40. T. L. Sun, G. J. Wang, L. Feng, B. Q. Liu, Y. M. Ma, L. Jiang and D. B. Zhu, *Angew. Chem. Int. Ed.*, 2004, **43**, 357-360.
41. F. A. Plamper, A. Schmalz, M. Ballauff and A. H. E. Muller, *J. Am. Chem. Soc.*, 2007, **129**, 14538-14539.
42. K. K. S. Lau and K. K. Gleason, *Macromolecules*, 2006, **39**, 3688-3694.
43. K. K. S. Lau and K. K. Gleason, *Macromolecules*, 2006, **39**, 3695-3703.
44. U. Gunduz, *J. Chromat. B, Analyt. Technol. Biomed. Life Sci.*, 2004, **807**, 157-161.
45. M. M. Denn, *Process fluid mechanics*, PTR Prentice Hall: Englewood Cliffs, NJ, 1980.
46. V. Smuleac, D. A. Butterfield and D. Bhattacharyya, *Chem. Mater.*, 2004, **16**, 2762-2771.
47. K. J. Kim and P. V. Stevens, *J. Membr. Sci.*, 1997, **123**, 303-314.

6.7 Supporting Information

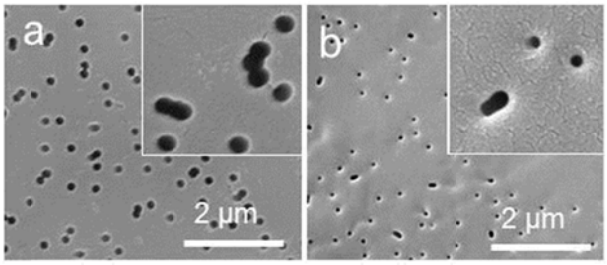

Figure S6-1 SEM images of the a) pristine polycarbonate membrane and b) hydrogel-coated membrane (M_2) viewed at the top surfaces. Inset: enlarged view of some interconnected pores.

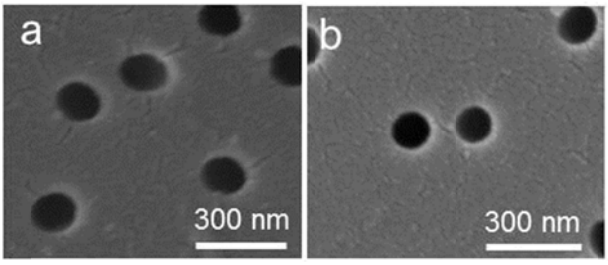

Figure S6-2 SEM images of the bottom surfaces of a) M_1 and b) M_2.

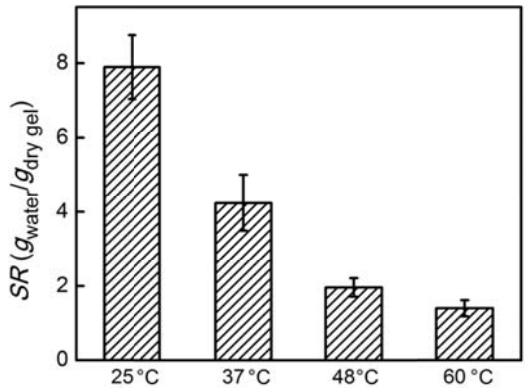

Figure S6-3 Swelling ratio of the P(DMAEMA-*co*-EGDA) coatings with r = 0.60 in the PBS solution.

CHAPTER VII

CONCLUSIONS AND FUTURE WORK

Initiated chemical vapor deposition is a versatile technique in producing polymeric thin films. The excellent combination of two distinct processes, chemical vapor deposition and free radical polymerization, enables applications that are difficult to achieve using conventional solution- and vapor-based methods. Two unique merits of the process are highlighted: the ability to conformally coat nanoscale-featured substrates without bringing any damage to the original structure; and the ability to fully preserve the delicate functional groups of the precursor monomer and provide stoichiometric control of the coating composition. The work in this thesis proved the promising applications of iCVD in bioengineering by demonstrating successful surface functionalization of nano- and microstructured materials.

Chapter II presentd a novel vapor-based hybrid grafting method of antimicrobial polymers to modify catheter surfaces. The hybrid graft coatings consisted of a vapor-crosslinked prime layer, as previously reported, and a subsequently grafted homopolymer layer. The iCVD process demonstrated systematic control over the composition of the crosslinked copolymer and perfect retention of the functionality of the dimethylaminomethylstyrene monomer. The vapor-crosslinking and hybrid grafting processes were proved to be applicable to substrates with complex structures (e.g. textiles), and substrates with thermal- and solvent-sensitivity (e.g. catheters). It is noted that this is the first successful attempt to employ the solvent-free approach to fabricate antimicrobial catheters.

Chapter III, IV and V focused on the functionalization of both vertically aligned single- and multi-walled carbon nanotube arrays in non-covalent and covalent ways using iCVD method. The iCVD method was proved to be ideal for VACNT functionalization,

as its solventless nature avoids any disruption of the aligned morphology, which is difficult to achieve using solution-based approaches. We demonstrated the iCVD functionalization of VACNTs with epoxy chemistry, which can undergo further chemical reactions for future applications. The epoxy functionalization enabled successful transfer of multi-walled carbon nanotube (MWNT) arrays, which were proven to significantly enhance its mechanical strength and wetting stability. Covalent functionalization was achieved on single walled carbon nanotube (SWNT) arrays, which was confirmed by Raman spectroscopy and terahertz time-domain spectroscopy. The covalent grafting of polymer altered the electronic structure of the nanotube arrays, which revealed the possibility of modulating optical and electronic properties of SWNT arrays using vapor phase approaches.

Functionalization of vertically aligned MWNT arrays with low site density was demonstrated in chapter V. Low site density carbon nanotube arrays are advantageous over closely packed carbon nanotube arrays in biosensor fabrication. However, they are also proven to be difficult to treat using solution-based approaches. The iCVD process enabled hydrogel functionalization of nanotube arrays with perfect retention of the original array structure and controllable coating thicknesses. The hydrogel coatings significantly enhanced the wettability of the nanotube arrays and imparted pH-responsiveness. Nanostructured materials such as vertically aligned carbon nanotube arrays are extensively researched for their exceptional properties and numerous potential applications. The iCVD technique provides a unique and powerful tool to help realize these applications by modifying and functionalizing the surfaces.

We further explored iCVD coating of another type of responsive polymer—thermo-responsive hydrogel on nanoporous membranes in Chapter VI. Using iCVD coating, sub-50 nm hydrogel coatings with stoichiometric chemistry were uniformly deposited along the nanopores. We demonstrated the fabricated "smart nanovalves" modulated biomolecule transportation by the control of temperature change. Thin hydrogel coatings are especially important in bioengineering applications. However, other vapor deposition methods such as PECVD are not fully capable of fabricating hydrogel coatings with stoichiometric control of the coating composition, which is a key parameter in achieving the desired hydrogel functionalities. The iCVD process has been demonstrated to provide precise and systematic control of the coating composition by simply adjusting the flow rates of the precursors.

Since the first attempt of introducing an initiator in the chemical vapor deposition of polymer films, iCVD has undergone a rapid development in both mechanism exploration and practical application endeavors. However, the mechanism and kinetics of the process is still not fully understood. We believe more detailed research in the relation of deposition parameters (e.g. filament and substrate temperature, pressure, and initiator type) with the properties of polymer coatings (e.g. molecular weight, coating structure, and copolymer composition) is necessary in order to further push the development of iCVD to real-world applications. Meanwhile, attempting to utilize more types of monomers in the deposition would realize more diversified applications not only in the bioengineering, but in miniaturized device fabrication, novel nanocomposites, etc. Explorations in the different choices of initiators could enable the possibility of

accelerating the deposition rate and adjusting the deposition kinetics, which are important in scaling up the fabrication process.

APPPENDIX A

FACAILE SYNTHESIS AND MICROPATTERNING OF FUNCTIONALLY GRADED FREE-STANDING THIN FILMS BY VAPOR DEPOSITION

Yumin Ye, Yu Mao, “Facile synthesis and micropatterning of functionally graded free-standing thin films by vapor deposition”. (In preparation)

Abstract

We introduce a novel facile approach of synthesizing functionally graded free-standing films using vapor deposition. Unlike traditional liquid-based layer-by-layer assembly, which has limitations in incorporating nonpolar or uncharged components, the vapor-crosslinking process is able to incorporate different surface functionalities such as hydrophilicity (hydrogel) and hydrophobicity (fluorine polymers) without changing the bulk property. The functionally graded films were easily exfoliated from the substrates after immersing in deionized water because of the swelling of hydrogel layer. Attenuated total reflectance Fourier transform infrared spectroscopy and contact angle measurement confirmed the successful incorporation of desired chemical composition and functionalities at the surface. The free-standing film was optically transparent and mechanically strong. Furthermore, by simply applying a SiN template, functional polymer micropatterns were deposited on a free-standing film. Scanning electron microscope and atomic force microscope revealed highly ordered patterns with 2 μm in diameter and 300 nm in thickness. The micropatterned free-standing films are flexible and can be attached to both flat and curved surface, indicating the potential applications as miniaturized patchable sensors.

A.1 Introduction

Free-standing polymeric films are of great interests in a wide range of applications, such as semipermeable membranes,[1,2] flexible optical and electronic devices,[3,4] miniaturized sensors,[5,6] mechanically reinforced nanocomposites,[7,8] drug delivery,[9] biomimetics,[10,11] and tissue engineering.[11-13] Two elements are considered essential for the successful utilization of polymeric films in many situations: the precise control of the bulk property, such as mechanical strength and optical transparency, and the fine tuning of the surface functionality, such as hydrophilicity/hydrophobicity and protein repulsion. To achieve the desired surface functionality while preserving the bulk property, a common strategy is to introduce a compositional difference between the film surface and the bulk, which can be achieved by constructing a film structure with multiple layers.[14,15] Recent development of nanofabrication techniques enables nanoscale control of the film composition, which facilitates the fabrication of layer-structured functional polymeric thin films.

To date, a number of approaches to the fabrication of layered free-standing polymeric films have been reported, such as layer-by-layer (LbL) assembly,[15,16] Langmuir-Blodgett method,[17] and recognition-mediated self-assembly.[18,19] The method of LbL assembly has received much attention and has been extensively investigated over the past decade. The solution-based method creates a multi-bilayer structure by alternate and repetitive adsorption of oppositely charged species or hydrogen-bond acceptors and donors. The ability to easily manipulate the composition of the thin film at the nanometer length scale enables the fabrication of multilayered ultrathin films with finely tuned functionalities. Recent advances in the LbL assembly technique have broadened the choices of building blocks from pure polyelectrolyte systems to nanoparticles,[20]

nanotubes,[21,22] nanoplates,[8,23] and biomolecules,[24,25] which offers new functionalities and architectures. In addition, the LbL assembly method can be combined with inexpensive patterning techniques, offering the potential applications in the fabrication of sensors, optical and electrical devices, and microelectromechanical systems.[15]

Despite of its versatility and convenience, conventional LbL assembly technique has several limitations in extending its applications in certain areas. First, the deposition of each layer in LbL assembly is based on the electrostatic or hydrogen-bond interaction to the previously deposited layer, which increases the difficulty of incorporating nonpolar and uncharged components.[26,27] Second, since most LbL assembly methods use dipping or spin coating followed by rinsing off weakly adsorbed species,[15] the thickness of a single adsorbed layer is limited to several to several tens of nanometers; thus it is difficult to scale up the film thickness to beyond micrometers. Third, the integrity of the LbL assembled structures relies on the weak interaction between layers, namely electrostatic interaction, hydrogen-bond or Van der Waals force; the long-term stability in aqueous solutions is therefore hindered.[28,29] To improve the film stability, post-processing steps, such as heat-[30,31] or chemical[29,32]-induced crosslinking, need to be implemented. Recent reports demonstrated a modified LbL assembly technique using consecutively alternating spin coating and photo-crosslinking.[27,33,34] Both hydrophobic and hydrophilic components were deposited and UV-crosslinked into a multilayered structure. Since the crosslinked structure ensured high affinity to the substrate, no rinse of weakly adsorbed species was necessary, allowing the thickness of a single layer to extend to hundreds of nanometers.

Vapor deposition represents an alternative route to the fabrication of functional polymer thin films.[35-37] By flowing both monomers and the initiator in a heated vapor environment, polymerization occurs on the cooled substrates with a free radical mechanism. Crosslinkers such as ethylene glycol diacrylate can also be introduced, allowing dissolvable functional monomers to anchor onto substrates in the form of a two-dimensional polymeric network. Previously, we have demonstrated single-step synthesis of antimicrobial polymer coatings via vapor-crosslinking[38] and vapor-based hybrid grafting.[39] The crosslinked thin coatings exhibited durable bactericidal efficacy against continuous washing. In addition, free-standing films have also been fabricated using vapor deposition. By spin coating of a sacrificial layer, followed by vapor-crosslinking deposition of butyl acrylate, free-standing polymer films with thicknesses ranging from 500 nm to 5 μm were fabricated.[40] The obtained films were subsequently transferred onto a microfluidic lung assist device to achieve gas permeable membranes with water resistance.

In this study, we introduce a novel facile route of fabricating functionally graded free-standing thin films using vapor deposition. The vapor-based process enables fine tuning of the film composition along the vertical growth direction by simply adjusting the feed ratio of precursors *in situ*, resulting in a graded polymeric structure. The i*n situ* composition control also enables the intended distribution of the crosslinking degree across the film, which maintains the robustness of the film and surface functionality. As opposed to most LbL assembly methods, the vapor deposition process utilizes chemical crosslinking as the bonding mechanism between layers with different compositions;

therefore the integrity and stability of the film is significantly improved without the necessity of post-treatment.

We demonstrate the fabrication of functionally graded free-standing films with thicknesses from as low as 150 nm up to 10 μm. Both hydrophobic and hydrophilic components were incorporated and arranged in a pre-determined order. The incorporation of a thin poly(dimethyl amino ethyl methacrylate-*co*-ethylene glycol diacrylate) (P(DMAEMA-*co*-EGDA)) prime layer, which has proven to have high swelling ratio in neutral solutions,[41] enables easy exfoliation of the film from substrates upon immersion in deionized water; therefore additional procedures are avoided for the liberation of the film.[27,40] Characterization of both surface and bulk properties will be discussed. Employing the method of vapor-crosslinking deposition, we further demonstrate single-step patterning of micrometer-sized hydrogel domains on the free-standing films. The micropatterned film can be transferred onto surfaces with complex geometries, indicating the potential of applications in miniaturized device fabrications.

A.2 Experimental

Vapor deposition of graded free-standing films

The vapor deposition was carried out in a custom-built deposition reactor (Sharon Vacuum) as previously reported.[38,41] Briefly, precursor monomers of dimethyl amino ethyl methacrylate (DMAEMA, 98%, Sigma-Aldrich) and 1H,1H,2H,2H-perfluorodecyl acrylate (PFDA, 97%, Sigma-Aldrich), crosslinker ethylene glycol diacrylate (EGDA, 90%, Sigma-Aldrich) , and initiator *tert*-butyl peroxide (TBP, 98%, Sigma-Aldrich) were

heated to 50 °C, 80 °C, 60°C, and 25 °C respectively, and fed into the reactor. The reactor was equipped with parallelly arrayed Nichrome filament (Ni80/Cr20, Goodfellow) and water-cooled stage. The flow rate of the precursor monomers and initiator was adjusted by mass flow controllers (MKS, model 1153, 1150, and 1479A), while the flow rate of the crosslinker was adjusted by a manual needle valve. The actual flow rates of the precursors at different stages are listed in Table A-1. During deposition, TBP was thermally decomposed in the vicinity of the heated filament and initiated the polymerization on the substrates, which were cooled by the circulating water. The temperatures of the filament and substrates were kept at 250 °C and 35 °C respectively, as measured by directly attached thermal couples (Omega, type K). The pressure inside the reactor was maintained at 250 mTorr through the first two stages and decreased to 150 mTorr towards the end of the deposition (Table A-1) using a throttling butterfly valve (MKS, model 253B). An interferometry system with a 633 nm He-Ne laser (JDS Uniphase) was used to monitor the deposition process by measuring the thickness increase of the polymer films *in situ*. The deposition time spans from 5 to 120 min depending on the film thickness.

The as-deposited films were immersed in deionized water for 3 min in order to be released from the substrate. The edges of the films were cut by a diamond pen prior to the immersion to facilitate the penetration of water into the hydrogel prime layer. The released films with 10 μm thickness were easily collected by a pair of tweezers. To fabricate the ultrathin 150 nm free-standing film, a 1 μm sacrificial poly(dimethyl amino ethyl methacrylate) (PDMAEMA) coating was deposited on the Si wafer prior to the deposition to accelerate the exfoliation process.

Micropatterning of the free-standing films

Vapor-based micropatterning was conducted in the same reactor as previously described. A SiN mesh (DuraSiN$_{TM}$, Protochips) with a window area of 0.5 X 0.5 mm^2 supported by a 2.65 mm diameter Si frame was used as the template and placed on the substrates of Si wafer or free-standing films. The mesh has 2 μm holes and 2 μm hole-to-hole distance. A small droplet of water was placed on the mesh so that an intimate contact between the substrates and template can be created through the wetting and drying process. After vapor deposition, the template was lifted and the 2 μm patterns were formed on the substrate.

Characterizations

The contact angle of the free-standing films was measured at room temperature using a standard contact angle goniometer (Rame Hart, Model 250-F1) equipped with an automatic liquid dispensing system. For each measurement, a 10 μL droplet of deionized water was used, and the static contact angle was measured using images taken by a F4 series digital camera and analyzed by the DROPimage software. At least five measurements were taken on different spots of each film to acquire the standard deviation.

The morphology of the free-standing films and micropatterned surfaces was observed using an FEI Quanta 600F scanning electron microscope (SEM). The FTIR spectra of the films were collected by a Nicolet 6700 FTIR spectrometer under the attenuated total reflection (ATR) mode using a DTGS detector and a diamond crystal over the range of 400-4000 cm^{-1} at 4 cm^{-1} resolution. The surface topography of the free-

standing films was examined using a Veeco Multimode SPM atomic force microscope (AFM) under the tapping mode. The light transmittance of the film was measured using a UV-Vis spectrometer (Cary Bio 300, Varian) over a 350-800 nm range.

The fluorescent functionalization of the patterned free-standing films was performed by placing a drop of 1% fluorescein disodium solution (pH=7) on the patterned area and let it sit for 5 min. The film was then rinsed thoroughly and dried in air. The stained patterns were observed under an Olympus BX51 epifluorescence microscope using a green filter.

Nanoindentation

Nanoindentation measurements were conducted using a Nano Indenter XP system (MTS Systems Corporation). A diamond Berkovich tip with 65.3˚ center line to face angle was used in all measurements. The nanoindentation tests were conducted in the air at 23°C under a relative humidity of about 50%. The resolutions for load and displacement are 50 nN and 0.01 nm, respectively. The maximum load applied was 1mN at a loading rate of 0.02 mN/s, and the measured indenter tip drift rate was within ±0.02nm/s. In all the nanoindentation tests, the indentation depths were restrained within 10% of the film thickness to minimize any substrate effects. At least five nanoindentation tests were conducted at different locations for each sample, and the load-displacement curves were recorded.

The hardness (H) is obtained using

$$H = \frac{P_{max}}{A_c} \tag{1}$$

where P_{max} is the maximum indentation force, A_c is the contact area corresponding to the contact depth (h_c) at the maximum load, which is calculated based on the tip area function. To determine the modulus of the specimen, the reduced modulus of the specimen (E_r) is calculated at first using

$$\frac{1}{E_r} = \frac{1-\nu_s^2}{E_s} + \frac{1-\nu_i^2}{E_i} \tag{2}$$

where E_s and ν_s are the Young's modulus and Poisson's ratio of the specimen, respectively, and E_i and ν_i are the Young's modulus and Poisson's ratio of the indenter tip (made up of diamond), respectively. Due to finite stiffness of the indenter tip, its modulus is considered in the calculation of sand grain modulus from the contact stiffness. The contact stiffness S is calculated from the slope of the initial unloading curve,

$$S = \frac{dP}{dh} = \frac{2}{\sqrt{\pi}} E_r \sqrt{A_c(h_c)} \tag{3}$$

Equations (2) and (3) along with the known values of the area function of the nanoindenter tip, the indent depth, the slope of the unloading curve, and the Young's modulus and Poisson's ratio values for the indenter tip were used to determine the elastic modulus for a specimen.

The contact area, taken as function of contact depth after indenter shape calibration, has such form as follows

$$A = a_0 h_c^{\,2} + a_1 h_c + a_2 h_c^{\,1/2} + a_3 h_c^{\,1/4} + a_4 h_c^{\,1/8} \cdots \tag{4}$$

A.3 Results and discussions

A.3.1 Fabrication of graded free-standing films

As illustrated in Figure A-1a, the vapor deposition of graded polymer thin films was carried out in a three-stage process. The detailed deposition conditions are listed in Table A-1. At the initial stage, the vapors of TBP, DMAEMA, and EGDA were metered into the reactor, where TBP was decomposed by the heated filament, initiating the copolymerization of DMAEMA and EGDA on the substrates. A 200 nm layer of P(DMAEMA-*co*-EGDA) hydrogel was thus deposited as the prime layer of the graded film. The following deposition created a bulk layer of highly crosslinked poly(ethylene glycol diacrylate) (PEGDA) and a top surface layer of poly(1H,1H,2H,2H-perfluorodecyl acrylate) (PPFDA). To realize a gradual transition between the three layers and ensure the integrity of the film, two transitional layers of P(DMAEMA-*co*-EGDA) and poly(1H,1H,2H,2H-perfluorodecyl acrylate-*co*-ethylene glycol diacrylate) (P(PFDA-*co*-EGDA)) were introduced between the surface and bulk layers. The resultant film has a high crosslinking degree in the bulk, but the crosslinking degree substantially decreases at the two surfaces, resulting in a robust structure with maximized surface functionalities. It is noted that the monomers with other functionalities can be anchored onto the two sides of the film using this method as well.

Table A-1 Deposition conditions of the 10 µm free-standing film at different stages.

stage	layer	FR^{*}_{DMAEMA} (sccm)	$FR_{crosslinker}$ (sccm)	FR_{PFDA} (sccm)	$FR_{initiator}$ (sccm)	pressure (torr)	deposition thickness (µm)
I	prime layer	1.5	0.2	0	0.8	0.25	0.2
	transitional layer	1.5	1.5	0	0.8	0.25	0.8
II	bulk	0	1.5	0	0.8	0.25	8
III	transitional layer	0	1.5	0.4	0.8	0.25	0.8
	surface layer	0	0	0.4	0.8	0.15	0.2

*FR: flow rate.

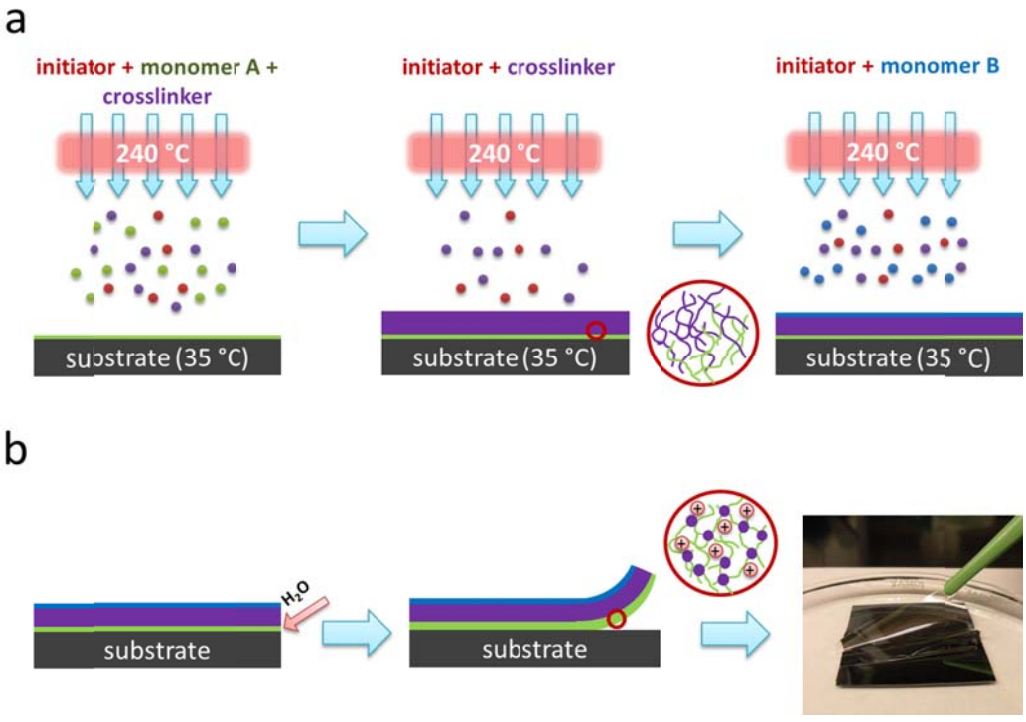

Figure A-1 a) Vapor deposition of functionally graded polymer films. In the circle is an illustration of the crosslinked structure connecting adjacent layers. b) Self-exfoliation of the deposited films.

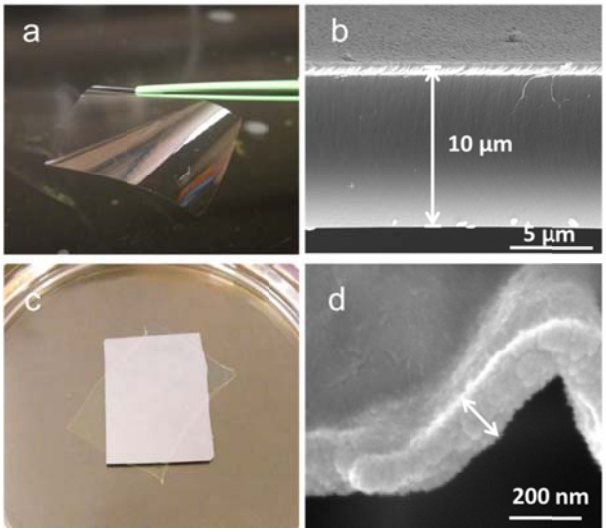

Figure A-2 The optical and SEM images of the fabricated free-standing films with thicknesses of 10 µm a) and b), and 150 nm c) and d).

Employing the high swelling behavior of the P(DMAEMA-*co*-EGDA) hydrogel prime layer, we demonstrate the self-exfoliation of the synthesized film in DI water. As shown in Figure A-1b, after immersing in deionized water for 3 min, the film was released from the Si wafer due to the high water-uptake of the hydrogel layer, and was easily collected by a pair of tweezers. The ionization of the tertiary amino groups induced the swelling of the hydrogel, which resulted in the invasion of water underneath the polymer film and subsequent separation of the film from substrate.

Figure A-2 shows the morphology of two exfoliated free-standing films with thicknesses of 10 µm and 150 nm. The 10 µm film is robust and can be easily manipulated by tweezers. The cross-sectional SEM image (Figure A-2b) reveals that the film is smooth and uniform. Since the hydrogel prime layer only contributes to a small portion of the entire film, the swelling of the hydrogel did not induce any "wavy" structure after exfoliation. The 150 nm film also retained its integrity after release from

the substrate, and showed a smooth surface without any cracks or fractures (Figure A-2c). The size and shape of the film resemble that of the silicon substrate. Small wrinkling structure, which is similar to the reported free-standing films assembled using LbL method,[42] was observed under the SEM, possibly due to the high swelling of the hydrogel. The compositional difference in the vertical growth direction did not cause any morphological variation across both films. We also demonstrate the fabrication of larger scale films (8 X 4 cm^2) by using a larger size substrate (A-S1). While free-standing films with different thicknesses have been successfully fabricated, we mainly focus on the characterization and discussion of the 10 μm film in this report. Although beyond the scope of this work, ultrathin free-standing films with functional grading are desirable in a variety of applications,[7,40] and the related research is ongoing in our lab.

A.3.2 Analysis of the graded free-standing films

The molecular structure of the graded free-standing film is schematically illustrated in Figure A-3. The film is consisted of a highly crosslinked PEGDA bulk layer and ultrathin layers of P(DMAEMA-*co*-EGDA) hydrogel and PPFDA at the two surfaces. Contact angle measurements were conducted on both sides of the film. As shown in Figure A-3, the top surface of the film exhibited hydrophobicity with a high contact angle of 118 ± 1°, which is similar to the reported contact angles of PPFDA films;[43] while the bottom surface of the film exhibited hydrophilicity with a low contact angle of 52 ± 1°. The contact angle measurements confirmed successful grading and amphiphilic nature of the thin film.

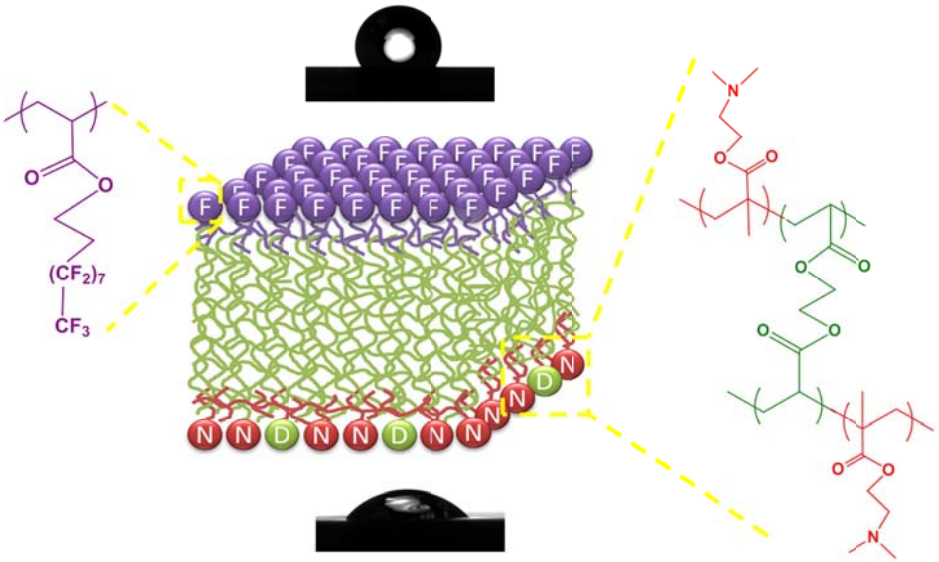

Figure A-3 Molecular structure of the graded free-standing film. The top and bottom images show the water contact angles of the hydrophobic and hydrophilic sides of the film, respectively.

Table A-2 Comparison of the contact angle (θ) and weight of the film before and after soaking in a pH=7 buffer for a 7-day period.

	day 0	day 7
θ_{top}	118 ± 1°	116 ± 1°
θ_{bottom}	52 ± 1°	47 ± 1°
weight (mg)	36.1	36.0

The graded film was then soaked in a neutral buffer solution (pH=7) for a 7-day period in order to study its stability. After soaking and drying, the contact angles of the two surfaces were measured again as shown in Table A-2. The soaking process did not cause any obvious change in the contact angle of the hydrophobic side, while the contact angle of the hydrophilic side decreased by 5°, possibly due to the residual water in the hydrogel. The weight loss of the film is also negligible. Compared with the free-standing films synthesized by LbL assembly, which are usually prone to degradation in physiological conditions,[32,33] the vapor-crosslinking deposition is able to create functionally graded structures with substantially enhanced stability without any necessity of post-treatment.

ATR-FTIR was employed to identify the surface composition of the graded film, as it is able to measure the IR absorption of surface layers as thin as 1 μm. As shown in Figure A-4, the hydrophobic side of the film has strong absorption peaks at 1146, 1201, and 1234 cm^{-1}, which are characteristic absorption peaks of $–CF_2–$ and $–CF_3$ moieties in PFDA.[44] The absorption peak at 1732 cm^{-1} is designated to the C=O stretching, which stems from the carbonyl groups of PFDA and EGDA. Compared with the spectrum of the PPFDA homopolymer film (supporting information), the intensity ratio of C=O to C-F (1146 cm^{-1}) stretching peaks from the graded film is larger, indicating the incorporation of EGDA moiety at the transitional layer. The hydrophilic side of the film, on the other hand, does not show any trace of the $–CF_2–$ or $–CF_3$ absorption. Absorption peaks at 2823 and 2774 cm^{-1} are designated to the $–CH_3$ stretching of tertiary amine groups, while the sharp peak at 1723 cm^{-1} stems from the C=O stretching of both DMAEMA and EGDA. The much stronger absorption of the C=O stretching than that of the $–CH_3$

stretching is due to the transitional layer of highly crosslinked P(DMAEMA-*co*-EGDA). Neither the hydrophilic nor hydrophobic side of the film shows any trace of the characteristic peaks from their counterparts, indicating the effective grading of the two functional moieties.

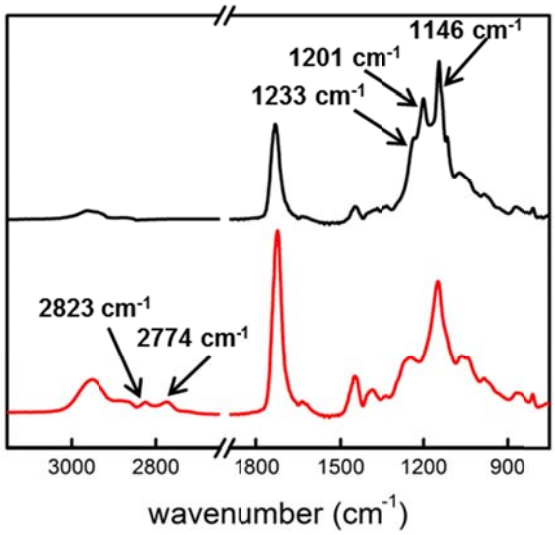

Figure A-4 ATR-FTIR spectra of the hydrophobic (a) and hydrophilic (b) sides of the free-standing film.

The surface topography of the graded free-standing film was investigated using AFM (Figure A-5). Both surfaces are smooth without any wavy morphology. The top surface of the film, which is composed of PPFDA, showed a relatively rough surface with a root-mean-square roughness (R_q) of 8.37 nm. Vapor deposited fluoropolymer has been reported to have rougher surfaces in comparison with hydrophilic polymers.[45] Granular structures were observed on the surface, indicating possible aggregation of the fluorine groups. The surface composed of P(DMAEMA-*co*-EGDA) hydrogel exhibited a significantly smoother surface with a R_q of 0.98 nm, which is comparable with that of the

reported poly(2-hydroxyethyl methacrylate)[45] and poly(dimethylaminomethylstyrene-*co*-ethylene glycol diacrylate)[39] films synthesized by vapor deposition.

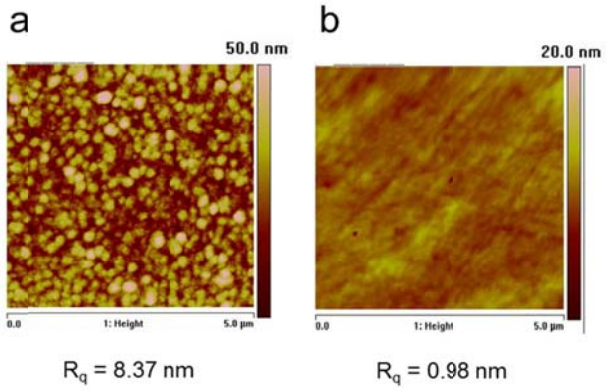

Figure A-5 AFM surface topography of the hydrophobic (a) and hydrophilic (b) sides of the free-standing film.

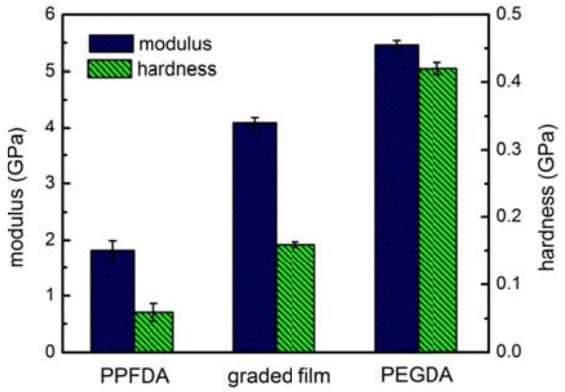

Figure A- 6 Modulus and hardness of the PPFDA, graded and PEGDA films.

A.3.3 Mechanical and optical properties

The mechanical property of the graded film was studied using nanoindentation. For comparison, mechanical property of the vapor deposited PPFDA and PEGDA films was

also investigated. As shown in Figure A-6, both modulus and hardness of the PPFDA film are relatively low, due to the weak intermolecular interaction between fluorinated chains and the consequent phase segregation.[46] The mechanical property of the PPFDA film is comparable to the reported values of other fluorinated polymers, such as poly(tetrafluoroethylene)[47] and poly((perfluoroalkyl)ethyl methacrylate)[48]. The PEGDA film, on the other hand, is mechanically strong with the modulus and hardness of 5.46 GPa and 0.42 GPa, respectively, which can be attributed to the cohesion of the EGDA chains and the highly crosslinked structure. Compared with the PPFDA film, the graded film exhibited enhanced mechanical property with the elastic modulus increased from 1.82 GPa to 4.09 GPa and hardness increased from 0.06 GPa to 0.16 GPa. It is therefore evident that the highly crosslinked PEGDA in the bulk of the film along with the transitional layer of P(PFDA-*co*-EGDA) has provided strong support to the PPFDA surface layer. Additionally, as we previously reported, vapor-crosslinking and the subsequent deposition of the functional monomer results in the hybrid grafting of the monomer on the crosslinked polymeric network.[39] Similarly, the graded deposition of PFDA lead to the secured immobilization of PPFDA on the film surface, which improved the integrity of the film and further promoted its robustness. We thus conclude that the graded structure renders the free-standing film enhanced mechanical robustness without sacrificing the surface functionality.

Further study on the optical properties of the graded free-standing film was performed by measuring the light transmittance of the film over a 350-800 nm wavelength range using UV-Vis spectroscopy. Excellent transparency of the film was observed from the UV-Vis spectrum, where more than 98% of transmittance was

achieved across the visible light spectrum (A-S2). Although fluorinated polymers tend to create optical hazes due to phase segregation,[46] functional grading improves the optical transmission of the film by confining the fluorinated components at the very top surface. The optical transparency of thin films is of significant importance for applications in optical devices and biomaterials. We prove our vapor deposition method fabricates functionally graded polymer films with higher optical transmittance than most of the reported multilayered free-standing polymer films.[8,27,32]

A.3.4 Single-step vapor patterning

Employing the method of vapor-crosslinking deposition, we further developed a single-step micropatterning strategy of free-standing films as illustrated in Figure A-7. A free-standing film with the top surface composed of PEGDA homopolymer was used as the substrate. An ultrathin prime layer (c.a. 40 nm) of highly crosslinked PEGDA was first deposited to ensure the affinity of the patterns to the film. The deposition then proceeded with a gradual transition to the desired surface composition, P(DMAEMA-*co*-EGDA) hydrogel in this case. The graded coatings were deposited both inside the holes and on top of the SiN template. Upon lifting off the template, coatings at the top were removed after deposition, while the coatings inside the holes remained on the film surface forming hydrogel micropatterns.

The topography and morphology of the patterned surface were examined using AFM and SEM. As shown in Figure A-8, highly ordered patterns of P(DMAEMA-*co*-EGDA) hydrogel with 2 μm in diameter were uniformly distributed on the surface. The micropatterns exhibited high fidelity to the template. From depth profile analysis (Figure

A-8b), each hydrogel domain exhibited cylindrical structure with an average height around 300 nm. The patterns were well-separated with high edge resolution without any debris between domains. To confirm the chemical functionality of the patterns, 1% fluorescein disodium solution was used to stain the hydrogel patterns on the free-standing film. Figure A-8d shows the selectively-stained patterning surface observed under fluorescence microscopy. The hydrogel domains clearly exhibit green fluorescence under the GFP filter, while the rest of the surface, which is composed of PEGDA, shows much darker color. The selective fluorescence functionalization is resulted from the electrostatic interactions between the positively charged tertiary amine in hydrogel and negatively charged fluorescein.[49,50]

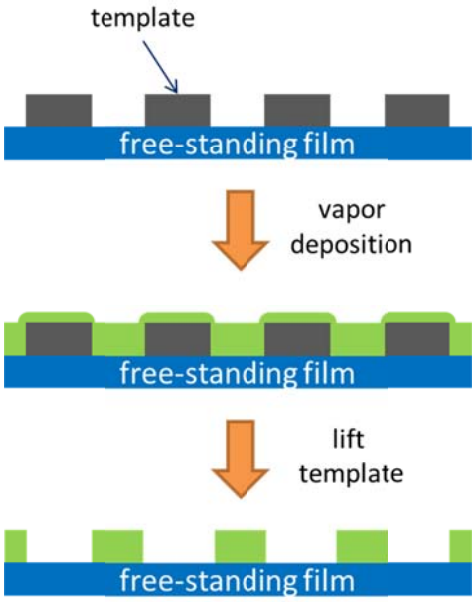

Figure A-7 Schematic illustration of the single-step vapor patterning of free-standing films.

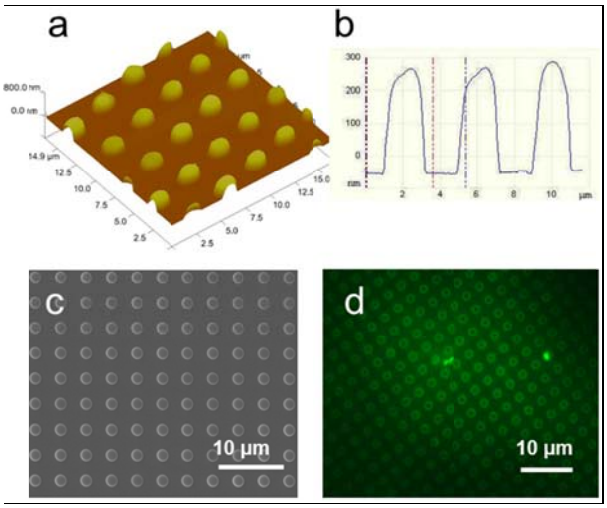

Figure A-8 a) Three dimensional AFM image and b) depth profile analysis of the patterned surface. c) SEM image of the micropatterns. d) Fluorescent functionalized micropatterns observed under fluorescent microscope.

The patterned free-standing film can be easily transferred onto surfaces with a variety of geometry for further applications attributed to its high flexibility. We demonstrate this concept by transferring the patterned film onto a glass rod. By simply releasing the patterned film in water and using the glass rod to load it, the film was tightly adhered to the end of the rod (Figure A-9). It is noted that the hydrogel layer returned to the deswollen state after drying, which restrained the film and created good adhesion to the glass surface. The film is not observable after transfer due to its high transparency, while the patterned area can be seen at the tip. The single-step micropatterning strategy combined with the ability to facilely synthesize functionally graded free-standing films is expected to provide a versatile and powerful tool in the research fields of cell biology, tissue engineering, and fabrication of biosensors and optical devices.

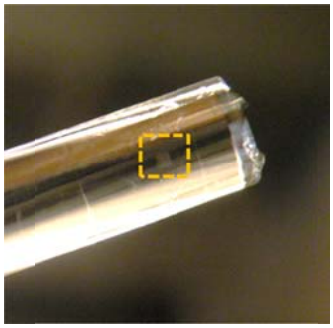

Figure A-9 The micropatterned free-standing film transferred onto a glass rod. Highlighted: the patterned area.

A.5 Conclusions

Functionally graded free-standing thin films were fabricated using vapor deposition. The vapor-deposited film incorporates both hydrophobic and hydrophilic components in a pre-determined order, resulting in an amphiphilic film with high crosslinking in the bulk and maximized functionality at the surface. The functional grading along with the crosslinked structure enabled high stability, high transparency, and mechanical robustness of the film, while the desired surface functionality was perfectly retained at the mean time. Furthermore, we demonstrate a facile route of micropatterning using vapor-crosslinking deposition. Highly-ordered cylindrical hydrogel domains with 2 μm diameter and 300 nm height were patterned onto the surface of the free-standing film in a single step. The micropatterns have distinct surface functionality from the background surface and high morphological fidelity to the template. The patterned thin film can be easily transferred onto surfaces with a variety of geometry, indicating its potential applications in miniaturized devices. It should be noted that although we used fluorinated polymer and hydrogel as the two surface components as a demonstration, the vapor

deposition method can be extended to fabricate graded structures with a variety of surface functionalities, such as epoxy chemistry, antimicrobial property, and surface responsiveness.

A.6 Acknowledgement

Financial support for this research was provided by the Oklahoma Center for the Advancement of Science and Technology (Award # ONAP 09-12 and AR 09.02-024). We thank the Oklahoma State University Microscopy Laboratory for SEM and AFM experiments. We also thank Dr. Ranga Komanduri, Fang Wang, and Boshen Fu for the nanoindentation tests.

A.7 References:

1. M. E. Buck and D. M. Lynn, *Advanced Materials*, 2010, **22**, 994-+.
2. I. Galeska, T. Hickey, F. Moussy, D. Kreutzer and F. Papadimitrakopoulos, *Biomacromolecules*, 2001, **2**, 1249-1255.
3. S. R. Forrest, *Nature*, 2004, **428**, 911-918.
4. M. C. LeMieux and Z. N. Bao, *Nat. Nanotechnol.*, 2008, **3**, 585-586.
5. C. Y. Jiang, S. Markutsya, Y. Pikus and V. V. Tsukruk, *Nature Materials*, 2004, **3**, 721-728.
6. C. A. Constantine, S. V. Mello, A. Dupont, X. H. Cao, D. Santos, O. N. Oliveira, F. T. Strixino, E. C. Pereira, T. C. Cheng, J. J. Defrank and R. M. Leblanc, *J. Am. Chem. Soc.*, 2003, **125**, 1805-1809.
7. R. Vendamme, S. Y. Onoue, A. Nakao and T. Kunitake, *Nature Materials*, 2006, **5**, 494-501.
8. P. Podsiadlo, A. K. Kaushik, E. M. Arruda, A. M. Waas, B. S. Shim, J. D. Xu, H. Nandivada, B. G. Pumplin, J. Lahann, A. Ramamoorthy and N. A. Kotov, *Science*, 2007, **318**, 80-83.
9. W. L. Cheng, M. J. Campolongo, S. J. Tan and D. Luo, *Nano Today*, 2009, **4**, 482-493.
10. L. Zhai, M. C. Berg, F. C. Cebeci, Y. Kim, J. M. Milwid, M. F. Rubner and R. E. Cohen, *Nano Lett.*, 2006, **6**, 1213-1217.
11. Z. Y. Tang, Y. Wang, P. Podsiadlo and N. A. Kotov, *Advanced Materials*, 2006, **18**, 3203-3224.
12. T. Boudou, T. Crouzier, K. F. Ren, G. Blin and C. Picart, *Advanced Materials*, 2010, **22**, 441-467.
13. H. Kerdjoudj, N. Berthelemy, F. Boulmedais, J. F. Stoltz, P. Menu and J. C. Voegel, *Soft Matter*, 2010, **6**, 3722-3734.
14. T. Boudou, T. Crouzier, K. Ren, G. Blin and C. Picart, *Advanced Materials*, 2010, **22**, 441-467.
15. P. T. Hammond, *Advanced Materials*, 2004, **16**, 1271-1293.
16. G. Decher, *Science*, 1997, **277**, 1232-1237.
17. D. H. McCullough and S. L. Regen, *Chemical Communications*, 2004, 2787-2791.
18. A. K. Boal, F. Ilhan, J. E. DeRouchey, T. Thurn-Albrecht, T. P. Russell and V. M. Rotello, *Nature*, 2000, **404**, 746-748.
19. O. Uzun, B. L. Frankamp, A. Sanyal and V. M. Rotello, *Chemistry of Materials*, 2006, **18**, 5404-5409.
20. S. Srivastava and N. A. Kotov, *Accounts of Chemical Research*, 2008, **41**, 1831-1841.
21. A. A. Mamedov, N. A. Kotov, M. Prato, D. M. Guldi, J. P. Wicksted and A. Hirsch, *Nature Materials*, 2002, **1**, 190-194.
22. C. Y. Jiang, H. Y. Ko and V. V. Tsukruk, *Advanced Materials*, 2005, **17**, 2127-+.
23. P. Podsiadlo, Z. Y. Tang, B. S. Shim and N. A. Kotov, *Nano Lett.*, 2007, **7**, 1224-1231.
24. F. Boulmedais, V. Ball, P. Schwinte, B. Frisch, P. Schaaf and J. C. Voegel, *Langmuir*, 2003, **19**, 440-445.

25. P. J. Yoo, K. T. Nam, J. F. Qi, S. K. Lee, J. Park, A. M. Belcher and P. T. Hammond, *Nature Materials*, 2006, **5**, 234-240.
26. R. S. Krishnan, M. E. Mackay, P. M. Duxbury, A. Pastor, C. J. Hawker, B. Van Horn, S. Asokan and M. S. Wong, *Nano Lett.*, 2007, **7**, 484-489.
27. S. Lee, B. Lee, B. J. Kim, J. Park, M. Yoo, W. K. Bae, K. Char, C. J. Hawker, J. Bang and J. H. Cho, *J. Am. Chem. Soc.*, 2009, **131**, 2579-2587.
28. M. E. Buck and D. M. Lynn, *Langmuir*, 2010, **26**, 16134-16140.
29. L. Richert, F. Boulmedais, P. Lavalle, J. Mutterer, E. Ferreux, G. Decher, P. Schaaf, J. C. Voegel and C. Picart, *Biomacromolecules*, 2004, **5**, 284-294.
30. J. H. Dai, A. W. Jensen, D. K. Mohanty, J. Erndt and M. L. Bruening, *Langmuir*, 2001, **17**, 931-937.
31. J. L. Lutkenhaus, K. D. Hrabak, K. McEnnis and P. T. Hammond, *J. Am. Chem. Soc.*, 2005, **127**, 17228-17234.
32. A. L. Larkin, R. M. Davis and P. Rajagopalan, *Biomacromolecules*, 2010, **11**, 2788-2796.
33. S. Kim, B. Lee, J. Bang and J. Cho, *Macromolecular Chemistry and Physics*, 2010, **211**, 1188-1195.
34. J. Park, J. Kim, S. Lee, J. Bang, B. J. Kim, Y. S. Kim and J. Cho, *Journal of Materials Chemistry*, 2009, **19**, 4488-4490.
35. Y. Mao and K. K. Gleason, *Langmuir*, 2004, **20**, 2484-2488.
36. M. E. Alf, A. Asatekin, M. C. Barr, S. H. Baxamusa, H. Chelawat, G. Ozaydin-Ince, C. D. Petruczok, R. Sreenivasan, W. E. Tenhaeff, N. J. Trujillo, S. Vaddiraju, J. Xu and K. K. Gleason, *Advanced Materials*, 2010, **22**, 1993-2027.
37. K. K. S. Lau and K. K. Gleason, *Advanced Materials*, 2006, **18**, 1972-+.
38. Y. M. Ye, Q. Song and Y. Mao, *Journal of Materials Chemistry*, 2011, **21**, 257-262.
39. Y. M. Ye, Q. Song and Y. Mao, *Journal of Materials Chemistry*, 2011.
40. R. Sreenivasan, E. K. Bassett, D. M. Hoganson, J. P. Vacanti and K. K. Gleason, *Biomaterials*, 2011, **32**, 3883-3889.
41. Y. M. Ye and Y. Mao, *Journal of Materials Chemistry*, 2011, **21**, 7946-7952.
42. Y. Ma, J. Sun and J. Shen, *Chemistry of Materials*, 2007, **19**, 5058-5062.
43. W. E. Tenhaeff and K. K. Gleason, *Advanced Functional Materials*, 2008, **18**, 979-992.
44. M. Gupta and K. K. Gleason, *Langmuir*, 2006, **22**, 10047-10052.
45. S. H. Baxamusa and K. K. Gleason, *Advanced Functional Materials*, 2009, **19**, 3489-3496.
46. D. Anton, *Advanced Materials*, 1998, **10**, 1197-+.
47. J. Wang, F. G. Shi, T. G. Nieh, B. Zhao, M. R. Brongo, S. Qu and T. Rosenmayer, *Scripta Materialia*, 2000, **42**, 687-694.
48. Y. Mao and K. K. Gleason, *Macromolecules*, 2006, **39**, 3895-3900.
49. R. Kugler, O. Bouloussa and F. Rondelez, *Microbiology-Sgm*, 2005, **151**, 1341-1348.
50. N. Sahiner and M. Singh, *Polymer*, 2007, **48**, 2827-2834.

A.8 Supporting information

A-S1 A larger-scale free-standing film with the size of 8 X 4 cm^2.

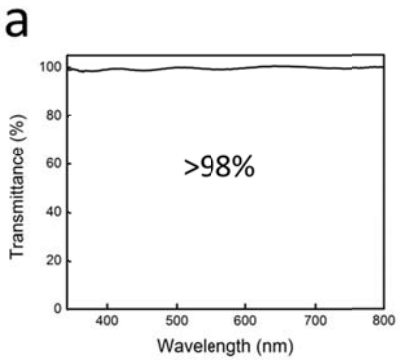

A-S2 a) UV-Vis spectrum of the free-standing film over the wavelength range of 350-800 nm, b) high transparency of the film.

APPPENDIX B

SYNTHESIS OF POLYMER NANOTUBES VIA VAPOR-BASED APPROACH

Polymer nanostructures are of great importance in a wide range of applications. Taking advantage of the iCVD process, we were able to fabricate polymer nanotube structures using a templated method. Two different porous membranes were used as templates, alumina membrane and polycarbonate membrane. The morphology of the two membranes was shown in Figure B-1. The alumina membrane has a more ordered structure with the pore size of 200 nm and thickness of 60 μm, while the polycarbonate membrane is less ordered with the pore size of 1 μm and thickness of 10 μm.

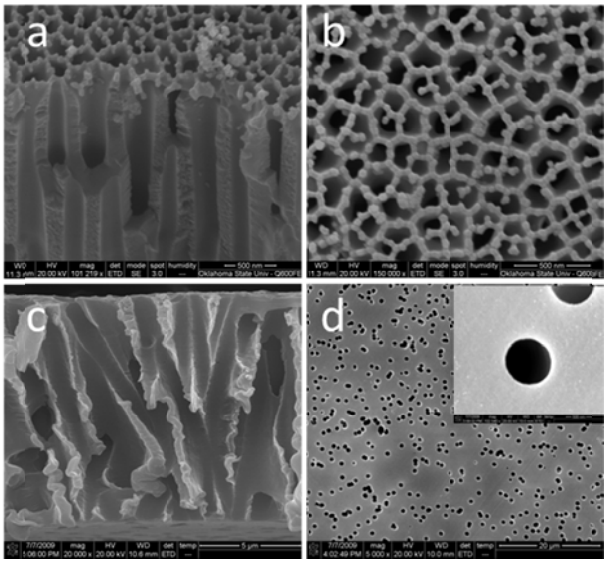

Figure B-1 Cross-sectional and top view of alumina a) and b), and polycarbonate c) and d) membranes.

The membranes were first put into the iCVD reactor and coated with a thin layer of polymer. Poly(glycidyl methacrylate) (PGMA) and poly(2-hydroxyl ethyl methacrylate-*co*-ethylene glycol diacrylate) (P(HEMA-*co*-EGDA)) were applied onto alumina membranes, while poly(methacrylic acid-*co*-ethylene glycol diacrylate) (P(MAA-*co*-EGDA) was applied onto polycarbonate membranes. After coating, the alumina membranes were dissolved in sodium hydroxide solution (pH=1) and the

polycarbonate membranes were dissolved in chloroform. The obtained structures were shown in Figure B-2. As shown in Figure B-2a and b, PGMA coatings formed disordered nanotube structures with the diameter of about 200 nm, which is the diameter of the pore size of alumina membranes. The P(HEMA-*co*-EGDA) nanotubes are still aligned after dissolving the alumina membrane, while the diameter is about 400 nm. The increase of the size of the nanotube is due to the swelling of the P(HEMA-*co*-EGDA) hydrogel in sodium hydroxide solution. The (P(MAA-*co*-EGDA) nanotubes exhibited vertically aligned structures, attributed to the low aspect ratio of the pores in polycarbonate membranes.

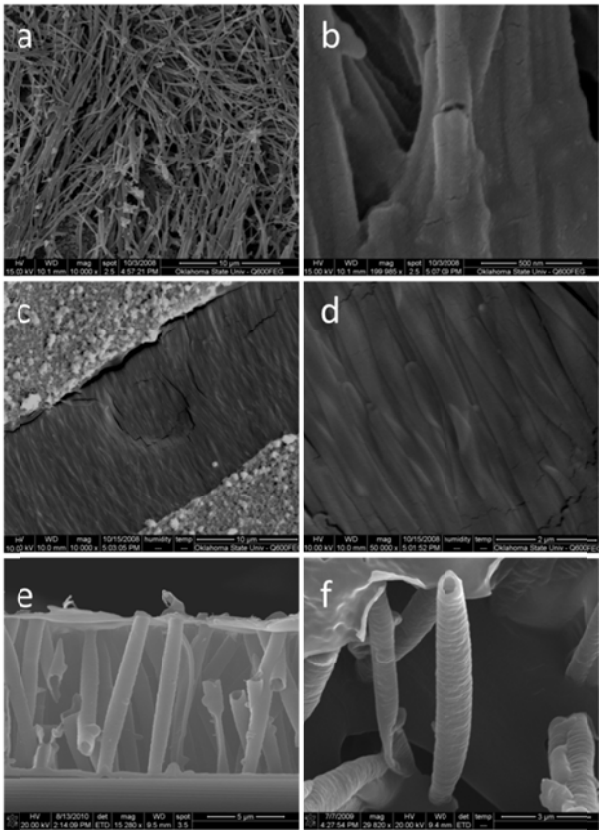

Figure B-2 a) and b) PGMA nanotubes formed in alumina membranes; c) and d) (P(HEMA-*co*-EGDA)) nanotubes formed in alumina membranes; e) and f) (P(MAA-*co*-EGDA) nanotubes formed in polycarbonate membranes.

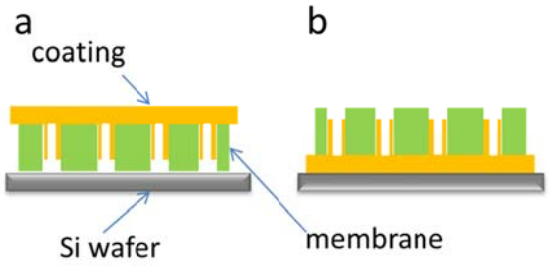

Figure B-3 Schematic illustrations of the two setups during annealing of PGMA nanotubes.

We further analyzed the effect of annealing of PGMA coatings in the membranes on the morphology of obtained PGMA nanotubes. Two different setups were employed to anneal the PGMA coatings inside the alumina membrane as shown in Figure B-3. For both of the setups, PGMA coatings were annealed at 180 ºC for 1 h. The resultant morphology of the nanotubes is distinct. When the coated side of the membrane was facing down during annealing, the PGMA coatings inside the nanopores accumulated on the surface of the membrane because of the gravity, forming short but thick nanotube arrays (Figure B-4a). On the contrary, when the coated side of the membrane was facing up during annealing, the nanotubes extended their length and formed long and thin nanotube arrays.

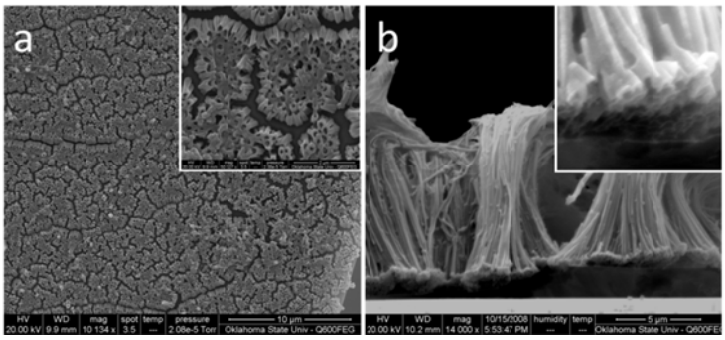

Figure B-4 PGMA nanotube arrays formed after annealing with a) the coated side of the membrane facing down and b) the coated side facing up.

APPPENDIX C

THE EFFECT OF ICVD PROCESS ON THE ENZYME ACTIVITY

Enzyme immobilization is an important step in biosensor fabrication. To use iCVD as a means to encapsulate enzymes in hydrogel coatings suggests a simple immobilization approach. Preliminary test on the impact of the iCVD process on the enzyme activity was thus performed. α-chymotrypsin (CT) was employed as the model enzyme and dipped on a silicon wafer. The dried CT was then put inside the reactor, coated with a 200 nm poly(methacrylic-*co*-ethylene glycol diacrylate) hydrogel and tested for activity. As seen in Figure C-1, compared with the enzymes in free solution and dipped on Si wafer, the enzyme underwent the iCVD process still remained active. Considering the diffusion factor of the coated enzyme from a confined space to the solution, the deposition process itself showed minimal influence on the enzyme activity.

Enzyme activity measurement. The activity measurement was performed by hydrolyzing a tetrapeptide (TP) N-Succinyl-Ala-Ala-Pro-Phe *p*-nitroanilide (Aldrich) using α-chymotrypsin (CT) (from bovine pancreas type II, Aldrich). For the free solution activity test, 1 ml 800 nM CT aqueous buffer (5 mM PBS, pH=7.4) and 1 ml stock solution of 0.1 mM TP (5mM PBS, pH=7.4, containing 1% dimethylformamide) were used. For the activity test of the enzymes underwent the iCVD coating process, 0.8 nmol CT was dipped onto a Si wafer, air-dried and coated with a 200 nm hydrogel film. 1 ml stock TP solution mixed with 1 ml PBS was then applied as the substrate solution. The product concentration was monitored by measuring the absorbance of the resultant solutions at 380 nm using a UV-Vis spectrometer (Cary 300).

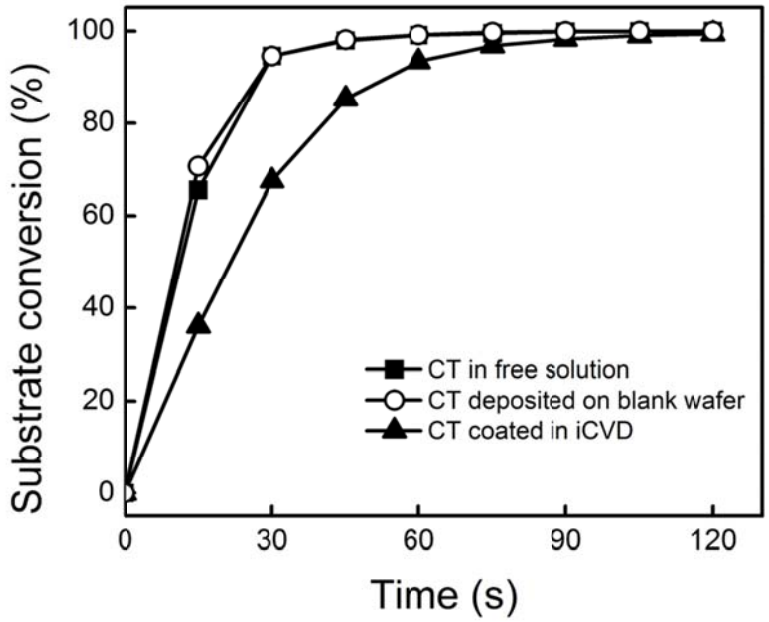

Figure C-1 Activities of chymotrypsin in free solution, deposited on Si wafer, and underwent the iCVD process.

APPPENDIX D

ACRYNOMS

AFM	atomic force microscope
ASWNT	aligned single-walled carbon nanotube
ATR	attenuated total reflection
ATRP	atom transfer radical polymerization
B. subtilis	*Bacillus subtilis*
BSA	bovine serum albumin
CA	contact angle
CFU	colony forming unit
CNT	carbon nanotube
CT	chymotrypsin
CVD	chemical vapor deposition
DMAEMA	dimethyl amino ethyl methacrylate
DMAMS	dimethyl amino methyl styrene
E. coli	*Escherichia coli*
EGDA	ethylene glycol diacrylate
EMA	effective medium approximation
FTIR	Fourier Transform Infrared
GMA	glycidyl methacrylate
HP	Hagen-Poiseuille
iCVD	initiated chemical vapor deposition
LbL	layer-by-layer
MAA	methacrylic acid
MFC	mass flow controller
MG	Maxwell-Garnett
MWNT	multi-walled carbon nanotube
P(DMAEMA-*co*-EGDA)	poly(dimethyl amino ethyl methacrylate-*co*-ethylene glycol diacrylate)

P(DMAMS-*co*-EGDA) poly(dimethyl amino methyl styrene-*co*-ethylene glycol diacrylate)

P(DMAMS-*co*-EGDA)-g-PDMAMS poly(dimethyl amino ethyl methacrylate-*co*-ethylene glycol diacrylate)-*g*-poly(dimethyl amino ethyl methacrylate)

P(MAA-*co*-EGDA) poly(methacrylic acid-*co*-ethylene glycol diacrylate)

P(PFDA-*co*-EGDA) poly(1H,1H,2H,2H-perfluorodecyl acrylate-*co*-ethylene glycol diacrylate)

PBS phosphate buffer saline

PDMAEMA poly(dimethyl amino ethyl methacrylate)

PDMAMS poly(dimethyl amino methyl styrene)

PECVD plasma enhanced chemical vapor deposition

PEGDA poly(ethylene glycol diacrylate)

PFDA 1H,1H,2H,2H-perfluorodecyl acrylate

PGMA poly(glycidyl methacrylate)

PMAA poly(methacrylic acid)

PNIPAm poly(*N*-isopropylacrylamide)

PPFDA poly(1H,1H,2H,2H-perfluorodecyl acrylate)

RAFT reversible addition-fragmentation chain transfer

RBM radial breathing mode

SEM scanning electron microscope

SR swelling ratio

SWNT single-walled carbon nanotube

TBP *tert*-butyl peroxide

TEM transmission electron microscope

THz-TDS terahertz time-domain spectroscopy

VACNT vertically aligned carbon nanotube

XPS X-ray photoelectron spectroscopy

VITA

Yumin Ye

Candidate for the Degree of

Doctor of Philosophy

Thesis: BIOFUNCTIONAL POLYMER COATINGS VIA INITIATED CHEMICAL VAPOR DEPOSITION

Major Field: Biosystems Engineering

Biographical:

Education:

Completed the requirements for the Doctor of Philosophy in Biosystems Engineering at Oklahoma State University, Stillwater, Oklahoma in May, 2012.

Completed the requirements for the Master of Science in Materials Science and Engineering at Zhejiang University, Hangzhou, China in 2006.

Completed the requirements for the Bachelor of Science in Materials Science and Engineering at Zhejiang University, Hangzhou, China in 2004.

Experience:

Research engineer — December 2007 - August 2010
Oklahoma State University, Stillwater, OK

Professional Memberships:

Materials Research Society — 2008-present
American Association of Textile Chemists and Colorists — 2009-2010

Name: Yumin Ye Date of Degree: May, 2012

Institution: Oklahoma State University Location: Stillwater, Oklahoma

Title of Study: BIOFUNCTIONAL POLYMER COATINGS VIA INITIATED CHEMICAL VAPOR DEPOSITION

Pages in Study: 169 Candidate for the Degree of Doctor of Philosophy

Major Field: Biosystems Engineering

Scope and Method of Study:
Surface modification is of essential importance in bioengineering. Polymer thin coatings offer various functionalities and biocompatibility to the interface of biomaterials and biosystems. While conventional solution-based polymer coating techniques are fully capable of providing uniform thin coatings on flat surfaces, they have limitations in coating nano- and micro-structured substrates. Vapor-based polymer coatings have also been investigated mainly by plasma-assisted processes, which encounter difficulties in retaining the delicate functional groups and controlling stoichiometric chemistry. We employed initiated chemical vapor deposition (iCVD) to conformally coat micro- and nano-structured materials with different biofunctional polymer films. The introduction of the initiator allows complete retention of the monomer functionality, while the vapor-based approach permits the excellent preservation of the original morphology of the substrates.

Findings and Conclusions:
Using iCVD technique, we achieved successful surface modification in three different applications of bioengineering. In CHAPTER II, we demonstrate the creation of durable antibacterial coatings on textile and catheter. Bacterial killing efficacy of more than 99% was achieved on both substrates. The bactericidal effect was durable against continuous washing for up to 10 hours. CHAPTER III, IV, and V presented another important application of iCVD functionalization of vertically aligned carbon nanotubes, which is difficult to achieve using conventional methods. We demonstrated both non-covalent and covalent functionalization of aligned carbon nanotubes with different chemistry. The epoxy chemistry enabled significantly enhanced mechanical properties and wetting stability to the multi-walled carbon nanotube arrays. The covalent functionalization tuned electronic properties of the single walled carbon nanotube arrays. Hydrogel chemistry offered pH-responsiveness and substantially improved wettability to the low-site-density carbon nanotube arrays. In CHAPTER VI, we presented thermo-responsive hydrogel coatings on nanoporous membranes to fabricate smart nanovalves. The tunable transportation of biomolecules through the nanovalves was successfully triggered by the adjustment of temperatures.

ADVISER'S APPROVAL: Yu Mao